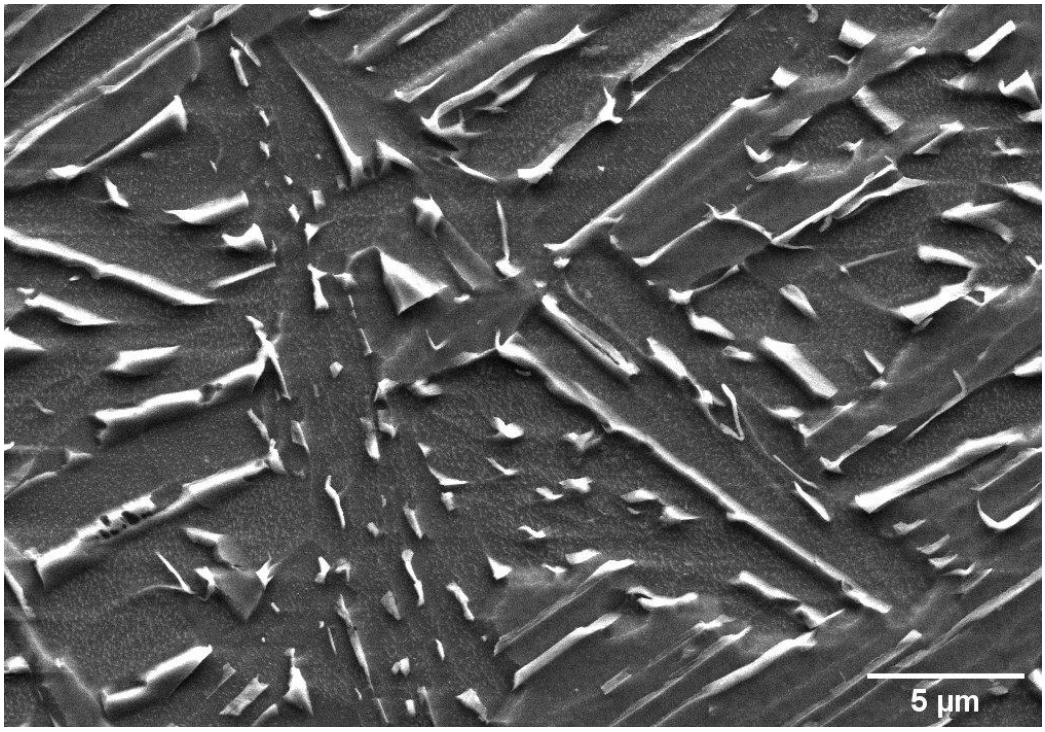

Characteristics of Porous Ti-6Al-4V Implant Fabricated by Electron Beam Melting (EBM) for Biomedical Applications

Master's Thesis in Materials Engineering

AKSHAY MUNDAYADAN CHANDROTH

DEPARTMENT OF INDUSTRIAL AND MATERIALS SCIENCE

CHALMERS UNIVERSITY OF TECHNOLOGY

Gothenburg, Sweden 2021

www.chalmers.se

MASTER'S THESIS 2021

Characteristics of Porous Ti-6Al-4V Implant Fabricated by Electron Beam Melting (EBM) for Biomedical Applications

Master's Thesis in Materials Engineering

AKSHAY MUNDAYADAN CHANDROTH

Department of Industrial and Materials Science

Chalmers University of Technology

Gothenburg, Sweden 2021

Master's Thesis

Characteristics of Porous Ti-6Al-4V Implant Fabricated by Electron Beam Melting (EBM) for Biomedical-Applications

Master's Thesis in Materials Engineering

AKSHAY MUNDAYADAN CHANDROTH

© AKSHAY MUNDAYADAN CHANDROTH

Examiner and Supervisor: Prof. Emmy Yu Cao, Department of Industrial and Materials Science

Supervisor: Dr. Anders Palmquist, Gothenburg University

Master's Thesis 2021

Department of Industrial and Materials Science

Chalmers University of Technology

SE – 412 96 Gothenburg

Telephone +46 31 772 1000

Cover: SEM micrograph of 5x13 – BS implant sample.

Gothenburg, Sweden 2021

Abstract

Additive manufacturing is turning out to be one of the prominent domain of research in recent times due to its ability to fabricate complex structures. The technique is extensively utilised in numerous applications, ranging from fabrication of clinical products to aerospace components. The drawbacks put forth by conventional manufacturing techniques in fabricating complex near net shape structures can be mitigated by additive manufacturing techniques. The ability to fabricate components with a trivial lead time and material wastage is another highlight of the technique. Additive Manufacturing techniques have phenomenal benefits, where complicated porous structures can be fabricated rapidly. An animal musculoskeletal system demands specific features for the implant materials for rejuvenation of lost body functions. The porous network have significant contributions towards biomechanical rejuvenation of the musculoskeletal system. The bone tissue – implant material interaction possess significant dependency on the surface properties of Ti-6Al-4V biomedical implant.

In the present research, the effect of powder recycling on the surface properties of the implant material fabricated by Electron Beam Melting (EBM) were investigated. The investigation was aimed to formulate an idea about the advantageous and disadvantageous effects of powder reuse in EBM. Microstructure of the implant, surface chemistry and geometry were characterized. The notable characterization techniques used were Scanning Electron Microscope, X-Ray Photoelectron Spectroscopy, X-Ray microtomography and Confocal Microscopy.

It was evident from the analysis that the overall microstructure of the implant samples exhibited trivial variation with respect to powder recycling. The lattice and solid regions in the implant samples were found to have a notable increase in oxygen content. The implant geometry and surface roughness were found to exhibit a feedstock induced variation.

Keywords: Additive Manufacturing**,** EBM, Ti-6Al-4V, Bone implants, Powder recycling

Acknowledgements

I would like to express my sincere gratitude to my mentor Prof. Emmy Yu Cao who have been with me throughout my journey at Chalmers. I am thankful to her for all the guidance, experimental support and wonderful oppurtunities.

I am thankful to Dr. Anders Palmquist (Gothenburg University) for his immense support and experimental guidance throughout the thesis. His wonderful inputs were valuable to find the right path.

A special gratitude should be expressed towards Jonas Holmberg from RI.SE for providing experimental setup and support for roughness measurement.

Also, I would like to thank Dr. Joakim Algardh (GE Additive) and Dr. Zhuoer Chen for the discussions on the topic and the truthful comments that made me think before I take a wrong step.

I would also like to thank Dr. Yimming Yao, Sri Bala Aditya Malladi, Erika Steyn, Dr. Antonio Mulone, Daniel Gren and other researchers in the department for their immense support and valuable inputs.

I would like to take this oppurtunity to thank my colleague Ahmed Fardan for his tips and tricks that helped me during the experiments.

The journey was smoother due to my friends, namely, Doyel Joseph, Sourav Nandakumar, Vishnu Anilkumar, Shibin Nair, Nagarajan Kumaresan, Christian Lundberg and Sreehari B. Ravindranath. I am thankful for being with me whenever I needed them.

The journey to Chalmers was possible only because of my teachers and friends at Amrita Vishwa Vidyapeetham. I would like to thank each and everyone of them, for their inputs. Finally I would like to thank my parents and the almighty for everything that they have done for me.

Table of contents

Abstract..... *i*

Acknowledgements.....*ii*

Table of contents.....*iii*

List of Figures.....*vi*

List of Tables.....*x*

1.Introduction.....*1*

1.1 Research Objective.....*2*

2. Theory.....*3*

2.1 Titanium alloys.....*3*

2.1.1 Alpha, Beta and Alpha + Beta Ti alloys.....*4*

2.1.2 Ti-6Al-4V.....*5*

2.2 Additive Manufacturing.....*6*

2.2.1 Laser Based- Powder Bed Fusion.....*7*

2.2.2 Electron Beam Melting (EBM).....*8*

2.2.3 Microstructure of EBM printed Ti-6Al-4V.....*10*

2.2.4 Defects in EBM printed samples.....*11*

2.2.5 Ti-6Al-4V powder processing for AM.....*12*

2.3 Titanium based implants and other materials.....*12*

2.3.1 Titanium based implants.....*12*

2.3.2 EBM of bone implants.....*13*

2.4 Characterisation techniques and their common principles.....*14*

2.4.1 Optical Microscope.....*14*

2.4.2 Scanning Electron Microscope.....*14*

2.4.3 Energy Dispersive X-Ray Spectroscopy.....*16*

2.4.4 X-Ray Photoelectron Spectroscopy.....*17*

2.4.5 X-Ray microtomography.....*18*

2.4.6 Confocal microscopy.....*19*

3. Methodology.....21
3.1 Sample details and nomenclature.....21
3.2 Sample preparation for analysis.....21
3.2.1 Sample preparation for poroity and microstructure analysis of implants.....22
3.2.2 Sample preparation for XPS analysis of implants.....23
3.2.3 Sample preparation for geometrical analysis of implants.....23
3.2.4 Sample preparation for surface roughness analysis.....24
3.2.5 Sample preparation for powder microstructure analysis.....24
3.2.6 Sample preparation for powder morphology analysis.....24
3.3 Sample characterisation.....24
3.3.1 Microstructural characterisation and composition analysis (EDS) of implant samples.....24
3.3.2 Porosity measurement of implant samples.....25
3.3.3 X-Ray Photoelectron Spectroscopy of implant samples.....25
3.3.4 Geometrical analysis of implant samples.....26
3.3.5 Roughness measurement of implant samples.....26
3.3.6 Microstructure analysis of powder samples.....26
3.3.7 Morphological analysis of powder samples.....26
3.3.8 Powder composition analysis.....27
4. Results and Discussion.....29
4.1 Powder samples.....29
4.2 Fabricated bone implants.....35
4.2.1 Microstructure at low magnification.....35
4.2.1.1 Microstructre and elemental composition of solid region in V13 implant.....35
4.2.1.2 Microstructre and elemental composition of solid region in 1x13 implant.....40

4.2.1.3 Microstructre and elemental composition of solid region in 5x13 implant.....45

4.2.1.4 Microstructre and elemental composition of lattice regions in implant samples.....48

4.2.1.5 Nano Precipitates.....51

4.2.1.6 Average α- lath thickness.....52

4.2.2 Porosity analysis.....53

4.2.2.1 Porosity percentage.....54

4.2.3 Implant surface chemistry.....56

4.2.3.1 Survey spectrum.....56

4.2.3.2 Chemical state.....58

4.2.3.3 Depth Profile.....60

4.2.3.4 Thickness of Oxide layer on the implant samples.....63

4.2.4 Implant lattice – geometrical analysis.....64

4.2.4.1 Average lattice strut thickness.....64

4.2.4.2 Lattice strut thickness distribution.....66

4.2.5 Implant lattice – topography and roughness.....68

5. Conclusions and Remarks.....73

6. Future scope.....75

7. References.....77

8. Appendix.....83

List of Figures

Figure 2.1: Microstructural features in Ti-6Al-4V.....4
Figure 2.2: Fundamental steps involved in additive manufacutring.....6
Figure 2.3: Working principle of Laser Based- Powder Bed Fusion.....8
Figure 2.4: Working principle of Electron Beam Melting.....9
Figure 2.5: Q10 plus EBM machine, courtsey GE Additive.....10
Figure 2.6: OM micograph portraying typical defects in Additive Manufacturing.....11
Figure 2.7: Gas Atomised Ti-6Al-4V powder particles.....12
Figure 2.8 : Schematic image portraying the osseointegrated and non-integrated bone implant in an animal body.....13
Figure 2.9 : Working principle of an Optical Microscope.....14
Figure 2.10: Working principle of a Scanning Electron Microscope.....15
Figure 2.11: Interaction volume generated by the electron beam and emission region of various signals.....16
Figure 2.12: Working principle of an X-Ray Photoelectron Spectrocopy.....17
Figure 2.13: Figure exhibiting the working of X-Ray microtomography.....19
Figure 2.14: Working principle of confocal microscopy.....20
Figure 3.1: Sectioned V13 implant with marked top and bottom regions.....22
Figure 4.1: Micrographs showing (a) virgin powder particle with satelites (b) virgin powder morphology (c) deformed 1x recycled powder (d) elongated 1x recycled powder particle (e) deformed 5x recycled powder and (f) broken 5x recycled powder particle.....30
Figure 4.2: Plots depicting the particle size distribution of (a) virgin powder (b) 1x recycled powder (c) 5x recycled powder.....31
Figure 4.3: SEM micrographs depicting (a) martensitic structure of virgin powder particle (b) internal porosity in virgin powder particle.....32
Figure 4.4: SEM micrographs depicting (a) microstructure of 1x recycled powder particle (b) fine martensitic needle and porosities in 1x recycled powder particle.....32
Figure 4.5: SEM micrographs depicting (a) microstructure of 5x recycled powder particle (b) internal porosity in 5x recycled powder particle.....33
Figure 4.6 : OM micrographs depicting the grain structure of (a) V-13 (b) 1x-13 and (c) 5x -13 implant.....35
Figure 4.7: An overview of the microstructure at the top region of V13 implant (V13-TS).....36
Figure 4.8: SEM micrographs of V13-TS implant depicting (a) martnesitic phase (b) large α phase.....36

Figure 4.9: SEM micrographs of V13-TS implant depicting (a) colony of α phase (b) α and β features (c) basket weave α and (d) α bulges.....37
Figure 4.10: SEM micrographs of V13-TS implant depicting (a) β phase (b) nano precipitates.....38
Figure 4.11: An overview of the microstructure at the bottom region of V13 implant (V13-BS).....38
Figure 4.12: Micrograph of V13-BS depicting (a)basket weave α (b) grain boundary α and α bulges.....39
Figure 4.13: An overview of the microstructure at the top region of 1x-13 implant (1x13-TS).....40
Figure 4.14: Micrograph of 1x-TS depicting (a)martensitic needles (b) α bulges.....41
Figure 4.15: SEM micrographs of 1x-TS implant depicting (a) basket weave and colony α phase (b) α colony.....41
Figure 4.16: SEM micrographs of 1x-TS implant portraying a β phase.....42
Figure 4.17: An overview of the microstructure at the bottom region of 1x-13 implant (1x13-BS).....42
Figure 4.18: SEM micrographs of 1x-BS implant depicting (a) colony α phase (b) grain boundary α.....43
Figure 4.19: SEM micrographs of 1x-BS implant portraying a large α phase.....43
Figure 4.20: An overview of the microstructure at the top region of 5x-13 implant (5x13-TS).....45
Figure 4.21: Micrograph of 5x-TS depicting (a)martensitic needles (b) α bulges.....45
Figure 4.22: An overview of the microstructure at the top region of 5x-13 implant (5x13-BS).....46
Figure 4.23: Micrograph of 5x-BS depicting (a)basketweave α (b) α colony.....46
Figure 4.24: Micrograph of 5x-BS depicting (a)large α phase (b) grain boundary α.....47

Figure 4.25: Micrograph of (a) V13 lattice cross section (b) V13 solid cross section (c) 1x13 lattice cross section (d) 1x13 solid cross section (e) 5x13 lattice cross section and (f) 5x13 solid cross section.....49
Figure 4.26: Micrograph of horizontal plane of lattice (a)V13 implant (b) 1x 13 implant (c) 5x implant.....50
Figure 4.27: Micrograph of V13 BS solid sample portraying the nano sized precipitates in α matrix.....51
Figure 4.28: Micrographs portraying (a) V13 SE image (b) V13 BSE image(c)1x SE image (d) 1x BSE image (e) 5x SE image and (f) 5x BSE image.....52
Figure 4.29: Plot depicting the variation in α- lath thickness in implant samples with respect to powder recycling.....53
Figure 4.30: FEG-SEM Micrograph portraying (a) gas porosity in V13 solid sample (b) lack of fusion in 1x lattice sample (c) gas porosity in 5x solid sample (d) lack of fusion in 5x lattice sample.....54
Figure 4.31: Plot depicting the variation in porosity percentage with respect to build height in (a) V13 implant (b) 1x implant (c) 5x implant.....55
Figure 4.32: Plot depicting the variation in porosity percentage with respect to powder recycling.....56
Figure 4.33: Survey spectrum of (a) V13 lattice (b) V13 solid (c) 1x13 lattice (d) 1x13 solid (e) 5x13 lattice (f) 5x13 solid.....57
Figure 4.34: High resolution spectrum of (a) Lattice Ti 2p3/2 (b) Lattice Al 2p (c) Lattice V 2p3/2 (d) Lattice N1s.....58
Figure 4.35: High resolution spectrum of (a) Solid Ti 2p3/2 (b) Solid Al 2p (c) Solid V 2p3/2 (d) Solid N1s.....59
Figure 4.36: Depth profiles of (a) V13 lattice (b) V13 solid (c) 1x13 lattice (d) 1x13 solid (e) 5x13 lattice and (f) 5x13 solid.....61
Figure 4.37: Cation depth profiles of (a) V13 lattice (b) V13 solid (c) 1x13 lattice (d) 1x13 solid (e) 5x13 lattice and (f) 513 solid.....62

Figure 4.38: Scatter plot depicting the variation in oxide thickness of implants, with powder recycling.....63
Figure 4.39: SEM micrograph of V13 implant showing a lattice strut.....64
Figure 4.40: Plot depicting the average strut thickness at different regions in (a) V13 implant (b) 1x13 implant (c) 5x13 implant.....65
Figure 4.41: Plot depicting the average strut thickness for implant samples at different powder recycling numbers in the (a) top region of implant (b) middle region of implant (c) bottom region of implant.....66
Figure 4.42: Plot depicting the strut thickness distribution at (a) V13 top region (b) V13 middle region (c) V13 bottom region (d) 1x13 top region (e) 1x13 middle region (f) 1x13 bottom region (f) 5x13 top region (g) 5x13 middle region (h) 5x13 bottom region.....67
Figure 4.43: Thresholded image of the 5x13 bottom region sample (from CTAn software).....68
Figure 4.44: 3D maps portraying the peaks and valleys in lattice sample of (a) V13 bottom region (b) 1x13 bottom region (c) 5x13 bottom region (d) V13 middle region (e) 1x13 middle region (f) (e) 5x13 middle region.....69
Figure 4.45: Plots exhibiting (a) average peak height at bottom region of implant samples (b) average peak height at middle region of implant samples (c) average valley depth at bottom region of implant samples (d) average valley depth at middle region of implant samples.....70
Figure 4.46:Heat maps portraying the surface roughness in the lattice sample at (a) V13 bottom region (b) 1x13 bottom region (c) 5x13 bottom region (d) V13 middle region (e) 1x13 middle region (f) (e) 5x13 middle region.....71
Figure 4.47: Comparison plots portraying the variation in surface roughnes values of lattice samples with powder recycling, at the (a) bottom region of the implant samples and (b) top region of the implant sample.....72

List of Tables

Table 2.1: Table depicting alloying elements in titanium alloy system.....5
Table 3.1 : Sample Nomenclature system.....21
Table 3.2 : Parameters for polishing steps as recommended by Struers.....23
Table 4.1. Powder composition (Polished powder, ETH 10 kV, WD - 8.5mm).....33
Table 4.2. Powder composition (Mounted powder, ETH 10 kV, WD - 8.5mm).....34
Table 4.3. Powder composition (Mounted powder, ETH 15 kV, WD - 8.5mm).....34
Table 4.4 Powder composition (Mounted powder, ETH 20 kV, WD - 8.5mm).....34
Table 4.5. Compositional difference between phases present in the V13-TS microstructre.....39
Table 4.6. Compositional difference between phases present in the V13-BS microstructure.....39
Table 4.7. Compositional difference between phases present in the 1x-TS microstructure.....44
Table 4.8. Compositional difference between phases present in the 1x-BS microstructure.....44
Table 4.9. Compositional difference between phases present in the 5x-TS microstructure.....47
Table 4.10. Compositional difference between phases present in the 5x-BS microstructure.....47
Table 4.11 Compositional difference between phases present in the lattice V13 microstructure.....50
Table 4.12 Compositional difference between phases present in the lattice 1x13 microstructure.....50
Table 4.13 Compositional difference between phases present in the lattice 5x13 microstructure.....51

1. Introduction

Additive manufacturing is turning out to be a phenomenal technology in recent times. The ability of the technique to generate complex shaped structures is the major highlight, which makes it preferable for numerous applications. The technology is being utilised in several important areas ranging from aeronautical parts, automobile components and biomedical applications. Several factors like morphology, chemistry and geometry must be taken into account while manufacturing such kinds of products with relevant applications. A slight variation from the preferred standards can lead to incalculable failures. In order to avoid these kinds of incidents, researchers are continuously optimizing the technique to attain the best possible materials and parameters for manufacturing [1].

Biomedical applications require advanced manufacturing methods to create the complex geometry that fits into a human musculoskeletal system. Researchers have been proposing the improvisation in surface chemistry and geometry of the implants in order to advance [2]. The porous surface of implants like the acetabular cup is found to have a significant contribution towards biomechanical restoration of the musculoskeletal system through implant-bone tissue interaction [3]. The Additive Manufacturing (AM) process is found to have advantageous effects, which allows printing of critical structures with porous lattice structures. Unlike the conventional manufacturing technologies, AM is found to put forward an impressive ability to rapidly manufacture these scaffolds with integrated porous structures [1].

Electron Beam Melting (EBM), is an additive manufacturing technology that offers a relatively better scope for manufacturing these complex, thin lattice structures. The emphasis of research on EBM printed bone implants is increasing due to its capability in rapid manufacturing. This offers even better opportunities like shorter leading times, reduced material wastage, flexible build design freedom and shorter manufacturing steps. In EBM, the metallic powders are fused in a layer by layer pattern according to the stereolithographic (STL) model of the component using an electron beam, unlike in Laser Based Powder Bed Fusion (LB-PBF), an equally competitive technique. Due to the usage of high electron beams in EBM instead of laser energy, the process time can be shortened to a significant range [1], [4].

The biomechanical rejuvenation process is assisted by the implant materials in numerous ways. The osteoblasts should be interacting with the implant material in order to aid the muscle repairing process. Earlier, stainless steels were used to manufacture implants. Nevertheless, it was found that materials like Ti-6Al-4V and magnesium alloys offer a reduction in stress shielding effect compared to implants manufactured from stainless steels [3]. Ti-6Al-4V is one of the most promising materials manufactured using EBM technology. However, intensive research is still required to assist the enormous demands in the upcoming society.

The healing capacity of the developed porous and solid bone implants, manufactured through EBM using Ti-6Al-4V were subjected to investigations [5], [6]. The results were found satisfactory, nevertheless, the advantageous effects of geometrical and surface properties of implants on bone healing kinetics needs to be investigated to formulate a better future prospective.

1.1 Research objective

In this investigation, three different acetabular cups manufactured by GE Additive are subjected to various experiments. The major focus of this research is to identify the geometrical, chemical and microstructural effects of powder recycling on Ti-6Al-4V implants fabricated through EBM. Three different batches of feedstocks were used to manufacture the implants, namely, virgin, one times recycled and five times recycled powder. The characterisation methods used to analyse the implants are Scanning Electron Microscopy (SEM), Energy Dispersive X-Ray Spectroscopy (EDS), Optical Microscopy (OM), X-Ray Photoelectron Spectroscopy (XPS) and X-Ray microtomography.

Several questions should be answered in order to formulate a reliable conclusion to this thesis. The major question is the *effect of powder recycling and variation in build height on the part porosity and microstructure*. Secondly, the *chemical variation on the lattice structure and the solid part of the implant with respect to powder recycling* will be analyzed. The third query is the *variation in geometrical features of the lattice structures with respect to the powder feedstock used for implant fabrication*.

2. Theory

Titanium is one of the prominent and abundant materials on earth which have a comparatively higher cost of extraction and ore processing compared to numerous other materials like iron and aluminium [7], [8]. The method of processing the titanium ore is difficult and expensive due to the presence of various elements associated like nitrogen, hydrogen, carbon and oxygen [9]. Commercially pure titanium and numerous other alloys of titanium are being widely used these days for various applications in industries, biomedical sector, energy related areas, chemical sector, sports equipment etc. [8] .

The applications of titanium is wide due to its excellent strength to weight ratio, resistance to corrosion and comparatively lower strength to weight ratio, with respect to various commonly used elements [8]. Donachie and Matthew, have discussed their excellent performance in corrosive environments like marine and petrochemical habitat [7]. Nevertheless, the excellent performance in biological areas is also being evaluated. Until this time, titanium and its alloys are being appreciated by scientists for its appreciable ability to replace and repair broken bones of tested patients. Due to its anticorrosive properties and trivial level of toxicity, titanium alloys (especially Ti-6Al-4V), is excessively used to manufacture surgical equipment, orthodontic implants, joint and bone implants, prosthetics etc [8], [9]. In 2016, a study conducted by B. Basu points out that almost 2.2 million pounds (1000 tons) of titanium implants are implanted in patients every year [10], [11],[12]. This shows the importance of titanium in the biomedical sector.

2.1 Titanium Alloys (Ti Alloys)

A review of titanium alloys, its classifications, phase transformation and various other properties are discussed in this section of the report. The properties of Ti alloys vary a lot with their chemical composition, exposed environment and method of manufacturing. Most of the titanium alloys have a tensile strength which lies in between the range of 200 to 1400 MPa [10]. The most commonly used Ti alloy is Ti-6Al-4V having a significant range of properties which makes it suitable for several critical applications. Titanium is famous for exhibiting allotropic transformation at a particular temperature value of ~ 882 °C [8], [11]. Researchers have reported that the Body Centered Cubic structure popularly known as β phase [7] is transformed to Hexagonal Close Packed (HCP) structure (termed as α phase) below this temperature value. The HCP crystal structure is a densely packed atomic arrangement. In the Body Centered Cubic (BCC) crystal structure, a Ti atom is present at the center and corners of the cube [7]. The crystal structure of the alloys plays a significant role in the structural, physical and chemical properties of the material [8].

Numerous elements like vanadium, nitrogen, oxygen, aluminium etc can be added to titanium as phase stabilizers. These stabilizers are categorized into two different categories called β stabilizers and α stabilizers. α stabilizers are known to increase the β transus temperature by dissolving atoms in the α phase. The most commonly added α stabilizers in Ti alloys are aluminium and oxygen, which is reported to significantly alter the alloy properties like ductility [8], [13]. Elements like chromium and vanadium act as β stabilizers. These elements help in decreasing the β transus temperature, thus stabilizing the β phase. The ductility of the alloys are found to be increasing due to this elemental addition of β stabilizers[14]. Altogether, the addition of these stabilizing elements effectively tailor various properties and microstructure of the developed alloy.

The elemental composition of the alloy is shown to effectively tailor the alloy's microstructural features in a significant manner. At certain elemental compositions, the developed alloys exhibit stabilization of both β and α phase. Each element added to the alloy system is shown to alter different properties of the alloys. This means the variation in wt-% of the elements in the alloys system will tailors particular properties like mechanical and high temperature performance. To summarize, with respect to the elemental composition, there can be different phases that are stabilized in a titanium alloy; β phase, α phase and α + β phase [8], [13], [14].

2.1.1 Alpha, Beta and Alpha+Beta Ti alloys.

The *β Ti alloys* are most commonly used in biological applications due to the negligible content of toxic elements in their composition [14]. Some of the most popular beta titanium alloys are Ti-10-2-3, Ti17, Timetal 21S and Beta III [14]. These alloys which possess a BCC crystal structure portrays a significant weldability and heat treating capability [8], [14]. Nevertheless, the β - Ti alloys are comparatively costlier.

Commercially pure titanium or cp - Ti is an *α phase Ti alloy* which portrays critical performance at cryogenic temperatures. Even though it's called pure, the alloy generally contains elements like Oxygen and Iron (Fe). Properties like strength to weight ratio, intermediate product quality and notable resistance to creep makes it attractive [7], [13].

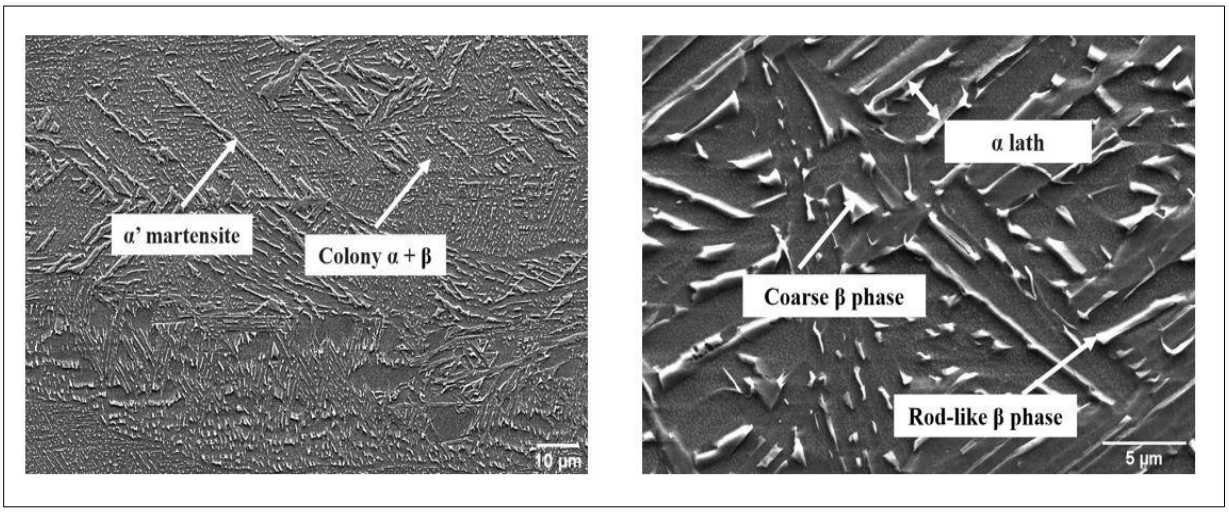

Figure 2.1: Microstructural features in Ti-6Al-4V.

α + β titanium alloys are known to exhibit both phases in its microstructure. These alloys are widely used for various applications due to its excellent properties like thermal conductivity, material castability and part weldability and high temperature performance (at 315 - 400 °C) [15]. Depending upon the composition of phase stabilizers, there can be various alloy systems like Ti-Al-2Sn and Ti-6Al-4V [16]. Elements like tin (Sn) and vanadium (V) act as a β stabilizer which stabilises the β phase by reducing the transus temperature. However, the α phase is stabilized by α stabilizers like aluminum (Al) [17]. The β transus temperature is critically affected by the compositional elements and their amount. This means that the transformation temperature can vary depending upon the type of alloys (α, β or α + β alloy)

[16], [18][19]. Figure 2.1 shows some of the phases present in the microstructure of Ti-6Al-4V. The general microstructure of α + β titanium alloys consists of features like duplex, equiaxed and lamellar structures [15]. The Table 2.1 details various stabilizing elements added to the titanium alloy system.

Table 2.1: Alloying elements in titanium alloy system.

Alloying elements	Effect of alloying
Zr, Sn	Strengthening alloying elements
Co, Si, Ni, Fe, Cr, Mn, Cu	β- eutectoid stabilizer
Ta, W, V, Mo	β- isomorphous stabilizer
Interstitial: N, O, C, Ga and Al	α- stabilizer

The transformation from one phase to another in Ti alloys is due to change of crystal structure of the alloy. This can alter the properties like hardness and melting point of the alloy due to the chemical reactions [15][17]. These kinds of transformations can be reversed, thus enabling the possibility to get back the α crystal from the formed β phase. However, certain conditions like thermal initiation and solidification rates of the melt needs to be controlled in order to achieve the required transformation. In general, the transformation from α → β or β → α can significantly affect the material properties of the developed Ti alloy [12], [15].

2.1.2. Ti-6Al-4V

Ti-6Al-4V is one of the most prominently used titanium alloy in this era. The alloy contains around 4 wt-% of vanadium (V), 6 wt-% aluminium (Al) and 90 wt-% of titanium (Ti). However, the composition can vary depending upon the manufacturers. Traces of elements like oxygen, hydrogen, nitrogen, iron and sometimes contaminants like silicon and yttrium can also be found in the fabricated alloy. Enormous amount of research has been carried out based on Ti-6Al-4V due to its notable properties [7], [8]. The scientific community is still undergoing research to enhance the properties like resistance to corrosive environment, biological adaptability and high strength to weight ratio [11].

Even after exhibiting superior material properties, the alloys still have disadvantages when it is considered for some critical applications. The unsustainable production method, comparatively higher cost of production, and the reactive nature of the material is reported to be a major drawback for the Ti-6Al-4V alloy system [8]. Also, when compared to high temperature nickel based superalloys the material is prone to reduction in strength and several other properties at elevated working temperatures [7], [11].

Ti-6Al-4V is a complex alloy system with both α and β phases. There can be various types of microstructural features in the developed alloy based on the processing methods and environment. For example, a homogeneous microstructure can be attained by significantly increasing the rate of solidification. The phase transformation kinetics during this melt solidification can be analyzed through techniques like High Temperature X- Ray Diffraction

[20]. The beta transus temperature for allotropic transformation in Ti-6Al-4V approximately lies at a temperature value of 995˚C. This is significantly higher when compared to the transformation temperature value (~882˚C) of commercially pure titanium or alpha Ti alloys [8], [19]. The increase in beta transus temperature can be attributed to the alloying elements added to the alloy system [17]. This is also found to affect the performance of the developed alloy.

The significant capability to tailor the mechanical and microstructural features of the alloys system through thermomechanical processes is the major highlight of the Ti-6Al-4V alloy system. The microstructural features of the Ti-6Al-4V system can be completely transformed into body centered cubic β phase structure. Nevertheless, gradual cooling of the system back to the β transus temperature can result in the formation of lath shaped structures or acicular features [19]. Figure 2.2 depicts the various features including acicular structures in the titanium microstructure.

This kind of thermomechanical processing is found to result in similar features as compared to the layer by layer build in electron beam melting fabrication. In the EBM manufacturing, each layer of metallic powder is reheated and cooled repeatedly above and below the β transus temperature during the building, making it complex. The typical microstructural features in EBM fabricated Ti-6Al-4V will be detailed in the trailing content.

2.2 Additive Manufacturing

Additive Manufacturing (AM) is one of the most promising technologies which is used to develop several complicated parts [1]. Figure 2.2 portrays the steps involved in additive manufacturing. It is a method which is utilised to join materials and make the final component based on the basic 3D model which is fed to the computer system. The process is usually a layer by layer manufacturing method which is completely contradicting with respect to the theory of subtractive manufacturing technologies [1]. There are various kinds of AM technologies which is utilized for rapid prototyping and rapid manufacturing of polymeric and metallic components. The most popular AM technologies which are being used these days are;

1. *VAT Photopolymerization*
2. *Powder Bed Fusion technology*
3. *Binder Jetting*
4. *Material Jetting*
5. *Material Extrusion*
6. *Sheet Lamination*
7. *Directed Energy Deposition* [21]

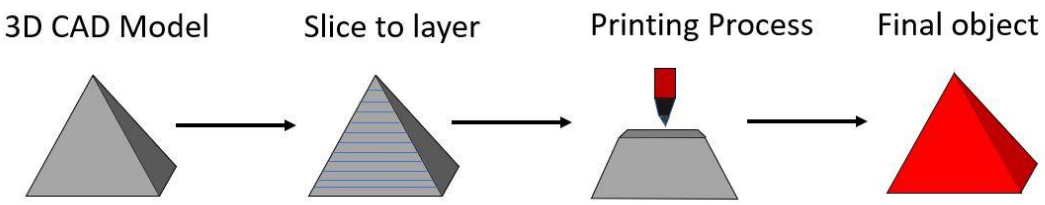

Figure 2.2: Fundamental steps involved in additive manufacturing

The general process steps in AM are identical for almost all the AM techniques. The common steps involved in the manufacturing procedure are:

1. *Development of CAD (Computer Aided Design)* file of the desired geometry to be manufactured.
2. *Conversion of the developed CAD file to STL* format, where the CAD geometry is sliced into various layers for manufacturing.
3. The developed *STL file* is processed in software's to distribute *support structures* and determine the build design.
4. *Setting up the machine*, which includes steps like cleaning the machine, recycling the remaining feedstock etc.
5. *Building of the desired geometry* with optimized build parameters.
6. *Removing the printed parts* from the build plate.
7. *Post processing* of build components using techniques like sand blasting to remove the loose powder and enhance the surface quality.
8. *Final heat treatments and other steps* should be carried out to achieve the desired state for application [22] [23]

In this investigation, the focus is more towards metal powder additive manufacturing which makes use of powdered feedstock to develop a final geometry.The most commonly used metal additive manufacturing methods are (i) Selective Laser Melting and (ii) Electron Beam Melting.

2.2.1 Laser Based - Powder Bed Fusion

This is a powder based metallic additive manufacturing technology, which makes use of a laser beam as its source of energy to melt the powder layers . Figure 2.3 portrays the working principle of Laser Based- Powder Bed Fusion. The process makes use of fine metallic powders to manufacture the parts in a layer by layer fashion . The powder size ranges from approximately 15 to 70 μm. The fabrication is carried out in an inert environment. The various parameters like beam energy, powder layer thickness etc. can be optimized in order to design the best processing methodology. The powdered feedstock is distributed homogeneously onto the building plate with the help of a recoater blade. The recoater ensures an even distribution of powdered feedstock at a desired thickness. The high intensity laser beam is selectively focused on the metallic powder layer based on the developed CAD model. After the fusion of each layer, the build plate is gradually lowered. This process of melting is repeated until the final component is manufactured. Post processing steps are also a crucial part of the methodology [24], [25].

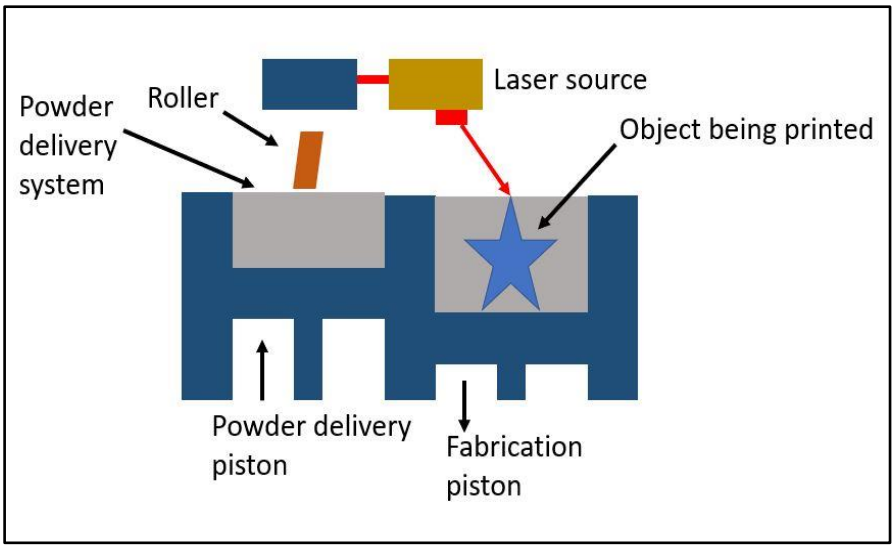

Figure 2.3: Working principle of Laser Based- Powder Bed Fusion.

2.2.2 Electron Beam Melting (EBM)

Electron Beam Melting is a competitive manufacturing technique developed during the late 20th century. The technology was initially developed as a master's thesis at Chalmers University of Technology and marketed by GE Additive (formerly known as Arcam AB) [26].The technique is now being extensively used to fabricate aerospace components and in the biomedical sector [24].

Unlike its competing technique, EBM makes use of a high energy electron beam instead of a laser beam. Figure 2.4 portrays the working ptinciple of EBM. The metallic powder is homogeneously distributed on the building plate with a layer thickness of approximately 50 to 200 µm. A typical EBM machine consists of several important parts like (i) Building Chamber and (ii) Electron beam chamber (Figure 2.5). Electron beam chamber is responsible for the high energy electron beam which fuses the material. The principal component of this chamber is a tungsten filament which is capable of producing electron beams with a high power ranging upto 3500 W [27]. The beam gun enables a beam spot size of approximately 200 to 1000 µm, and 1000 m/s scanning speed [27].

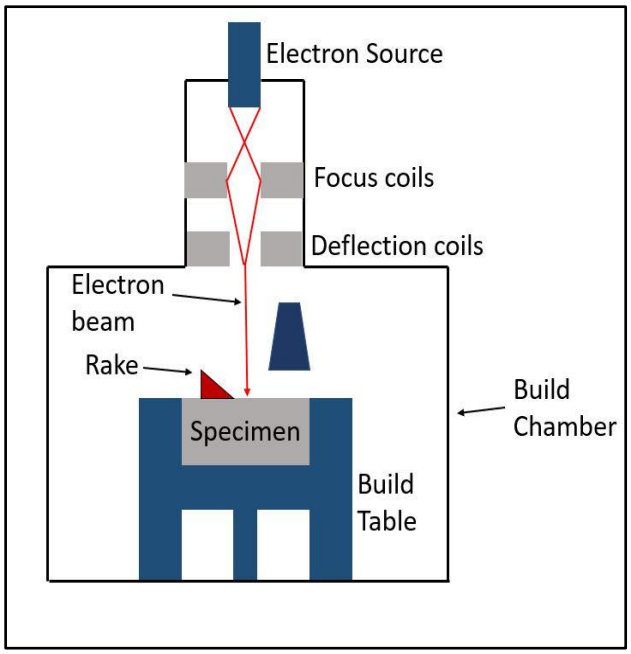

Figure 2.4: Working principle of Electron Beam Melting.

The powdered feedstock is fused by the heat energy produced by this electron beam. This happens inside the building chamber which is kept at a significantly high vacuum atmosphere (upto 10^{-5} mbar). The vacuum atmosphere is important in EBM, unlike LB-PBF due to its high energy electrons which can collide with the atmospheric gas, thus resulting in vigorous chemical reactions. Other than this, there are several other components like the build table and feedstock hopper in the building chamber [28]. The layer-by-layer manufacturing takes place on the build table made of steel. Rake is another important tool which assists in the uniform distribution of feedstock over the build plate. It is essential to maintain a uniform layer of metallic powder on the build plate to ensure a proper build [24], [27].

The fusion process is guided according to the provided CAD model. The powders are semi-sintered by the beam, prior to the melting process, in order to reduce internal cracks and induced stresses in the printed component. This is attained by semi sintering the powder using a low energy electron beam prior to fusion using a higher energy electron beam [27]. The chamber thermal history is complicated to understand and control [29]. This is the major reason behind the complex microstructure of the developed alloys systems. Due to the difficulty for heat transfer in the high vacuum chamber, there is always a significant difference in temperature at the melt pool region and the region far from the melt pool [24]. From the literature, the EBM process temperatures are calculated to be in the range of 620 to 700 °C. Nevertheless, the exact process temperature is still a hypothetical case [30].

There are two different steps involved in the melting procedure. Namely, hatch and contour melting. The outline of the component is printed during hatch melting, while the interior features are processed during the contour melting procedures. These steps are continued till the final component is achieved [31].

In this investigation, the samples are printed using a GE Additive Q10 Plus EBM printer (Figure 2.5) which is specifically utilized for fabrication of bone implants. The machine has a high energy electron beam source of 3 KW and a large build volume of 200 mm x 200 mm x

180 mm. The machine also provides additional features like enhanced resolution and varying material options [32].

Figure 2.5: Q10 plus EBM machine, courtesy GE Additive [32]

EBM printed samples might always require efficient post processing methods like loose powder removal, annealing and other heat treatment methods. Compared to other methods, the sample printed using EBM usually offers a poor surface finish and a lower density. This can adversely affect the mechanical performance of the samples when subjected to high cyclic loads. There can be various kinds of porosities in the EBM printed samples. Therefore, the post processing techniques like Hot Isostatic Pressing, surface smoothening, grinding and sandblasting are essential for the fabricated components [27], [31].

The unmelted loose feedstock can be recovered and recycled with the help of a Particle Recovery Station. This system includes several steps of powder removal and recovery, like vacuum suction, sandblasting and powder particle sieving. Nevertheless, the recycled feedstock will not be the same as its precursor. The semi-sintering and melting process will alter the morphology and chemistry of the powdered feedstock [31]. The effects like surge in O2 content and morphology modification need to be discussed in detail.

2.2.3 Microstructure of EBM printed Ti-6Al-4V

This section details the general metallurgy of $\alpha + \beta$ phased Ti-6Al-4V which is fabricated using EBM technique. The electron beam melting process is a highly advanced manufacturing process which involves a complicated thermal processing history. The high intensity electron beam interacts with the material generating an intense heat flow in the material. This is the reason behind the complex phases and microstructure in the EBM developed Ti-6Al-4V alloys. Nevertheless, the printing parameters have a great influence on the microstructure. Variation in these parameters and post manufacturing processes can lead to the tailoring of microstructures [27], [33].

The epitaxial grain growth resulted from the intensive thermal process is the reason behind the abundance of the prior β granular structures in the EBM printed samples . The columnar grain growth is usually observed along the build direction [31], [34]. During the melting of each layer the underlying layer can be remelted. This re-melted granular structure acts as a nucleation site for the epitaxial growth of the grains [27]. Fine Widmanstätten morphologies is another common feature observed in the prior β columnar grains. Occurrence of this morphology in EBM can be attributed to the quicker cooling rates of the process [31]. The cooling process also results in the transformation of β grains to martensitic structures which is also referred to as ' α'' [30]. The cooling rate in EBM is always identified to exceed 10^4 K/s. It is always enough to form martensitic structures. Nevertheless, the constant chamber temperature can further decompose these structures [30]. Other typical features in EBM processed Ti-6Al-4V are, lamellar structures with both α and β phases and basketweave morphology . The formation of these lamellar structures are attributed to the thermal decomposition of the ' α'-martensite' and β phases, during the simultaneous remelting and cooling process [35].

2.2.4 Defects in EBM printed samples

The EBM processed samples can have various kinds of innate defects, as shown in Figure 2.6. The most common defects occurring during the EBM manufacturing are (i) lack of fusion and (ii) gas porosities. These kinds of defects are generally observed at the specimen surface which is perpendicular to the direction of the build [27]. Lack of fusion is a typical AM defect which is observed as an elongated porosity with sharp edges and tip. It is usually measured to be hundreds of micrometers. Low energy density produced by the electron beam results in un-melted powder layers. This can be attributed as the reason behind lack of fusion defects [36]. Gas porosities are generally occurring due to the entrapped gaseous molecules or the innate gas porosity in the feedstock material. However, an uneven distribution of metallic powder layers can also result in gas porosity [36]. Gas porosities are generally sized in between 1 to 100 μm [37].

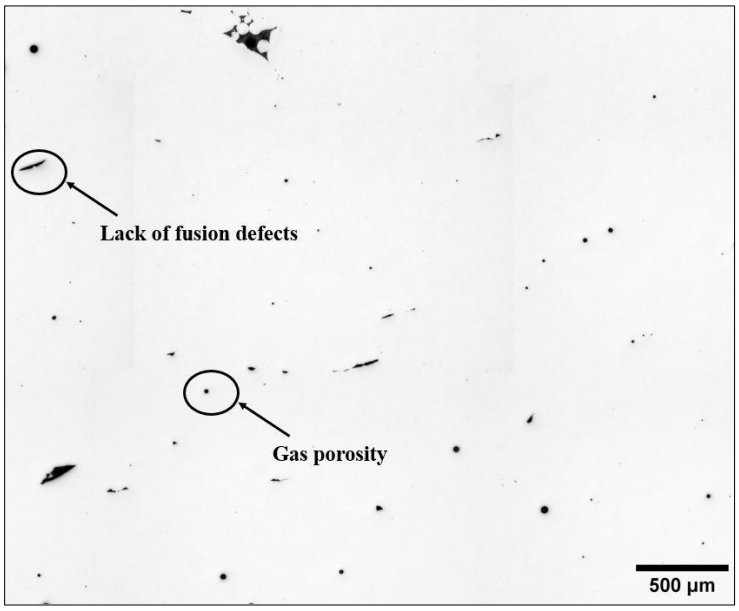

Figure 2.6: OM micograph portraying typical defects in Additive Manufacturing

2.2.5 Ti-6Al-4V powder processing for AM.

Processing the feedstock for the manufacturing process should be carried out in a controlled and careful manner. The quality, size and the sphericity of the powdered feedstock is crucial for the process and product quality [31]. The powder synthesis is usually carried out with the help of atomization techniques. The major atomization methods used to manufacture titanium powders are (i) Plasma Atomization and (ii) Gas Atomization [38], [39], [40]. The powder particles utilized as feedstock in this research are synthesised using Gas Atomization technique Figure 2.7 shows the virgin Ti-6Al-4V powder particles produced by Gas Atomization. Powder characterization is also carried out as a part of this thesis to understand the quality and features of the feedstock powder. The major variables to be investigated are; powder particle shape, Particle Size Distribution (PSD), powder microstructure, porosities and chemical composition.

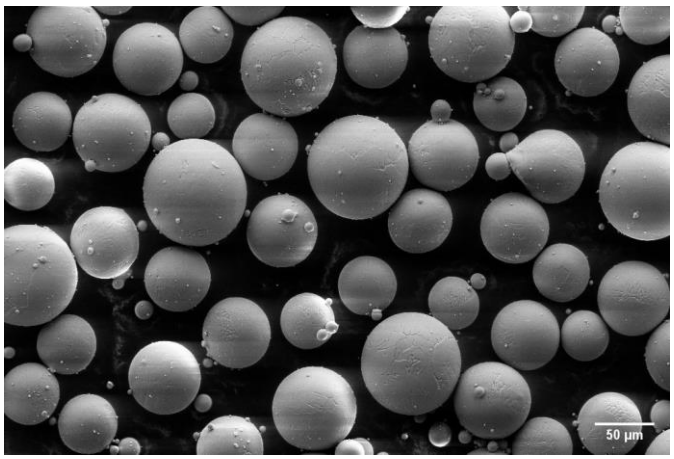

Figure 2.7: Gas Atomised Ti-6Al-4V powder particles.

2.3 Titanium based implants and other materials

2.3.1 Titanium based implants

Titanium based bone implants are found to be a promising material for biomedical applications due to its superior resistance to corrosion, high strength to weight ratio and biological compatibility. Researchers are still exploring various chemical compositions of titanium based alloys to identify the best suitable composition which is comparable in mechanical and biological properties of a bone. Nevertheless, Ti-6Al-4V still exists as the most preferred material compared to the other alternatives (β Ti alloys, Ti-Mg alloys etc). Implant materials are expected to satisfy certain standards as they are being utilized inside a human musculoskeletal system for a long period of time. Undesirable chemical reactions and effects of mechanical properties can lead to harmful effects for the user in the long run. The developed implants are preferable with a comparatively low Young's modulus, chemical and surface properties suitable to a human bone for osseointegration [11]. Figure 2.8, shows the osseointegrated and non integrated Ti based implant. The osseointegrated implant is observed to have a strong bond between the biological materials and inorganic titanium implant material [41],[42]. The mechanial and biological parameters are still subjected to research due to its importance in a biomedical implant. The excessive amount of elements like Mn and V introduced into the human body can be a vital reason for development of diseases like Alzheimer's weight loss and development of carcinogenic tissues [41].

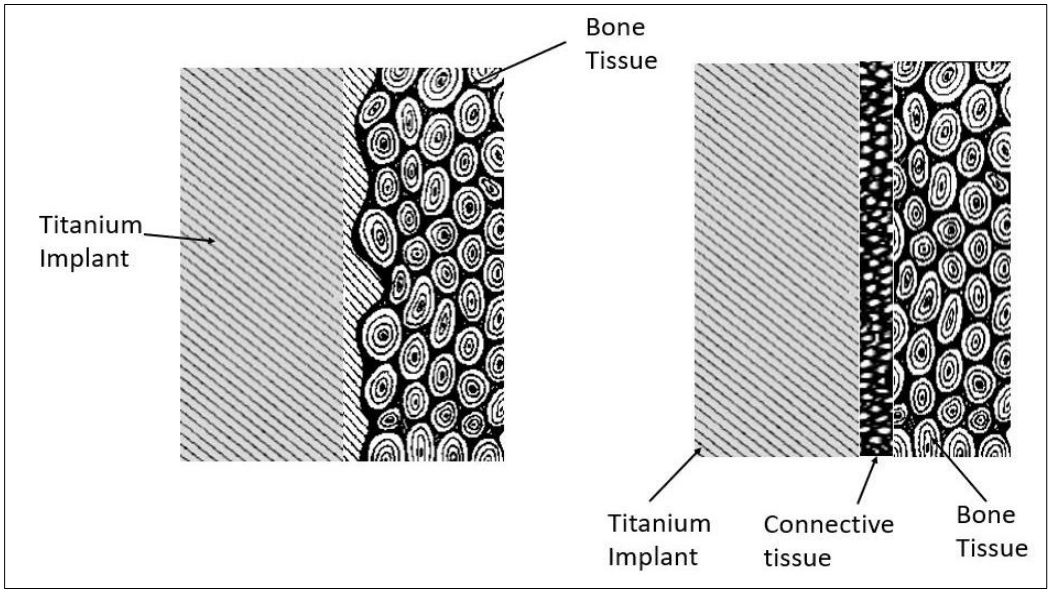

Figure 2.8 : Schematic image portraying the osseointegrated (left) and non-integrated (right) bone implant in a human body.

2.3.2 EBM of bone implants (surface geometry and roughness)

Electron Beam Melting is widely being used to manufacture biomedical implants due to its advanced manufacturing capability to produce complex meshes or porous network structure on a solid material. The process can be altered based on the requirement of final geometry and property of the implant. Due to the possibility of alteration of process parameters, the technique offers a possibility to produce person specific, customizable implants [43]. T. Stich et.al have investigated the effects of surface properties on osseointegration. The researchers experimented with various surface modifications on a titanium based implant and it was found out that the surface roughness and presence of nano and micro structured materials will influence the rate of bone tissue healing [44]. The presence of nano and micro scale structures on the implant material was found to improve the osteoconductivity or bone-implant material interaction rate in a significant manner.

EBM manufactured samples are generally found to offer a rough topography with respect to other manufacturing techniques like LB-PBF. The presence of partially melted loose powders on the implant surface might be beneficial for increasing the topological aberrations which can be advantageous for improving the rate of bone tissue healing to a notable extent. The possibilities to produce complex geometrical shapes allows printing of porous network structure [24], [41].

2.4 Characterization techniques and their common principles.

2.4.1 Optical Microscope.

Optical microscopy is a conventional method utilized to analyze the sample surface. The equipment is used to picture a two dimensional topographic image of the sample surface. The working principle of an optical microscope is given in Figure 2.9. The equipment makes use of visible light and several sequences of lenses. The light passing through these sequences of lenses assists in obtaining a magnified image of the focused object [45]. There are two basic types of light optical microscope: compound and simple microscope. The basic working principle behind these microscopes is the reflection of light from the object. The reflected light which passes through the sequence of lenses will generate an inverted magnified image of the focused object [45].

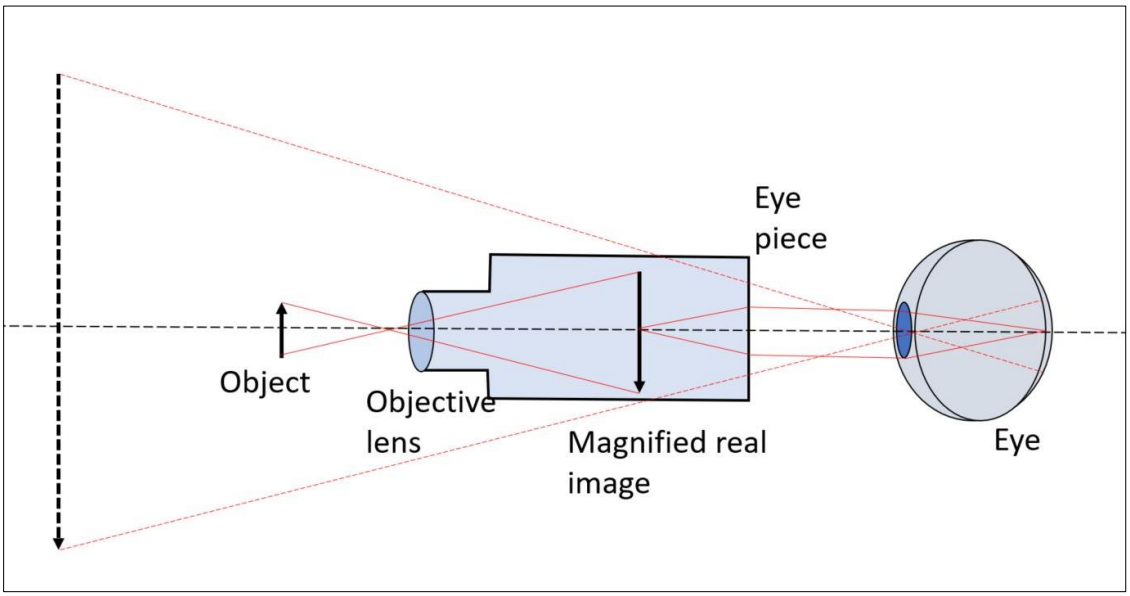

Figure 2.9 : Working principle of an Optical Microscope.

The major components of an optical microscope are (i) mechanical stage (ii) multiple objective lenses (iii) rough and fine focusing knobs (iv) eyepieces (v) light source and (vi) condenser The light source is a critical component to irradiate the sample placed on the mechanical stage [45], [46] ,which can be moved in several directions. This assists in focusing the beam on the relevant spot [46]. The microscope consists of several objective lenses like; 5x, 10x, 50x and 100x. The eye piece is usually 10x. The beam is focused on the etched or polished surface and the focal length is adjusted by using the rough and fine tuning knobs. The microscope has an image resolution limit of approximately 1 μm. The magnification can range upto 1500x. Nevertheless, the equipment cannot be utilized for analyzing the crystallography and chemistry of the samples [45].

2.4.2 Scanning Electron Microscope

In Scanning Electron Microscope (SEM), the focused electron beams will irradiate the surface and interact with the molecules/atoms present in the sample. The signals produced by these interactions are measured by using a set of detectors [47]. There are various electron sources,

like a single crystal tungsten needle and filament made of tungsten. The SEM can be classified based on the source of electrons. It can be classified into two different categories; Schottky Field Emission Gun (FEG's) and Thermionic gun. The FEG source will provide a higher resolution when compared to Thermoionic guns [27].

Figure 2.10 shows the working principle of SEM. In the tungsten filament source, the Primary Electrons (PE) are accelerated by means of continuous heating of the filament, until sufficient energy is transferred to the electron to overcome the potential hindrance offered by the filament atoms [48]. In the single crystal ZrO2 coated tungsten needle, the electric field energy is applied to the crystal tip. This intense electric field assists the primary electrons to leave the tip [47] and then focus on the sample surface (which acts as an anode). The voltage of the electron beam can be adjusted within a range of 0.1 to 50 kV [27], [47], [48].

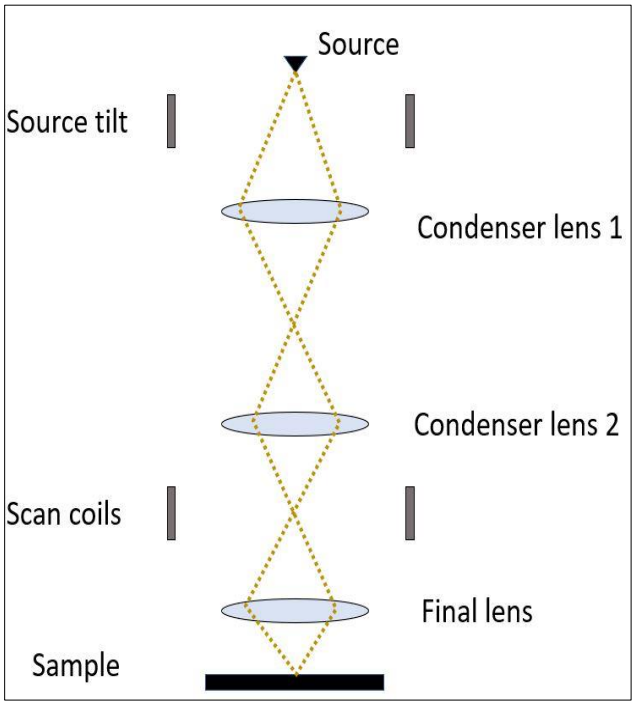

Figure 2.10: Working principle of a Scanning Electron Microscope.

The produced electron beams are passed through parallel condenser lenses, which are typical electromagnets. The setup includes several apertures which helps in focusing and narrowing the beam [48], [49], [50]. The deflection coils placed at the end of the beam column is another major component of an SEM. The repelling force generated by the current applied on the deflection coils is assisting in shifting the PE according to the scanning requirement. Selective scanning is possible by this tilt and shift of the beam. The distance between the focused sample surface and the pole piece (lower tip of the beam column) is referred to as the Working Distance (WD) [47], [48].

Primary electrons hitting the sample will generate several interactions between the electrons and the sample surface. Figure 2.11 depicts the tear drop shaped electron - sample interaction. Several types of signals are produced as a result, including, secondary electrons (SE), backscattered electrons (BSE), characteristic X-Rays etc [48], [51].

Secondary electrons are emitted from the topmost surface of the sample (few nanometers in depth) as a result of electron sample interaction. These electrons with a comparatively lower kinetic energy are detected by means of an SE detector, which converts them into signals that can be processed into images. SE electrons can give the surface details of the sample [27].

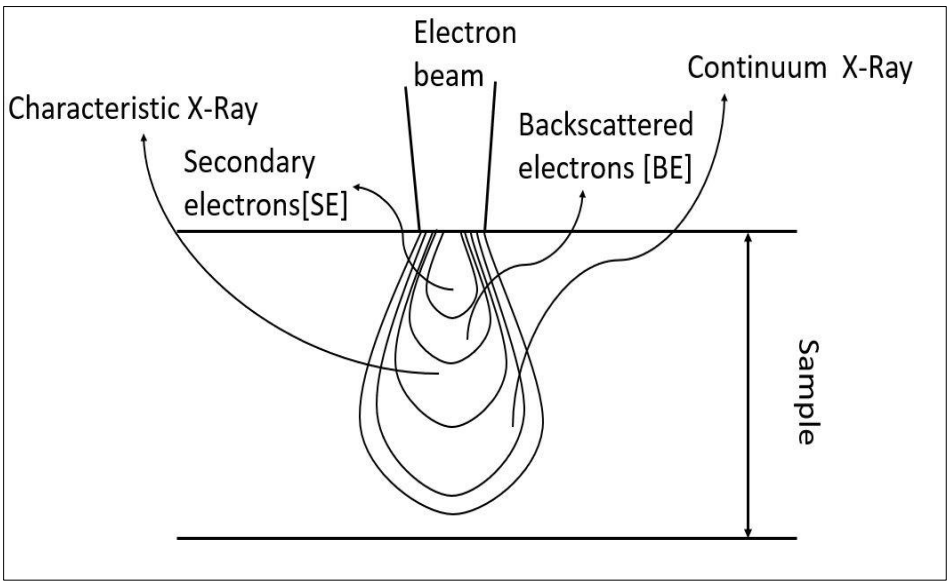

Figure 2.11: Interaction volume generated by the electron beam and emission region of various signals.

BSE electron is different from the SE electron. After hitting the sample surface, some of the primary electrons get scattered back. These electrons undergo numerous deflections and have a comparatively higher kinetic energy. The number of scattered primary electrons is directly proportional to the atomic number of the interacting phase. The BSE detector collects these scattered primary electrons and generates a signal. Thus, a composition contrast or 'Z contrast' is obtained. In the developed BSE image, the brighter regions indicate the phases with higher atomic number while the darker region indicates the phases with lower atomic number.

The parameters for imaging determine the quality of the SEM image. Optimum parameters including the voltage of electrons, WD, aperture size and type of detected electrons play an important role in the relevance of the image [48].

2.4.3 Energy Dispersive X-Ray Spectroscopy

Electron microscopes are attached with another component to evaluate the elemental composition of the specimens subjected to analysis. This equipment known as Energy Dispersive X-ray Spectroscopy or EDS can be utilized simultaneously with imaging. The analyzed X-rays are emitted from the specimen surface during the inelastic interaction of the primary electrons and the specimen electrons. The different kinds of X-Rays produced during this process are X-Ray continuum (popularly known as Bremsstrahlung) and characteristic X-rays. The former one is resulting from the de-accelerated PE electrons, as a result of PE- sample

electron interaction. Due to this, the spectrum energy is comparatively low and will not contain any specific information about the constituent elements of the sample.This lower energy of the spectrum can be explained by the Plank's wave energy equation which states a reduction in spectrum energy with the electron velocity [51], [52].

Nevertheless, the characteristic X-rays are useful for elemental analysis. These X-Rays provide information specific to each element and can be used for EDS analysis. This characteristic X-ray spectrum is arising from primary and sample electron interaction, resulting in the ejection of a sample electron. The void created by the ejected electron is filled by another electron from its outer shell thus, producing a characteristic X-ray [51], [53].

Each atom is surrounded by several orbital shells, namely, K, L, M, N, O etc. The characteristic X-ray spectrum can be named according to the movement of electrons from one shell to another. For example, the X-ray produced during the movement of an electron from outer L shell to the K shell is labelled as Kα [27], [51].

This generated characteristic X-rays are detected by means of a highly sensitive detector doped with semiconductors (ref SEB). The detector assists in generating a plot showing the intensity or number of counts of each X-rays versus its energy. Optimum parameter choice is essential for EDS analysis to obtain trustworthy results [51], [53], [54].

2.4.4 X-Ray Photoelectron Spectroscopy

Surface chemistry of the materials can be characterized by utilizing this technique called X-Ray Photoelectron Spectroscopy (XPS). It is also referred to as Electron Spectroscopy for Chemical Analysis (ESCA). Various information such as the surface elemental composition and elemental composition along the depth of the specimen, especially the chemical state of the elements can be attained through this technique [55].

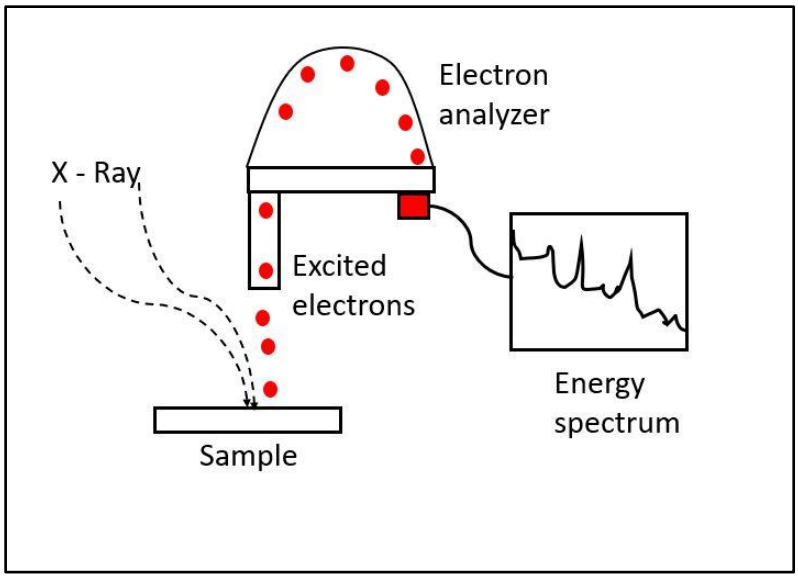

Figure 2.12: Working principle of an X-Ray Photoelectron Spectroscopy.

Figure 2.12 shows the working principle of an XPS. The XPS setup consists of several components like an electron detector, a lens, and a specimen stage. The setup is maintained in a vacuum environment (about 10^8 Pa). This helps to evade any possible contamination to the specimen surface. In this technique, the specimen surface is irradiated with X-rays. This results in emission of electrons from the sample surface. The energy (kinetic energy - E_k) of the emitted electrons, called photoelectrons, are measured by means of an electron detector [55], [56], [57]. The X-rays for irradiations are generated with the help of a metal anode and a heated filament. There exists a voltage variation between the anode and filament, and this results in generation of electrons from the filament to the anode. This irradiation of electrons on the anode will result in a generation of X-rays. Different types of anodes are used in an XPS setup. One of the most commonly used anode is Al, which produces a Kα signal of energy 1486.6 eV. Other than this, MgKα (1253.6 eV) sources are also used in some setup [57]. The generated X-ray is focused on the specimen subjected to analysis. The irradiation results in ejection of photoelectrons from the inner shell of the specimen atom. The kinetic energy of the ejected electron is measured using the analyzer. The photoelectron binding energy can be estimated by using the general equation below (Eq 2.1) [57]:

$$E_B = h\nu - KE - \varphi \quad (2.1)$$

As shown in Eq 2.1, binding energy (E_B) can be calculated by substituting the values of kinetic energy (KE), X-ray photoelectron energy ($h\nu$) and φ (spectrometer work function).

Various photoelectron peaks are notated in the form nl_j, according to the angular momentum (l), principal quantum number (n) and total angular momentum (j) of each electron. For example, $2p_{1/2}$, 1s are some notations used for photoelectron peaks. Three major purposes of the XPS instrument are; (i) Chemical composition analysis, (ii) Chemical shift of the element and (iii) depth profiling[55], [58], [59].

2.4.5 X-Ray microtomography

X-Ray microtomography or micro-CT is a technique which is extensively used nowadays for biological analysis. It is a miniature adaptation of the popular cone beam computed tomography technique. Figure 2.13 shows the working principle of a X-Ray microtomography setup. The technique makes use of X-Ray images which are compiled together to produce a real time 3D model of the sample subjected to analysis. It is non-destructive and can be used to examine the topological and internal details in the subject specimen. The setup consists of an X-Ray generator which illuminates the sample placed on a rotating stage. The rotating stage equipped with a step motor will ensure the exposure of X-rays on the entire surface of the sample subjected to analysis. The detector placed on the opposite side of the rotating stage collects the signals from the sample regions. The detected signals are developed into images. The present investigation is conducted using a Skyscan 1172 micro-CT setup from Brukers. The setup has a 104 kV tungsten X-ray source and can produce 11 Mega Pixels per slice thus enabling imaging of smaller object within a range of 30mm at higher resolution [60], [61].

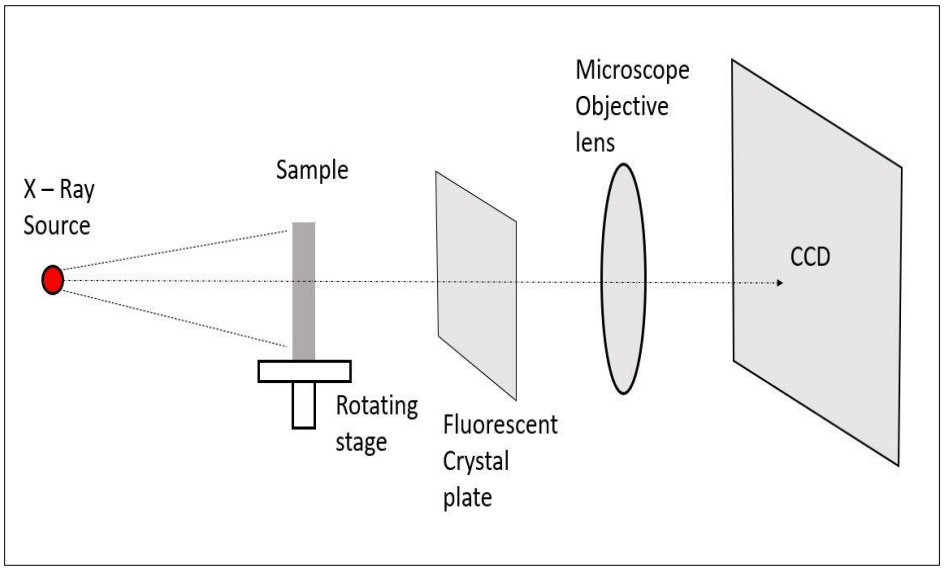

Figure 2.13: Figure exhibiting the working principle of X-Ray tomography.

2.4.6 Confocal microscopy

Confocal microscopy is an advanced analysis technique which has several advantages over the conventional compound optical microscopy. The equipment allows the user to have a control over the depth of field of the microscope and perform a systematic reduction of background noise from the developed images.The fundamental tool of confocal microscopy is the utilization of filtering methods to avoid the presence of unwanted light sources, focus errors and artifacts which introduces a variation in the depth of field of the equipment [62]. The modern confocal microscopy technique consists of several innate detector systems attached to a compound optical microscope, which are essential for the filtering. It is widely being used in biological analysis [63].

Figure 2.14 shows the working principle of a confocal microscope. A fundamental confocal microscopy setup consists of an objective lens, a laser source, dichromatic mirror, pinholes, filters and detector system. The equipment can be additionally attached with fast scanning mirrors. Argon and helium sources are widely used in the setup. Nevertheless, modern machines make use of advanced laser sources like fiber and diodes. The light emitted from the laser is focused through an array of lenses to a dichromatic mirror setup. The reflected beam of laser is focused on to the specimen surface through the objective piece. The setup consists of a pinhole which enables it to eliminate the artifacts caused by out of focus light. The amount of light entering the system can also be controlled by altering the pinhole size to a certain extent. Another important component of the confocal microscope is a systematic arrangement of scanning mirrors which aids in avoiding the over exposure of sample surface to the beam of laser [63].

The mean surface roughness values (S_a) can be calculated from the data values obtained from the machine, using Eq 2.2 [64].

$$Sa = 1/n_x n_y \sum_{j=1}^{ny} x \sum_{i=1}^{nx} |\eta(x_i y_j) \quad \text{....Eq (2.2).}$$

As expressed in Eq 2.2, Sa can be calculated using the area surface roughness data matrix $|\eta(x_i y_j)$.

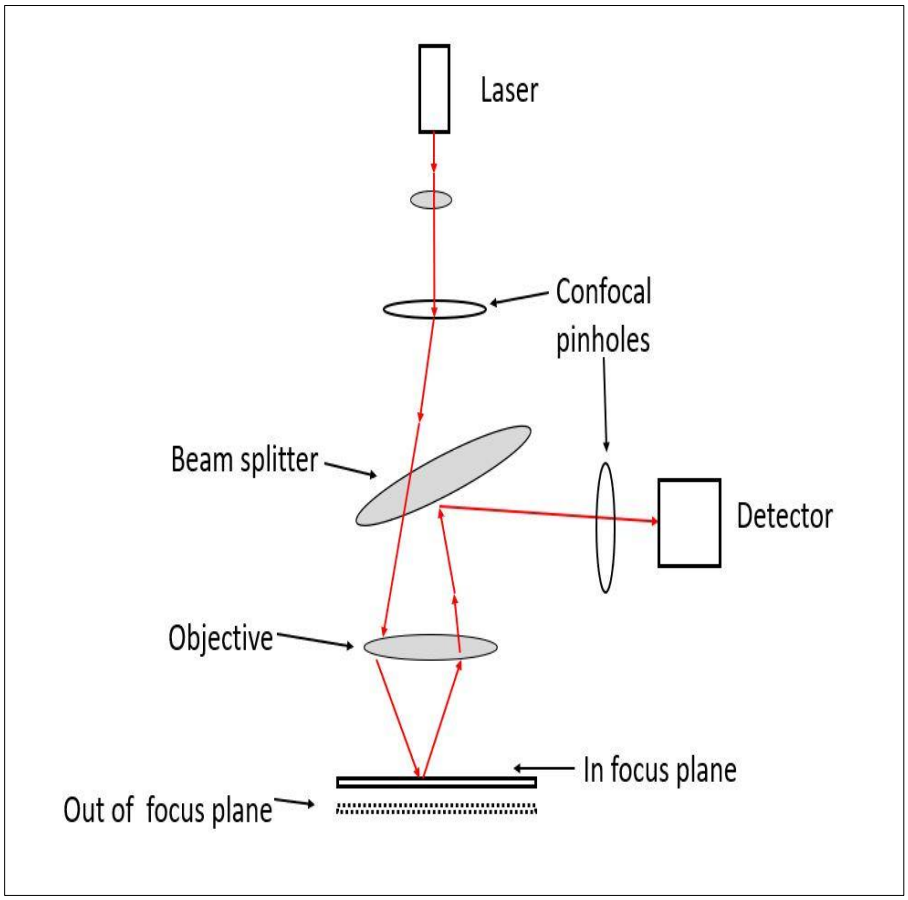

Figure 2.14: Working principle of confocal microscopy.

3.Methodology

This section of the thesis briefs about the investigation methodology of the research. The details about the samples, their preparation and characterization techniques are discussed below.

3.1 Sample details and nomenclature

The bone implant samples were provided by GE Additive (formerly known as Arcam AB) (Figure A1).The manufacturing was carried out by using three different batches of powder; virgin, one time recycled and five times recycled. These powders were used to fabricate scaffold samples at similar build design which is referred to as Theme 13 by GE Additive. Along with the fabricated samples, 100 grams of used powder sample (virgin, one time recycled and five times recycled) were also provided by GE Additive. The details of the samples and their nomenclature are tabulated below (Table 3.1).

Table 3.1 : Sample Nomenclature system

Sl No.	***Sample type***	***Sample details***	***Sample name***
1	Acetabular cup	Made from virgin Powder-Theme 13	V 13
2	Acetabular cup	Made from one time recycled - Theme 13	1x 13
3	Acetabular cup	Made from five times recycled - Theme 13	5x13
4	Powder	Virgin or fresh powder	Virgin
5	Powder	One time recycled	1x recycled
6	Powder	Five times recycled	5x recycled

3.2 Sample preparation for analysis

The samples provided by GE Additive need to be prepared according to the required standards in order to conduct the experimental investigation including microstructure, porosity analysis, XPS, micro-Ct analysis. Additionally, the powder samples are subjected to morphological and microstructural analysis.

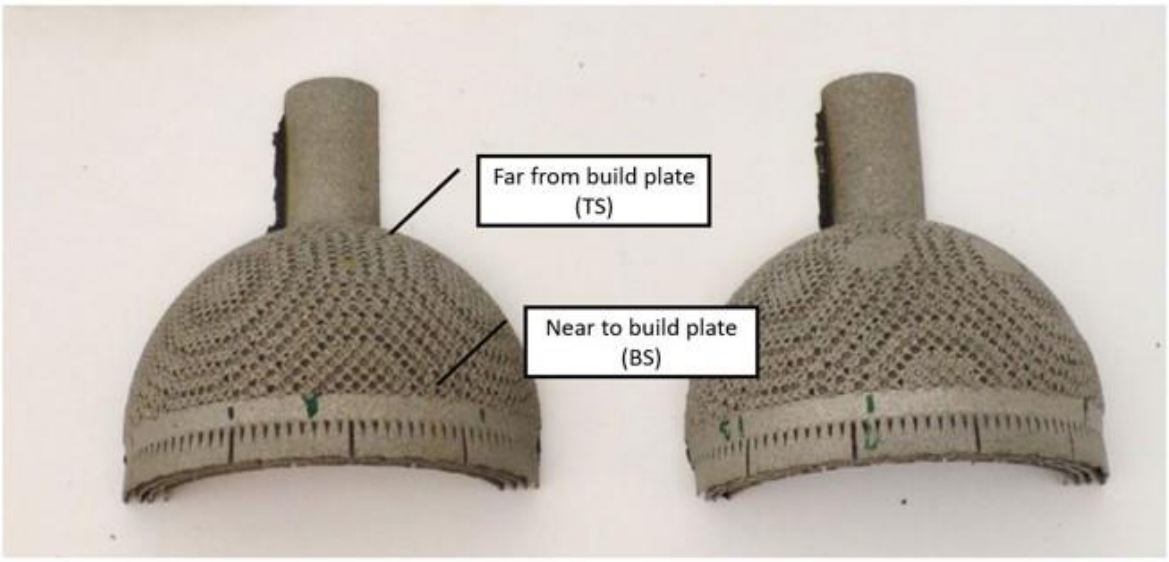

Figure 3.1: Sectioned V13 implant with marked top and bottom regions.

3.2.1 Sample preparation for porosity and microstructure analysis of implants.

The EBM printed acetabular cups provided by GE additive should be sectioned and polished in order to carry out microstructure analysis. The analyses were performed at the region near the build plate (BS) and far from the build plate (TS), in order to identify the variation with respect to increase in build height (Figure 3.1). The lattice regions for analysis were extracted from the surface of the implants, at the middle region of the implant. Solid samples were extracted from similar locations to have a comparitive study between lattice and solid samples. The lattice samples were not subjected to microstructural variation with respect to building height. The provided samples were sectioned using a Struers Discotom-2 metal cutting machine equipped with a SiC cutting wheel (Grade :10S25). The sectioning of titanium alloys can lead to formation of undesirable oxide layers on the specimen surface. Water was used as a lubricant inorder to reduce the heat generation during sectioning, thus lowering the oxidation reaction on the metal surface. The extracted samples for analysis were taken from the same regions on the build to have a precise comparison.

The samples were mounted using carbon containing Polyfast powder in order to enable electrical conductivity for the mount. The mounting process was carried out using the CitroPress-20 manufactured by Struers. The sectioned samples were grinded flat using a SiC grinding paper (Grade #220) until the surface anomalies from sectioning were removed.

Table 3.2 : Parameters for polishing steps as recommended by Struers

Grinding/Polishing step	Plane Grinding	Fine Grinding	OP
Used Surface	MD Piano	MD Largo	MD Chem
Size and type of abrasive	#220, Diamond paste	9 µm, Diamond paste	0.04 µm, Silica colloid
Suspension name	Water	Diapro Allegro/Largo	10% H2O2 + 90% OP-S
Force (N)	25	20	30
Rpm	300	150	150
Time (min)	8 -10	8 - 10	5 - 10

The mounted samples were then taken for the final step which includes grinding, fine grinding and chemical polishing.Table 3.2 lists the parameters selected for the grinding and polishing process. The polished samples were rinsed with running water, isopropanol and ethanol, followed by cleaning using an ultrasonic bath for 20-25 mins, using ethanol as the solution. For microstructural investigation, polished samples were etched by rubbing a cotton swab dipped in standard Kroll's reagent (1-2%HF+3% HNO_3+ H_2O) until the sample surface turned cloudy.

3.2.2 Sample preparation for XPS analysis of implants.

XPS analysis was carried out on both the solid surface and the porous network or lattice structure. The bottom region of the acetabular cup was chosen as the analysis region due to the presence of both solid and lattice structure at that region. The extracted samples were sectioned from the same region of the build using a Struers Discotom-2 metal cutting machine followed by cleaning using an ultrasound bath for 20 min using isopropanol solution. The cleaning procedure was repeated using ethanol, for 15 mins. The samples were then carefully dried using nitrogen gas to avoid contamination. The prepared samples were mounted using a carbon tape.

3.2.3 Sample preparation for geometrical analysis of implants.

The geometrical analysis on the porous lattice structure was carried out using a micro-CT machine. The samples for analysis were extracted from three different regions in the acetabular cup: top, middle and bottom. They were then grinded using a SiC paper (Grade: #220) to obtain a flat bottom surface. The samples were maintained at a dimensional tolerance of 10 mm in thickness. The grinded samples were cleaned in an ultrasound bath for 15 mins using ethanol.

3.2.4 Sample preparation for surface roughness analysis.

The acetabular cups were sectioned into two halves. The lattice structure on one half of the scaffold sample was used for the roughness measurement. First, the bottom of the sectioned half was grinded flat using a SiC paper of grade #220. Subsequently, it was carefully cleaned in an ultrasound bath for 20 mins using isopropanol to remove surface contaminants.

3.2.5 Sample preparation for powder microstructure analysis.

The powder samples were provided by GE Additive in glass containers. The powder was carefully mixed with equal portions of fine Polyfast powder, grinded using mortar and pestle. The mixture was mounted using a Struers Citopress-20. The mounted samples were grinded and polished using the Struers TegraPol-31. The three-step polishing process (plane grinding, fine grinding and chemical polishing) was carried out by using the similar steps mentioned in Table 3.2. The load was reduced to 15 N and the time for each step was reduced to 1.5 min. The polished samples were rinsed using water and isopropanol to remove the remaining silica particles from the surface. The samples were rubbed with a cotton swab dipped in Kroll's reagent for 20 sec inorder to etch.

3.2.6 Sample preparation for powder morphology analysis.

The powder samples provided by GE Additive were mounted on a carbon tape for morphological analysis. The powder samples were spread on the carbon tape to get an even distribution. The remaining loose powders were blown out. The carbon tape mounted with the powder specimens was carefully placed on the mount.

3.3 Sample characterization

3.3.1 Microstructural characterization and composition analysis (EDS) of implant samples

In the present investigation, microstructural characterization at lower magnification is carried out on the plan perpendicular to the building direction by means of a light optical microscope (Zeiss Axio Imager M2m), controlled by the Zeiss Zen Core 2.5 software. A Scanning Electron Microscope (SEM) was used for high magnification images. The Zeiss-LEO Gemini Field Emission Gun (FEGSEM) controlled by the Zeiss SmartSEM software was operated with an acceleration voltage of 10 kV and an aperture of 30 µm. A standard SE and InLens detectors were chosen for imaging the topography. A BSE detector was also used to get a chemical contrast of the area of interest.

The α-lath thickness was measured on SEM images at 2000x at 5 different locations using the ImageJ software. The measurement scale is calibrated with the help of the scale bar in the SEM image (in microns). The image was then cropped using the crop tool in ImageJ to specify the region of interest and avoid the annotations. The cropped image was thresholded (regular binary threshold) to define the α and β phase. The nearest neighbour distance between the beta phase was measured to determine the α lath thickness. The process was repeated at various orientations in images at different locations to get an average α lath thickness.

A composition analysis on the different phases was carried out in the SEM equipped with the Oxford X-mas EDS detector. Different phases like α and β were analyzed inorder to determine

the compositional variation with respect to powder recycling. An aperture size of 60 µm and acceleration voltage of 10 kV was chosen for the analysis. The working distance (WD) was fixed to 8.5 mm for all the analysis. A point EDS analysis was performed on the SE images taken using the FEG-SEM at 3000x magnification.The evaluation was performed using the Aztec software from Oxford Instruments.

3.3.2 Porosity measurement of implant samples

The porosity measurement was performed on optical imagesfrom polished samples without being etched using the Zeiss Axio Imager compound light optical microscope. The stitching function in the Zeiss zen Core software was used to stitch twelve 50x magnified images to generate the entire specimen surface. The stitched images were evaluated using the Image J software, following similar procedures for the measurement of α-lath thickness. scale was calibrated by measuring the scale bar from the instrument. The region of interest was defined by cropping out the specimen edges to avoid measurement errors. A binary threshold was applied on the image and a fixed threshold limit of 110 was chosen for all the measurements. The porosity fraction in the sample was measured by the built-in particle analysis setup in the software. A particle analysis limit of 5 µm was applied inorder to avoid undesirable speckles which can be counted as a pore by the software.

3.3.3 X-Ray Photoelectron Spectroscopy (XPS) analysis of implant samples

The XPS analysis on the solid and lattice implants samples were performed using the PHI5500 XPS instrument. A monochromatic X-ray source of AlKα having an energy of 1486.6 eV was used to irradiate the sample. The machine was operated with a power of 25 W, beam size of 100 µm and a take off angle of 45° in a vacuum setup of 10^{-7} Pa. Depth profiling was performed by Ar^{+} ions sputtering with the raster size of 2 x 2 mm and ion beam voltage fixed at 2 kV.

Various spectral data were extracted from the analysis, namely, survey spectra, high resolution spectra or multiplex scans of elements of interest and depth profiling. The measured plots were analyzed using the Multipak software.The survey scan for identifying the surface chemical composition was performed at a binding energy range between 0 - 1100 eV. The multiplex scans were performed for - Ti2p, $V2p_{3/2}$, Al2p, C1s, N1s and O1s. The oxidation states of the elements were identified from these peaks.

The depth profiling was performed for Ti2p, Al2p, V2p3, C1s, O1s and N1s to identify the oxide thickness and cation enrichment in the solid and lattice samples. The etch rate for the chosen parameters was calibrated to be 52 Å/min by using Ta_2O_5 with known thickness as a reference material.

Based on the depth profile, the oxide thickness was calculated at the point where the oxygen intensity was reduced to approximately 50 % of the maximum value. The sputter time (min) at the particular point was multiplied with the callibarated etch rate (52 Å/min) in order to obtain the thickness of the oxide layer.

3.3.4. Geometrical analysis of implant samples

The geometrical analysis of the lattice sample was performed by means of a SkyScan 1172 made by Bruker, Belgium using tungsten generated X-Ray sources. The equipment was operated at a current of 100 uA and acceleration voltage of 100 kV. The vital energy X-rays irradiating the specimen surface are eliminated by using an Al and Cu filter. The specimens subjected to analysis were mounted at a distance of 93.8 mm from the X-ray source, while the camera was placed at a distance of 208.89 mm from the source. The samples were rotated at 360° while the analysis was performed. A step size of 0.4◦ was chosen for the rotation. . The samples were exposed to the source with an exposure time of 205 ms. The camera setting was kept constant at 1000 x 668 pixels with a frame averaging of 4 and 15.76 µm resolution. The approximate X-ray imaging time for each sample was approximately 25 min.

The analyzed data was reconstructed using a Version 1.6.9.8 NRecon software. Reconstructed data of the samples were aligned to keep the investigated lattice sample at a desired orientation in DataViewer. The orientated data was analysed in CTAn software. An image of the sample from the optimal location in the slice is selected and binary thresholded at global setting. The thresholded images were processed with the opening plug-in. The notable speckles present in the images were removed with the remove while speckles plug-in. The processing steps were essential to remove the presence of artifacts in the images. The analysis was performed at the region of interest by keeping fixed parameters of 5 pixels and 1 voxel for both 2D and 3D space respectively. The morphometric measurements plug-in was used to measure the lattice strut thickness distribution and average lattice strut thickness of the implant. The CTAn software was also used to generate a 3D model of the analyzed specimen from the processed data set. The generated 3D model was saved in a '.ctm' format and was opened using the CTvol software.

3.3.5. Roughness measurement of implant samples

The roughness measurement was carried out at three locations at the middle and bottom position of the implant samples using a SensoFar Neox microscope with a Nikon-EPI 20x objective lens. A confocal fusion method was used by the equipment for the analysis. A 6 x 6 stiching function was used to generate a sufficient window for analysis. The images were processed in various stages. A polynomial deg 3 setting was used to remove the form. The artifacts were filtered out using a median denoising 5 x 5 spatial filtering method. The non measured points were filled in during the processing which was carried out with the least square method level. All the evaluations were carried out using the Mountain Map 8 software.

3.3.6 Microstructure analysis of powder samples

Microstructure of the powder samples were imaged using the Ziess Leo Gemini FEG-SEM at an acceleration voltage of 10 kV and the working distance of 8 mm. A standard SE detector with an aperture size of 30 µm was used to get the topographical information of the etched powder samples.

3.3.7 Morphological analysis of powder samples

The morphological features of the powder samples were investigated using the Zeiss Leo-Gemini FEG-SEM at an acceleration voltage of 10 keV and aperture size of 30 µm. The working distance was kept at a constant of 8 mm.

3.3.8 Powder composition analysis

The elemental composition of the powder samples was evaluated with an Oxford X-mas EDS detector attached to the FEG-SEM. The analysis was performed on both carbon tape mounted and polyfast mounted, polished powder samples. The experiment was carried out at different acceleration voltages ranging from 10 - 20 kV. A constant aperture size of 60 µm and working distance of 8.5 mm was maintained for all the experiments. The analysis was performed on 10 powder particles to determine their average elemental composition.

4. Results and Discussion

4.1 Powder samples

Figure 4.1 portrays the morphological features of virgin, 1 time recycled and 5 times recycled powder samples. Secondary electron imaging was used to analysis the surface features on each powder batches. The virgin powder samples are found to have a relatively smooth surface compared to the recycled powder batches. The powder surface is found to be more spherical compared to the recycled powders. Small globular particles can be observed on virgin powder particles which are referred to as satellites (Figure 4.1 (a)) [65]. In (Figure 4.1 (b)), a striated dendritic feature is observed on the powder surface. Grain boundary can be observed on the smooth virgin powder surface. The recycled powder surface are deformed and rough due to which the grain boundaries can not be observed [66].

It can be observed from the figure that, in the 1 time recycled powder particles, surface deformation is occurring in a notable extent. The powder sphericity has been reduced and the particle have notable chipping and defects on the surface (Figure 4.1 (c)). The presence of satellite particles is reduced in the 1 times recycled powder sample, compared to virgin powder. Surface deformation is also, observed on the elongated powder particle from 1 time recycled powder batch (Figure 4.1 (d)).

The powder particles from 5 times recycled batch (Figure 4.1 (e) and (f)) were observed suffer severe deformation too compared to 1 time recycled and virgin powder batches. The satellite particles were observed to be nearly absent in this batch. The development of surface defects and chips can be observed in Figure 4.1 (e)). It is evident that the chipping is severe in 5 times recycled powder. The surface deformation is occurring because of powder melting and recycling process. The repeated melting and remelting happening on the powder particle can result in formation of rough patches and chipping on the powder surface. The sieving process and exposure to high temperatures can also affect the surface of powder particles. Thus, the deformation rate will be increasing with increase in recycling number of powder batches [66]. Due to repeated process of melting, the powder particles tend to break and get deformed. This is most probable in 5 times recycled powder batches which are recycled more number of times. According to the literature, the absence of satellite can be attributed to the blasting and sieving process during recycling, which break down these nanosized agglomerates [65].

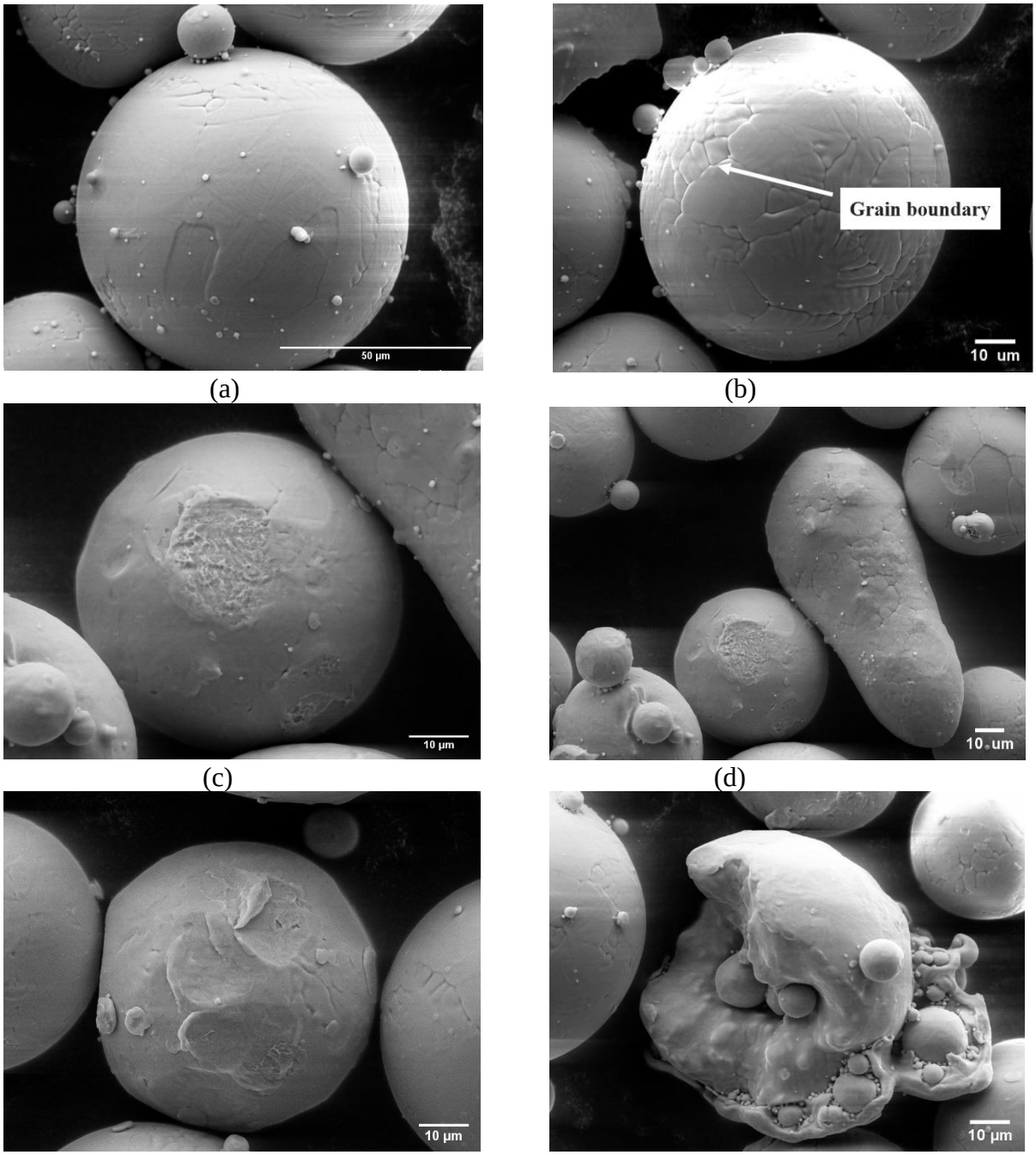

(a) (b)

(c) (d)

(e) (f)

Figure 4.1: Micrographs showing (a) virgin powder particle with satellites (b) virgin powder morphology (c) deformed 1x recycled powder (d) elongated 1x recycled powder particle (e) deformed 5x recycled powder and (f) broken 5x recycled powder particle

Particle size distribution (PSD) is an important factor which can alter the porosity percentage and size of the developed pores to a considerable extent [66]. Figure 4.2 portrays the PSD of virgin, 1 time recycled and 5 times recycled powder. It is evident from the graphs that, 1 time recycled powder (Figure 4.2 (b)) exhibits an increase in average diameter of powder particles compared to virgin powder. The 5 times recycled powder also exhibits a similar trend. This can be attributed to the high chamber temperatures and recycling process which results in clustering of powder particles. The satellite particles are broken down during the recycling

process [66]. The PSD is concentrated at a specific range (40 – 100 µm) for all the powder samples. The size distribution of particles are observed to shift towards the right side, thus showing an increase in the average diameter of the powder particles. This effects the powder layer thickness, thus leading to uncomplete melting and generation of process induced gas porosities [65], [66].

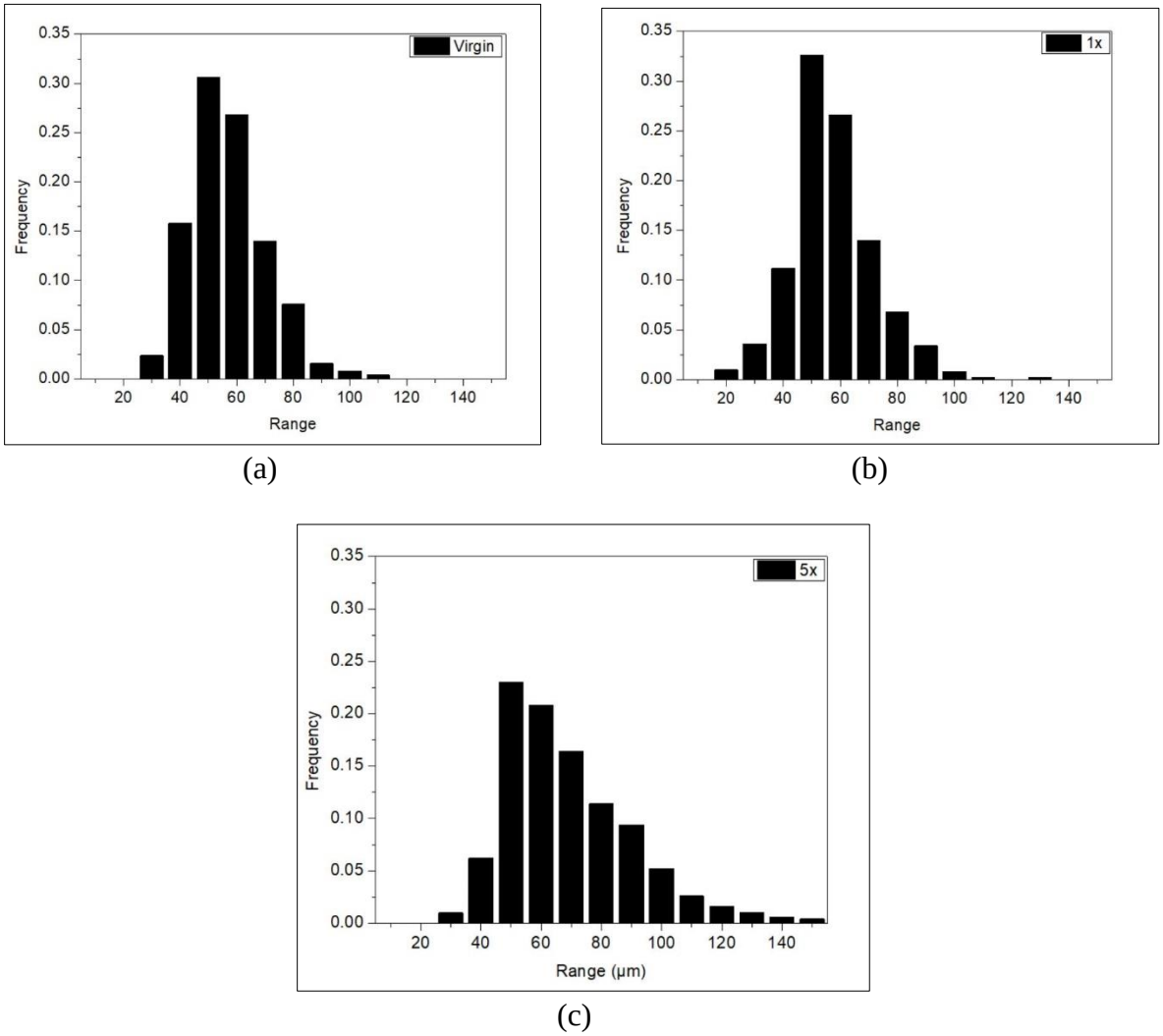

Figure 4.2: Plots depicting the particle size distribution of (a) virgin powder (b) 1x recycled powder (c) 5x recycled powder.

The microstructural analysis of virgin powder revealed the presence of sharp needle like structures (Figure 4.3). This was the only phase detectable in the virgin powder microstructure.

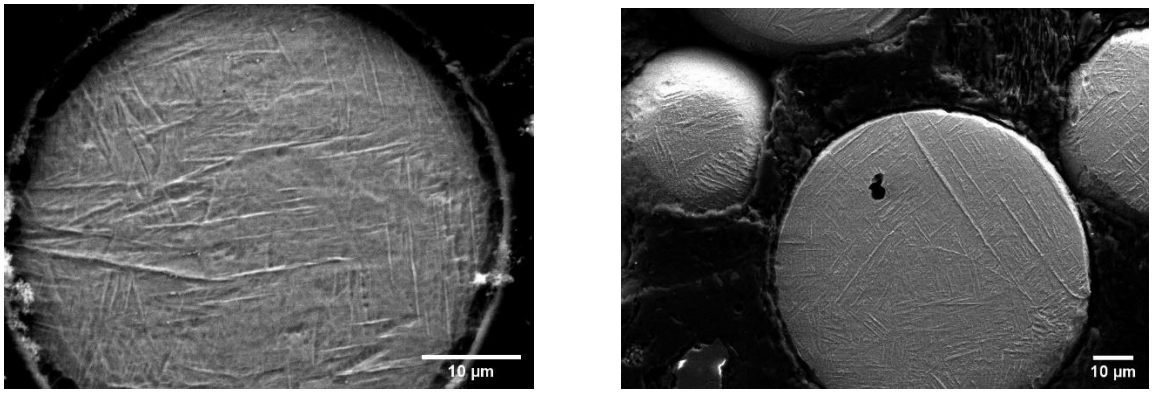

(a) (b)

Figure 4.3: SEM micrographs depicting (a) martensitic structure of virgin powder particle (b) internal porosity in virgin powder particle.

The needles are martensitic phases which are measured to be 2 – 40 µm in length, approximately. These needles are observed to be randomly orientated in the microstructure. Martensite phase is obvious in the virgin powder due to the sudden rapid quenching of atomized droplets of alloyed melt by a flow of gas, during Gas Atomization process. This results in formation of martensitic phases. The powder particles have internal porosities (Figure 4.3 (b)) which was developed during the powder manufacturing process [27], [67].

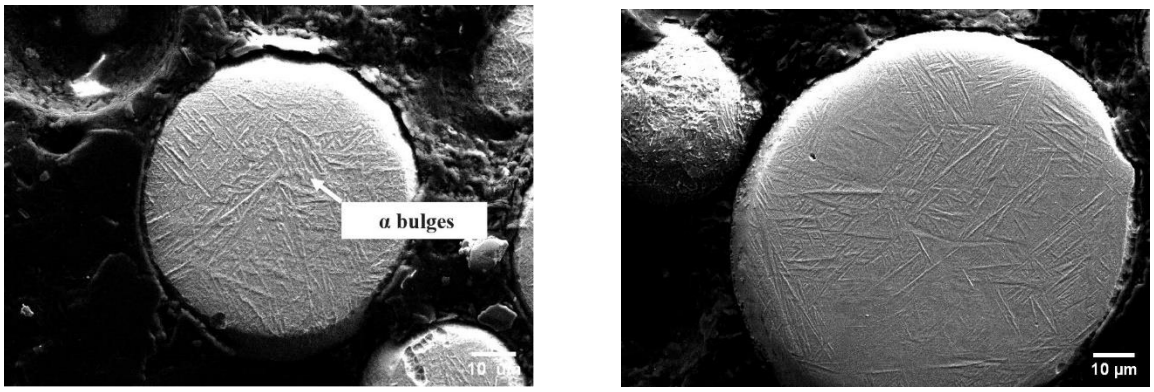

(a) (b)

Figure 4.4: SEM micrographs depicting (a) microstructure of 1x recycled powder particle (b) fine martensitic needle and porosities in 1x recycled powder particle.

Figure 4.4 portrays the microstructure of 1 times recycled powder sample which possess a martensitic structure similar to virgin powder. However, a slight variation is observed. There is presence of bulge like structures, which is expected to be α phase. Gas porosities are evident in the 1 time recycled powder samples, aswell. The microstructure of 5 times recycled powder sample is portrayed in Figure 4.5. It is evident that the microstructure is different compared to virgin and 1 time recycled powder samples. Bright white particulate like structures which were identified to be β phases, with EDS analysis, can be observed in the microstructure. The needle like acicular martensite is also observed in 5 times recycled powder microstructure along with bulge like structures, which is expected to be α phase. This phase will be further discussed in the following sections. The martensitic needles are found to obey the Burger's orientation relationship [27], [33], [68]. There is presence of large process induced gas porosities in 5 times recycled powder (Figure 4.5(b)).

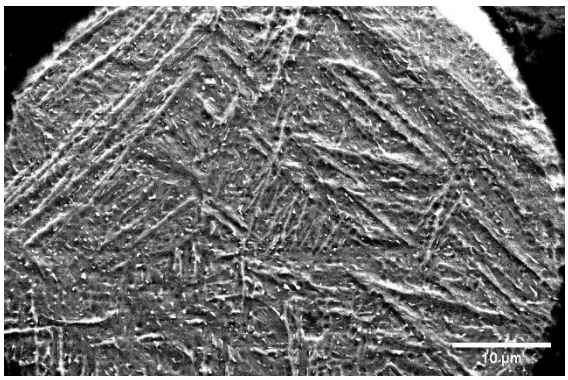

(a)

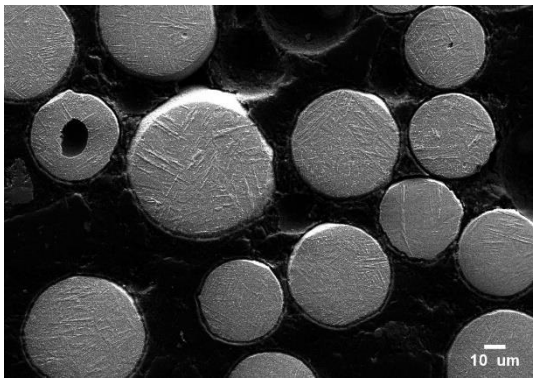

(b)

Figure 4.5: SEM micrographs depicting (a) microstructure of 5x recycled powder particle (b) internal porosity in 5x recycled powder particle.

The composition analysis was conducted on both ground and polished powder samples and the one mounted on carbon tape. Notice the former one revealed the powder composition at the interior region of the powder while the later one provided this information at the powder surface. At the interior region, the oxygen content was found to be increasing after recycling in general (Table 4.1) This is an effect of recycling process and powder remelting in the EBM chamber [69]. However, compared to 1 time recyling the 5 times recycled powder is found to have a lower concentration of oxygen. It should be mentioned that, EDS measurement is complicated when quantifying light elements like oxygen. This might be the possible reason for this contradiction [27], [51].

Table 4.1. Average powder composition (Polished powder, ETH 10 kV, WD - 8.5mm) (wt-%)

Phase	Ti	Al	V	O	Si	Fe
Virgin	87.67 ± 0.52	5.97 ± 0.19	3.87 ± 0.36	2.19 ± 0.20	0.04 ± 0.03	0.26 ± 0.33
Recycled 1x	86.62 ± 1.59	5.92 ± 0.19	3.97 ± 0.64	3.11 ± 1.40	0.05 ± 0.03	0.33 ± 0.33
Recycled 5x	87.21 ± 0.96	5.60 ± 0.21	3.85 ± 0.63	2.62 ± 1.10	0.08 ± 0.14	0.22 ± 0.34

Table 4.2 shows the composition at the powder surface from the samples which are mounted on a carbon tape. The beam voltage was kept constant at 10 kV during this analysis. The oxygen content was found to be increasing with powder recycling Moreover, an increase in aluminium content was observed, compared to the interior region (Table 4.1). This observation is a contradiction to the literature [70]. Aluminium have a lower melting point compared to titanium, and thus, have a tendency to get evaporated during the repeated melting and recycling process [71], [72]. It seems that the increasing aluminium content was contradicting this fact. This can be explained as follows. Aluminium has a high affinity towards oxygen and tends to move from the interior region towards the surface oxygen and form Al_2O_3 [55]. This can be the reason behind the increase in aluminium content at the surface with respect to a decreasing concentration at the interior region. Although, there is an evaporation in aluminium from the powder samples during the repeated melting and recycling process, as confirmed by GE Additive. This occurs in rather shallow region and cannot be confirmed by EDX, which is a bulk analysis method. In fact, the evaporation of Al has been confirmed by surface analysis method such as XPS [55], which has an information depth less than 10 nm.

Table 4.2. Average powder composition (Mounted powder, ETH 10 kV, WD - 8.5mm) (wt-%)

Phase	Ti	Al	V	O	Si	Fe
Virgin	86.95 ± 0.63	6.45 ± 0.20	3.63 ± 0.28	2.64 ± 0.50	0.05 ± 0.04	0.29 ± 0.31
Recycled 1x	86.66 ± 1.30	6.64 ± 0.61	3.61 ± 0.56	2.97 ± 0.92	0.06 ± 0.08	0.06 ± 0.10
Recycled 5x	86.37 ± 1.51	6.72 ± 0.54	3.14 ± 0.48	3.40 ± 1.13	0.06 ± 0.03	0.33 ± 0.32

The beam voltage used for analysis above was 10 kV. Inorder to get a larger depth of analysis, beam voltage was increased to 15 kV and 20 kV and the compositional results are given in Table 4.3 and 4.4. The difference is insignificant.From these analyses, it can be concluded that there is an increase in aluminium content on the surface of the powder samples.

Table 4.3. Average powder composition (Mounted powder, ETH 15 kV, WD - 8.5mm) (wt-%)

Phase	Ti	Al	V	O	Si	Fe
Virgin	86.92 ± 0.92	6.36 ± 0.56	3.62 ± 0.25	2.78 ± 0.59	0.06 ± 0.03	0.22 ± 0.10
Recycled 1x	87.12 ± 2.02	6.25 ± 0.62	3.47 ± 0.19	2.80 ± 2.02	0.15 ± 0.31	0.21 ± 0.12
Recycled 5x	86.67 ± 0.65	6.99 ± 0.70	3.36 ± 0.77	2.82 ± 0.60	0.06 ± 0.03	0.14 ± 0.16

Table 4.4 Average powder composition (Mounted powder, ETH 20 kV, WD - 8.5mm) (wt-%)

Phase	Ti	Al	V	O	Si	Fe
Virgin	86.19 ± 0.63	6.34 ± 0.27	3.57 ± 0.13	3.68 ± 0.64	0.06 ± 0.03	0.16 ± 0.05
Recycled 1x	87.02 ± 1.15	6.06 ± 0.66	3.48 ± 0.43	3.25 ± 0.56	0.05 ± 0.03	0.14 ± 0.10
Recycled 5x	85.74 ± 1.37	6.37 ± 0.71	3.44 ± 0.16	4.22 ± 0.88	0.06 ± 0.03	0.17 ± 0.07

4.2 Fabricated bone implants

The implant samples provided by GE Additive were subjected to various experimental investigations. The microstructure, porosity, chemistry , geometry and roughness of the samples were evaluated. The trailing content details about the formulated results.

4.2.1 Microstructure at low magnification

The overall microstructure and the grain orientation of the implants manufactured with different powder batches is depicted in Figure 4.6. The images were taken at a magnification of 25x. The micrograph details about the grain structure of the implants. The various grains in different micrographs can be differentiated by the variation in colour tone due to etching originated from the difference in etching rate of each phase present in the microstructure of the Ti-6Al-4V implant samples. The grains are large and elongated with irregular shape. The grains are differentiated by a pale white grain boundary. Different grains are oriented nearly parallel to the build direction of the implant samples. The large grains portrayed in the micrographs are prior β grains with an average width of 25 - 200 µm. All the implant samples were as-printed and the overall microstructure looks similar. The elongated structure of the identified grains can be attributed to the epitaxial growth during the EBM process [24], [27].

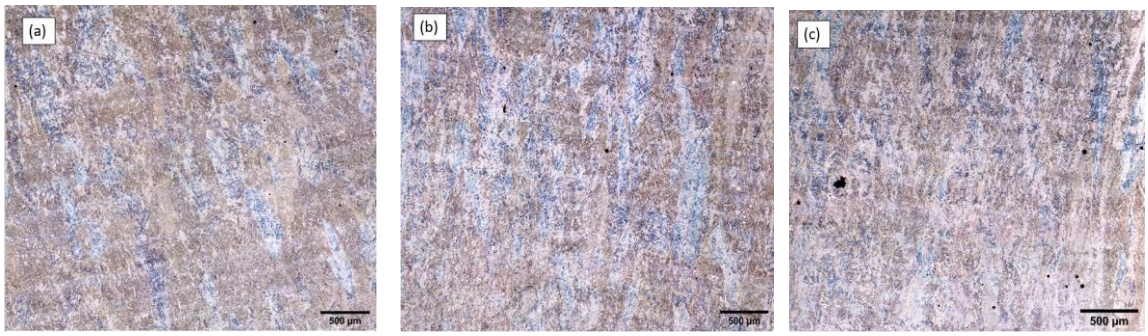

Figure 4.6 : OM micrographs depicting the grain structure of (a) V-13 (b) 1x-13 and (c) 5x - 13 implant.

4.2.1.1 Microstructure and elemental composition of solid region in V-13 implant .

Figure 4.7 portrays the overall microstructural feature on the solid section of a top region in V-13 implant. The presence of various phases which differ in shape, size and contrast of appearance was observed. The heterogeneous microstructure is arising due to the complex thermal history of the manufacturing process and the varying feed stock [27]. The powder particles used as a feedstock are significantly varying in their size distribution and morphology with respect to each other. This can have an influence on the developed microstructure of the implant. The bright features in the micrograph are the β phases which are distributed non uniformly in a dark matrix of α phase [35].

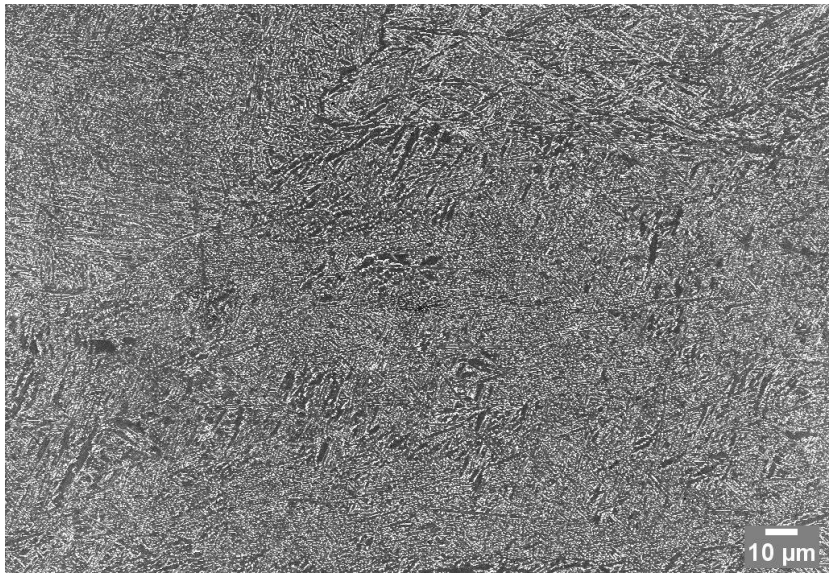

Figure 4.7: An overview of the microstructure at the top region of V13 implant (V13-TS).

A large needle shaped structure is evidently observed in the top section micrograph of implant made of Ti-6Al-4V virgin powder (Figure 4.8 (a)). There are also presence of minute fragmented pieces of these needle shaped structures in the microstructure. These needle like structures are martensitic features which are approximately 5 – 80 µm in dimension [27], [35]. The martensitic features appear to be in irregular orientation in the matrix with respect to other microstructural features. Nevertheless, the martensitic needles appears to satisfy the Burger orientation relationship which demands a perpendicular orientation of martensitic needles [27], [30], [34].

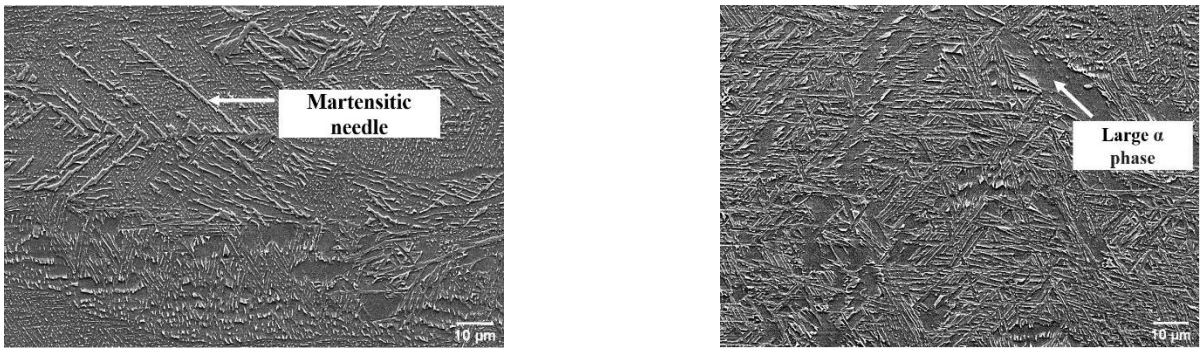

(a) (b)

Figure 4.8: SEM micrographs of V13-TS implant depicting (a) martensitic phase (b) large α phase

A most commonly observed feature in the microstructure is the large dark phase as indicated by the arrow in Figure 4.8 (b). There is no visual presence of white bright structures in this phase. It is assumed to be a large patch of α phase which can be in varying dimension and shape. The results from the compositional analysis should be evaluated in order to have a validation. This phase is further discussed in the trailing content.

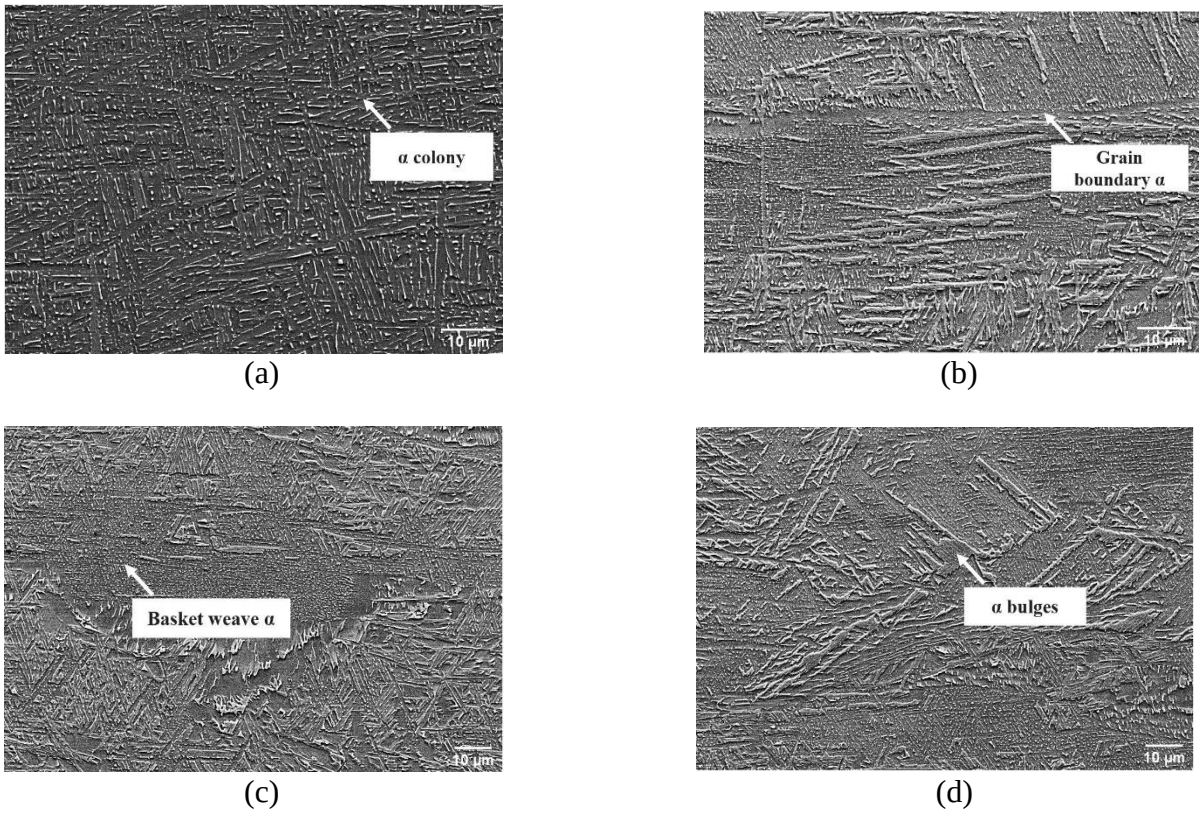

Figure 4.9: SEM micrographs of V13-TS implant depicting (a) colony of α phase (b) α and β features (c) basket weave α and (d) α bulges

Figure 4.9 portrays some of the typical features observed in an EBM processed Ti-6-4 alloy consisting of colony α, grain boundary α and basket weave α. These microstructural features might be originating due to several reasons which will be discussed in detail in the following content.

Along the prior β grain boundaries, a dark wavy patch which seperate β grains is observed. This microstructural feature is the grain boundary α [27]. In the OM micrographs, these features are observed (Figure 4.6) to be parallel to the building direction of implant. It is unlikely that they are formed during the initial cooling of the melt pool. Instead, the grain boundary α is nucleated in the trailing stages of build cooling at the large prior β grain boundaries. Moreover, a bulge like phase is frequently noted in the micrograph (Figure 4.9 (d)). These bulges are not typical in EBM microstructure and was misinterpreted to be an artifact occurring due to unsatisfactory etching. Nevertheless, these type of phases were mentioned by researchers in previous investigations [73].

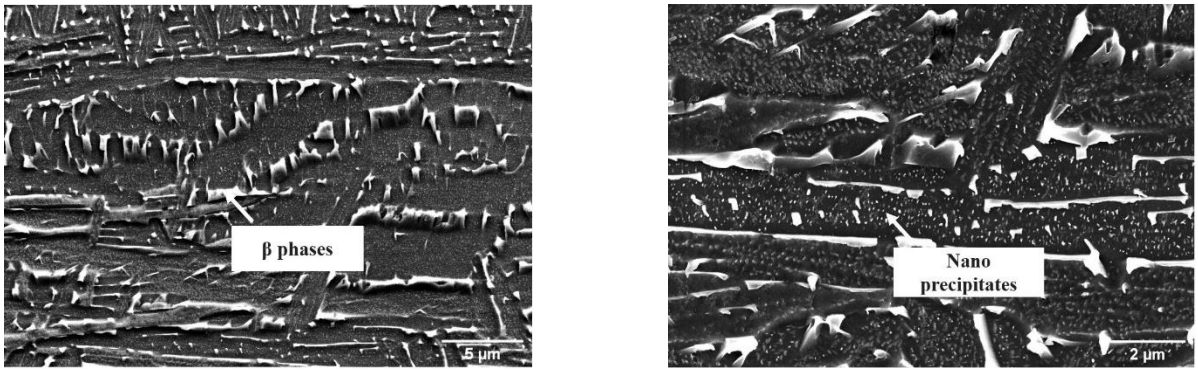

(a) (b)

Figure 4.10: SEM micrographs of V13-TS implant depicting (a) β phase (b) nano precipitates.

In Figure 4.10 (a), bright irregular features can be observed in the micrograph. They are irregular in morphology, orientation and size. These bright phases are β phases. Apart from these features, nano sized precipitates like structures are also observed in the α matrix (Figure 4.10 (b)).

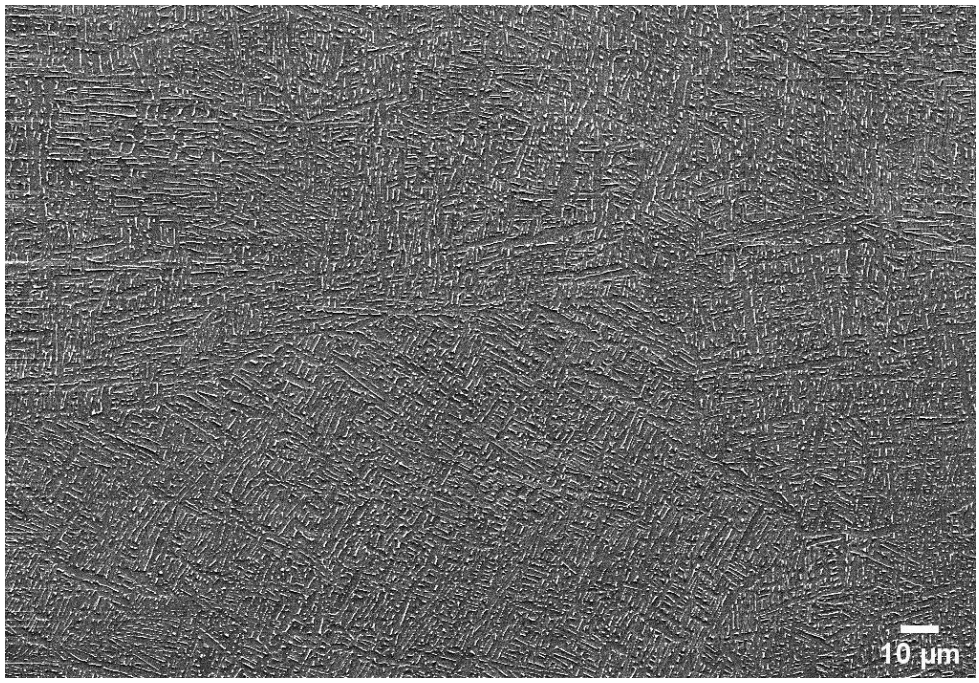

Figure 4.11: An overview of the microstructure at the bottom region of V13 implant (V13-BS).

The V13-BS microstructure (Figure 4.11) appears to be coarser than the V13-TS microstructure. The presence of bright, irregular shaped β features distributed in dark α matrix is evident in the V13-BS microstructure aswell. The microstructure is heterogeneous similar to the V13-TS microstructure. Nevertheless, the V13-TS microstructure appears to be finer and contain more fraction of martensitic phases.

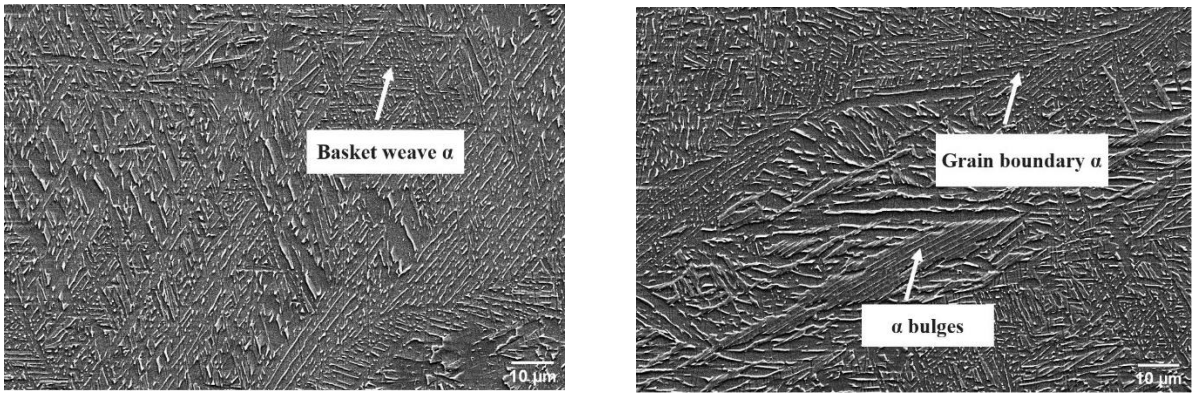

(a) (b)

Figure 4.12: Micrograph of V13-BS depicting (a)basket weave α (b) grain boundary α and α bulges .

The microstructure of V13-BS contains features similar to V13-TS sample. Figure 4.12 (a) depicts the basket wave α structure which is expected to be formed during the heat transfer stages.

Table 4.5. Compositional difference between phases in the V13-TS microstructure (wt-%)

Phase	Ti	Al	V	O	Si	Fe
Large α phase	88.19 ± 0.41	6.09 ± 0.06	3.16 ± 0.20	2.40 ± 0.37	0.03 ± 0.05	0.12 ± 0.15
α bulge phase	88.59 ± 0.46	6.04 ± 0.03	2.93 ± 0.23	2.31 ± 0.35	0.04 ± 0.01	0.08 ± 0.12
β phase	86.85 ± 3.16	5.69 ± 0.43	3.46 ± 1.22	3.71 ± 1.97	0.03 ± 0.02	0.28 ± 0.40

The fine microstructural features in V13-TS and V13-BS solid samples were a challenge during the EDS compositional analysis. The acceleration voltage chosen for generating K_α peaks from all elements is 10kV. This is the smallest acceleration voltage which have enough energy to generate the peaks from all the elements. However, the beam width might be larger than the microstructural features resulting in measurement errors. The surrounding surface region will also be analyzed along with the microstructural features.

Table 4.6. Compositional difference between phases in the V13-BS microstructure (wt-%).

Phase	Ti	Al	V	O	Si	Fe
Large α phase	88.88 ± 1.07	5.55 ± 0.56	3.39 ± 1.43	2.08 ± 0.31	0.03 ± 0.03	0.07 ± 0.09
α bulge phase	84.31 ± 2.91	4.66 ± 0.45	8.01 ± 2.95	2.17 ± 0.22	0.03 ± 0.04	0.83 ± 0.59
β phase	74.91 ± 8.10	2.89 ± 1.22	17.99 ± 8.33	1.50 ± 0.78	0.05 ± 0.02	2.66 ± 1.34

Table 4.5 and 4.6 list the elemental compositions of V13-TS and V13-BS microstructures, respectively. The compositional analysis is in accordance with the standard composition of Ti-6Al-4V as per the literatures [74]. The α phases are found to enriched with aluminum, while the β phase is vanadium enriched. Trivial variation in elements like Si and Fe can be observed between α and β phases. However, the variations are not significant enough to justify. The large phase observed in the microstructure of both samples is confirmed to be aluminum enriched. This ensures that the massive phase is α. A notable difference which is observed between the EDS analysis of V13-TS and V13-BS samples is the vanadium enrichment of α bulges in V13 BS sample. This variation will be discussed in detail in the trailing content.

4.2.1.2 Microstructure and elemental composition of solid region in 1x-13 implant.

Figure 4.13 portrays the overall view of the top region of 1x-13 implant. The micrograph has both bright and dark features, similar to the microstructure of V-13 implant. The microstructure appears to have phases which vary in size and morphology. This heterogeneous microstructure appears to be similar to the microstructure of V-13 implant. However, the microstructural features seem to be coarser than the V13-TS microstructure. The β phase is randomly distributed in the dark α matrix. The possible reasons for these heterogenous behaviour were discussed in the previous section (4.2.1.2).

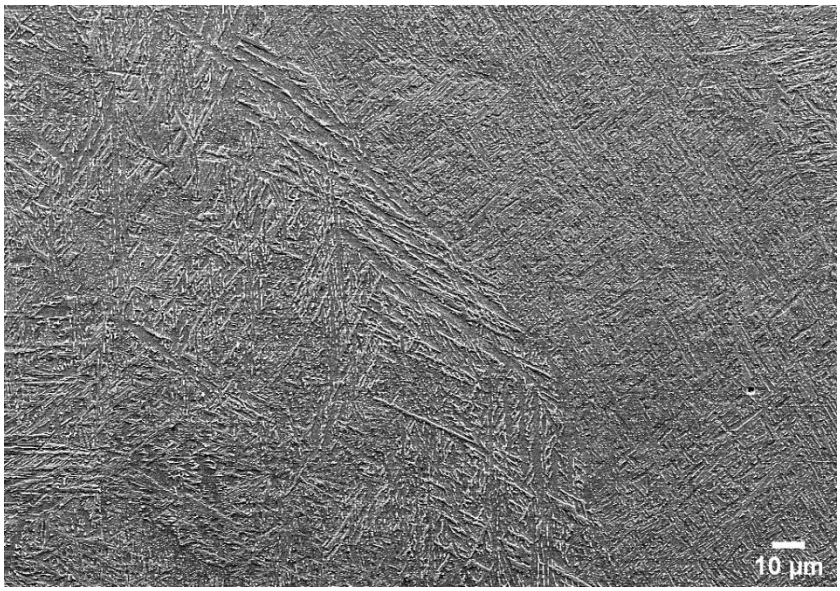

Figure 4.13: An overview of the microstructure at the top region of 1x-13 implant (1x13-TS).

In Figure 4.14 (a), the needle like phases can be observed similar to V-13 microstructure. These features were identified as martensitic phases as discussed in the previous content. They are approximately measured in the range of 5- 80 µm in length. The needle like structures occur in fragments which are dispersed randomly around the longer martensite needles. The presence of β phase is visually evident around the peripheries of these needles and fragmented structures. This presence of β phase around the needles, can be noted in the V-13 microstructure aswell. Similar to the V-13 microstructure, the needle like phase is observed to be obeying the Burger's orientation relationship. They are found to be in a perpendicular inclination between each other. The α bulges are found to be present in the 1x-13 sample, similar to the V13 sample. These bulge like structures possess lamellar like bright striations, which must be β phase. These structures are further discussed in section 4.2.1.3.

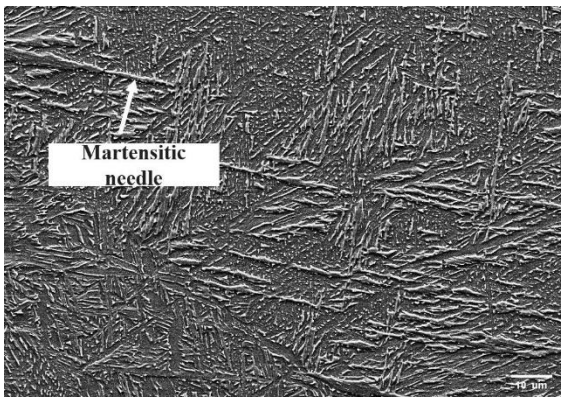

(a)

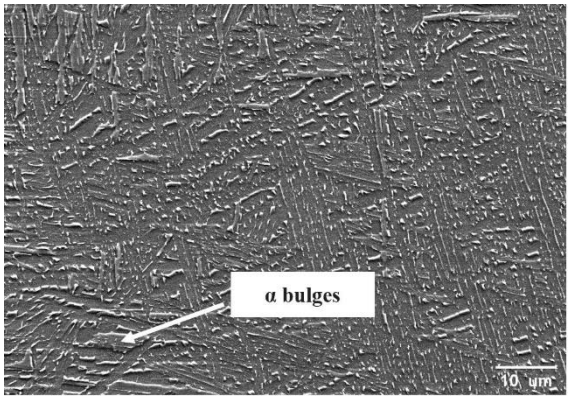

(b)

Figure 4.14: Micrograph of 1x-TS depicting (a)martensitic needles (b) α bulges .

Figure 4.15 portrays the basket weave and colony α microstructure. These kinds of microstructures are typical in EBM Ti-6Al-4V and were observed in V13 samples, aswell. The presence of large α phase in the top section of 1x – TS sample is less frequent compared to V13-TS sample. These large α phase are observed throughout the specimen microstructure at the top region. Grain boundary α is observed in the boundary region of prior β grains which is parallel to the direction of implant build. The irregularly shaped β phase is found to be unevenly distributed in the α matrix (Figure 4.16).

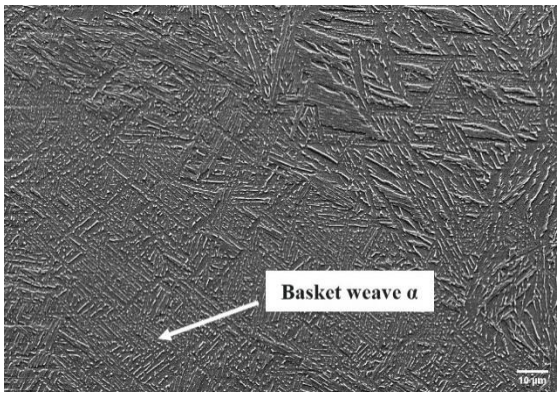

(a)

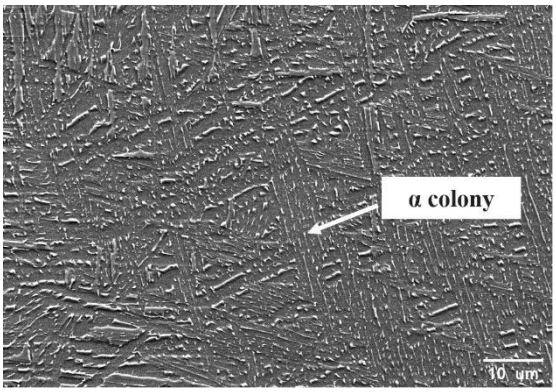

(b)

Figure 4.15: SEM micrographs of 1x-TS implant depicting (a) basket weave and colony α phase (b) α colony

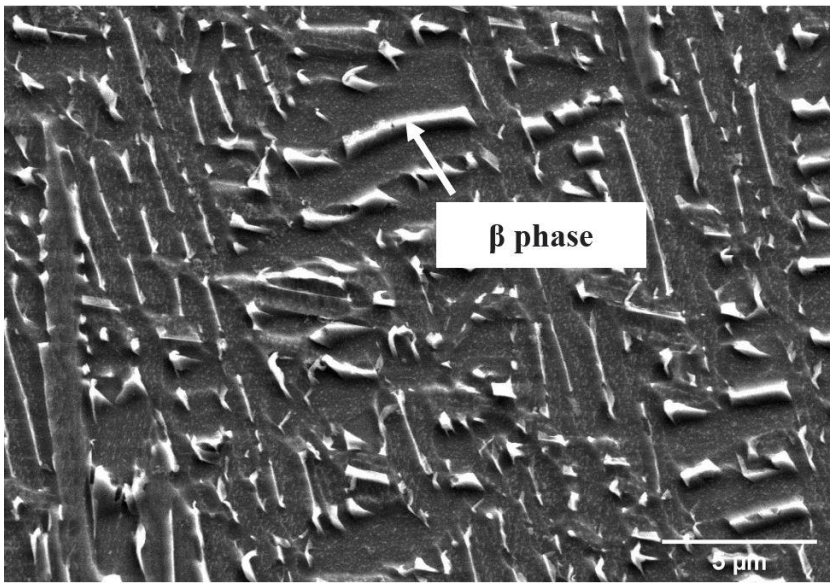

Figure 4.16: SEM micrographs of 1x-TS implant portraying α and β phase

Figure 4.17 shows the overall microstructural features at the bottom solid section of 1x-13 implant (1x13-BS). The micrograph appears to be heterogeneous and portrays both β and α phases in the microstructure. Nevertheless, the overall microstructure seems to be coarser than the microstructure at the top section of the solid sample. The amount of sharp martensitic needles appears to be reduced when compared to the micrograph at the top region of the solid section (Figure 4.13).

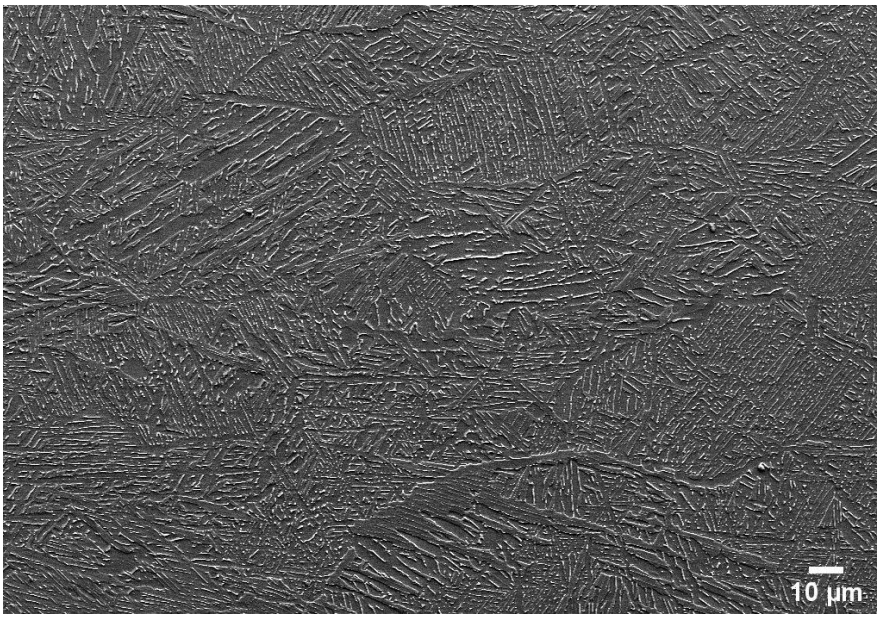

Figure 4.17: An overview of the microstructure at the bottom region of 1x-13 implant (1x13-BS).

The typical microstructural features like α colony, basketweave α and grain boundary α is visible in the 1x-BS microstructure aswell. The observed features do not show any variation from the V13 solid section microstructure (Figure 4.18).

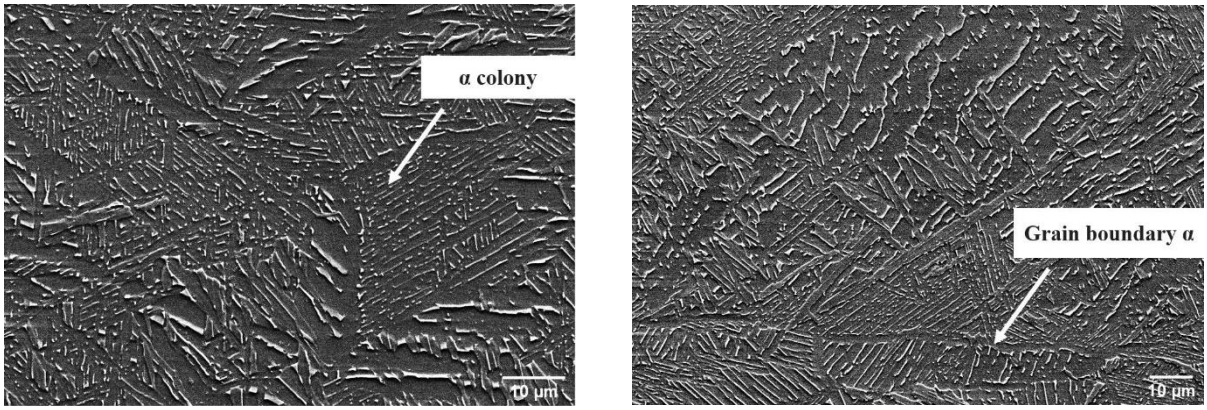

(a) (b)

Figure 4.18: SEM micrographs of 1x-BS implant depicting (a) colony α phase (b) grain boundary α.

The large α phase structure is observed more frequently in the bottom section microstructure of 1x-BS compared to 1x-TS sample (Figure 4.19). These phases were mentioned by researchers during previous investigations [75]. Nevertheless, the microstructural feature was not discussed in detail. There are numerous assumptions for the development of these phases in the Ti-6Al-4V microstructure. The large phase was misinterpreted as an oxide inclusion which might be formed during the EBM process [27]. The phase could be possibly an α-globular phase which can be formed during the lowered cooling rates of the EBM process. The feedstock morphology, composition and size can also be the reason for the formation of this phase which is not typical to EBM manufactured Ti-6Al-4V. EDS analysis on the phase validated that the large feature is α. The vanadium impoverishment of the feedstock can lead to improved α stability, leading to the formation of this phase [27], [28].

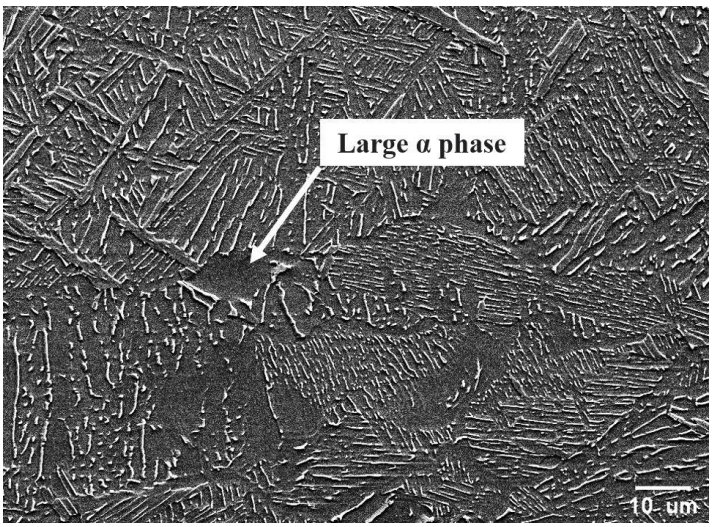

Figure 4.19: SEM micrographs of 1x-BS implant portraying a large α phase

The compositional analysis (EDS) of the surface confirmed again that the α and β phases are in accordance with the literature. The β phases are found to be enriched with vanadium and the α phases are found to be aluminium enriched.

Table 4.7. Compositional difference between phases in the 1x-TS microstructure (wt-%).

Phase	Ti	Al	V	O	Si	Fe
Large α phase	86.99 ± 1.71	5.69 ± 0.46	4.65 ± 2.12	2.26 ± 0.27	0.04 ± 0.05	0.38 ± 0.35
α bulge phase	87.29 ± 0.73	5.89 ± 0.21	4.38 ± 0.96	2.04 ± 0.30	0.07 ± 0.02	0.33 ± 0.22
β phase	80.47 ± 2.21	4.99 ± 0.52	9.14 ± 2.48	4.03 ± 1.06	0.10 ± 0.14	1.27 ± 0.42

Table 4.7 and 4.8 lists the composition of α and β phases in the microstructure of 1x-TS and 1x-BS respectively. Elements like Si, Fe and O show slight variations between α and β phases. The large phase is observed to be aluminium enriched, thus confirming it to be α phase. The vanadium enrichment in α bulge phase is observed from 1x -TS to 1x-BS sample. From the SEM micrographs, it is evident that the α bulges in the bottom section of the sample has more frequent β phase striations, comparatively. This can be attributed to the vanadium enrichment of α bulges in the bottom section of the sample.

Table 4.8. Compositional difference between phases in the 1x-BS microstructure (wt-%).

Phase	Ti	Al	V	O	Si	Fe
Large α phase	88.23 ± 0.82	6.08 ± 0.18	2.69 ± 0.51	2.80 ± 0.54	0.05 ± 0.03	0.15 ± 0.10
α bulge phase	86.74 ± 1.94	5.83 ± 0.40	4.20 ± 1.44	3.02 ± 1.04	0.02 ± 0.02	0.18 ± 0.15
β phase	82.13± 7.08	4.70 ± 1.52	9.50 ± 7.59	2.18 ± 0.60	0.03 ± 0.03	1.46 ± 1.51

4.2.1.3 Microstructure and elemental composition of solid region in 5x-13 implant.

Figure 4.20 shows the overview of the top section microstructure of 5x – 13 implant (5x13-TS). The micrograph clearly portrays both α and β phases in the microstructure which can be identified from their contrast difference. The bright β phases are found to be distributed in the α matrix.

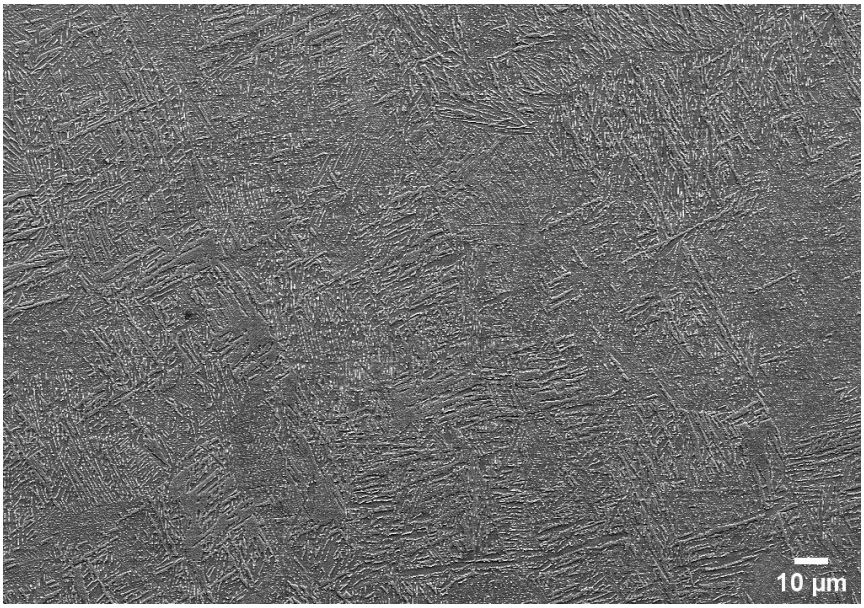

Figure 4.20: An overview of the microstructure at the top region of 5x-13 implant (5x13-TS).

The presence of sharp martensitic needles and alpha bulges similar to V13-TS and 1x-TS (Figure 4.21),is also found in the microstructure of 5x13 - TS.

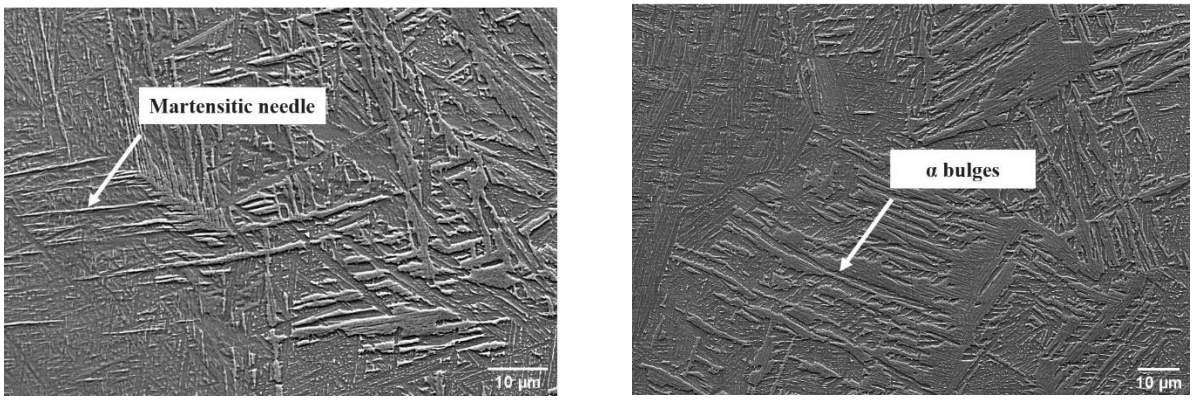

(a) (b)

Figure 4.21: Micrograph of 5x-TS depicting (a)martensitic needles (b) α bulges .

Short fragments of needles are found in the peripheries of larger acicular martensite. These short martensitic needles are observed to obey the Burger's orientation relationship like the acicular martensite. The fragments are assumed to be retained martensitic structures, which

remains after partial decompositon of acicular martensitic structures. The presence of bright β phases can also be noted in the micrographs (Figure 4.21).

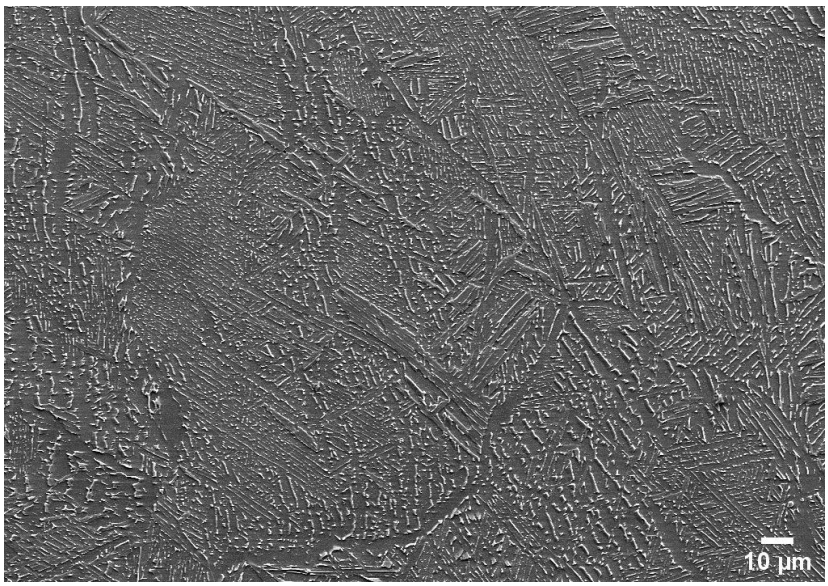

Figure 4.22: An overview of the microstructure at the top region of 5x-13 implant (5x13-BS).

Figure 4.22 portrays the overview of the bottom section microstructure of 5x-13 implant. It can be clearly noted that microstructure is heterogeneous and contain both α and β phases. Similar to V-13 and 1x-13 implants, the microstructure at the bottom section of the implant is found to be coarser than the top section. The fraction of martensitic structures is found to be low compared to the 5x13-TS implant.

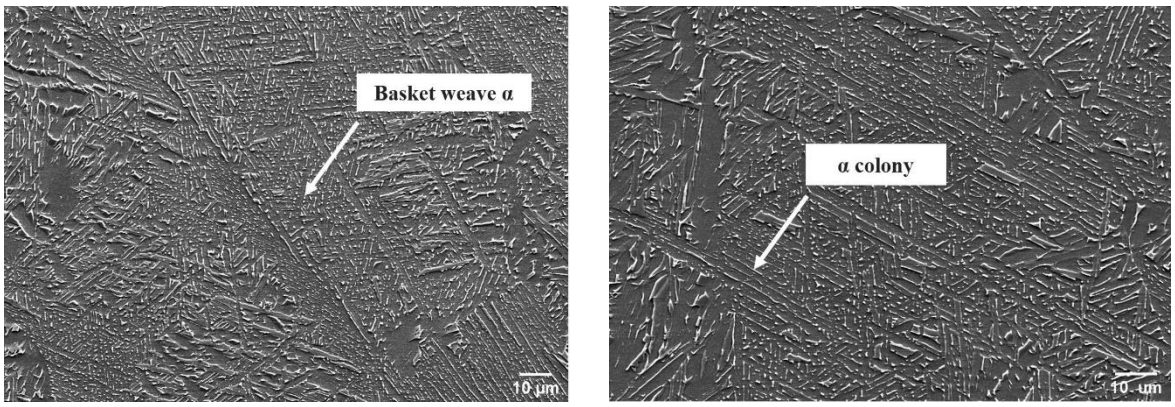

(a) (b)

Figure 4.23: Micrograph of 5x-BS depicting (a)basketweave α (b) α colony .

Typical EBM microstructural features in Ti-6Al-4V like, basketweave α and α colony is evident in the microstructure of 5x13-BS implant (Figure 4.23). Grain boundary α is found to be present along the prior β grain boundary, similar to previous samples analyzed. The large α phase is found to be more frequent in the 5x13-BS microstructure, compared to 5x13-TS microstructure. The bulge like microstructural features called α bulges is also observed in the micrograph. Nevertheless, the compositional analysis confirmed that the phase is α.

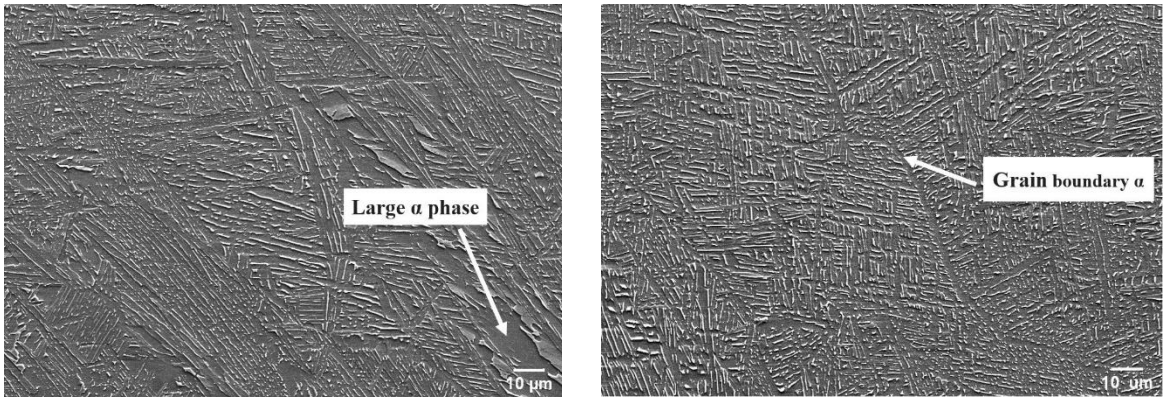

(a) (b)

Figure 4.24: Micrograph of 5x-BS depicting (a)large α phase (b) grain boundary α .

The EDS analysis of the samples confirmed that the composition of the developed 5x13 Ti-6Al-4V implants is in accordance with the literature (Table 4.9 and 4.10).

Table 4.9. Compositional difference between phases in the 5x-TS microstructure (wt-%).

Phase	Ti	Al	V	O	Si	Fe
Large α phase	86.96 ± 1.50	5.81 ± 0.30	4.88 ± 1.55	2.19 ± 0.17	0.02 ± 0.02	0.14 ± 0.29
α bulge phase	87.67 ± 2.57	6.06 ± 0.51	3.88 ± 2.81	1.99 ± 0.20	0.05 ± 0.02	0.35 ± 0.36
β phase	76.80 ± 3.59	4.13 ± 0.85	14.64 ± 4.34	2.81 ± 0.89	0.05 ± 0.02	1.57 ± 0.58

The compositional analysis clearly portrays the aluminium enrichment of α phase and vanadium enrichment of β phase (Table 4.9 and 4.10). Similar to the V13 and 1x13 TS samples, an increase of both O and Fe content in β phase compared to α phase, is notable in the 5x13 TS sample aswell. This is due to the β stabilizing behaviour of Fe and O [27]. Nevertheless, a different trend is observed in the β phases of V13, 1x13 and 5x13 BS samples, where the O content is found to be decreasing and Fe content is increasing compared to α phase. The TS samples have a finer microstructure compared to BS samples due to which the EDX analysis might include information from the surrounding region of the analysed phases. This can be the reason for increase in O content in β phase of TS samples, eventhough O is an α stabilizer.

Table 4.10. Compositional difference between phases in the 5x-BS microstructure (wt-%).

Phase	Ti	Al	V	O	Si	Fe
Large α phase	86.71 ± 5.39	5.89 ± 1.04	4.85 ± 5.63	1.94 ± 0.27	0.06 ± 0.02	0.55 ± 1.01
α bulge phase	86.44 ± 2.14	5.49 ± 0.63	5.34 ± 2.44	2.27 ± 0.22	0.05 ± 0.03	0.41 ± 0.43
β phase	72.51± 5.50	2.74 ± 1.22	19.76 ± 6.11	1.76 ± 1.11	0.11 ± 0.07	3.12 ± 0.98

The percentage of O is found to be higher compared to the nominal values. This variation is possibly due to the difficulty of EDS to evaluate the precise concentration of light elements like O. Also, a possible formation of oxide layer on the microstructural features can lead to an increase in O content aswell.

In summary, the solid regions in implant samples, clearly portrays a variation with respect to the build height in V13, 1x and 5x samples. It is noted that the microstructure tends to be coarser at the place, close to the build plate. A fine heterogeneous microstructure with more fraction of martensitic structures can be noted at the top region of build, in all the implants. It is evident that the presence of different microstructural features is independent of the build height. This is in accordance with literature [76]. The coarsening of microstructure can be attributed to the slower cooling rates near to the build plate. The elemental composition of different microstructural phases in the implants does not show any significant variation with powder recycling.

4.2.1.4 Microstructure and elemental composition of lattice regions in implant samples.

Figure 4.25 portrays the difference in microstructural features in lattice and solid samples. The lattice microstructure is observed to be heterogenous with more fraction of martensitic phases. The microstructure of the lattice cross section of all three implant samples (V13, 1x13 and 5x13) is depicted to have sharp needle like structures which are acicular martnesite. There is presence of short fragment of needles along with these martensite . The martensitic structures are observed to have a dimension within the range of 5 – 100 µm. There are bright β phases dispersed along the peripheries of these martensitic needles.

The microstructure of the solid cross section is found to be heterogeneous. Nevertheless, the microstructure is coarser compared to the lattice microstructure. This is due to the faster cooling rates in the lattice region compared to solid region. The lattice region has a smaller area compared to the solid region at the same location of build height. The solid and the lattice regions are found to have a typical EBM microstructure of Ti-6Al-4V alloy. Phases like α bulges, colony α and grain boundary α were present in the microstructure of solid region aswell. However, no signficant difference in microstructure was observed between V13, 1x13 and 5x13 implant samples.

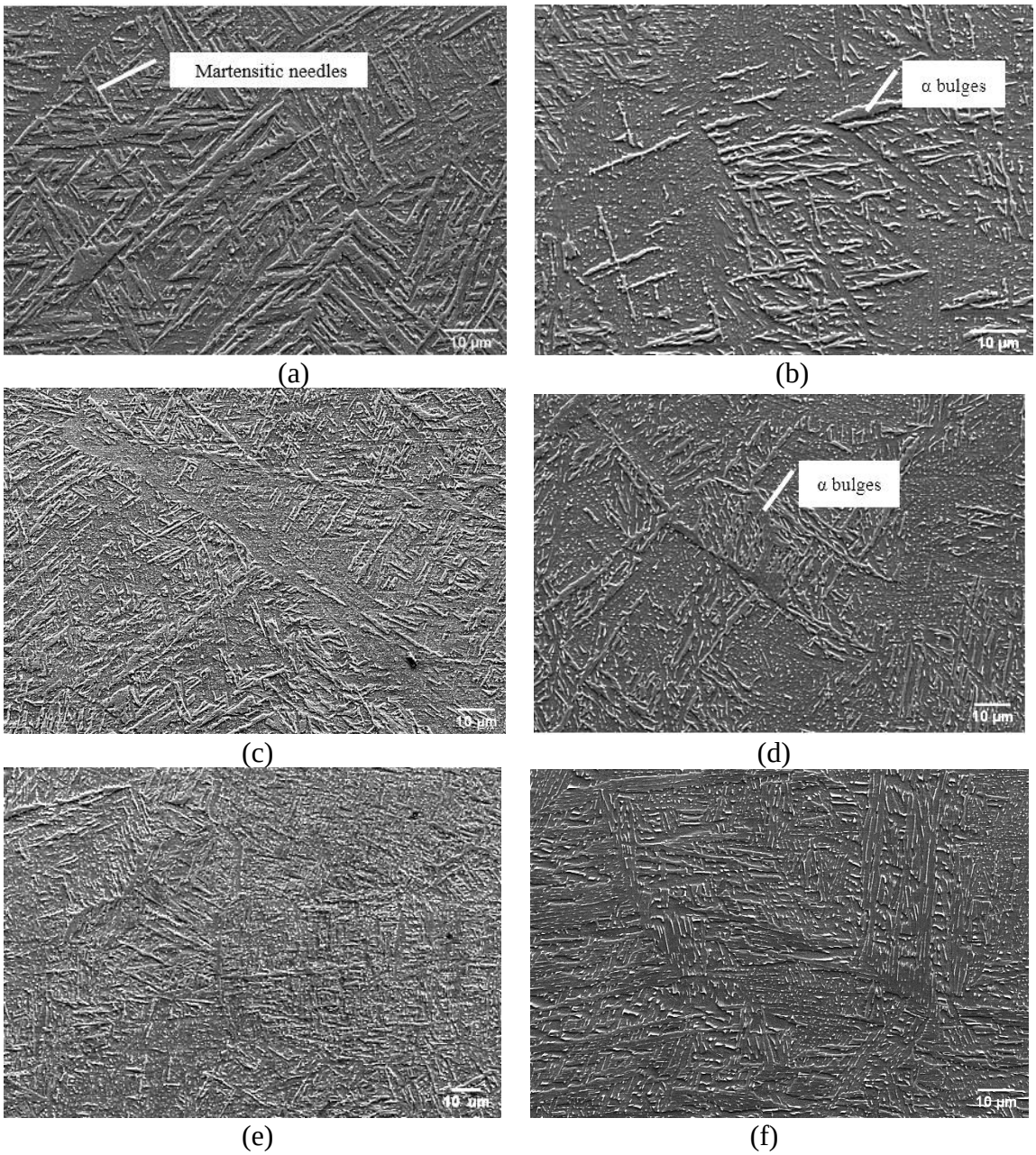

Figure 4.25: Micrograph of (a) V13 lattice cross section (b) V13 solid cross section (c) 1x13 lattice cross section (d) 1x13 solid cross section (e) 5x13 lattice cross section and (f) 5x13 solid cross section

The horizontal plane of the lattice region, which is perpendicular to the build direction, is found to possess more fraction of martensitic needles. A martensitic phases in the lattice region is found to obey the Burger's orientation relationship (Figure 4.26).

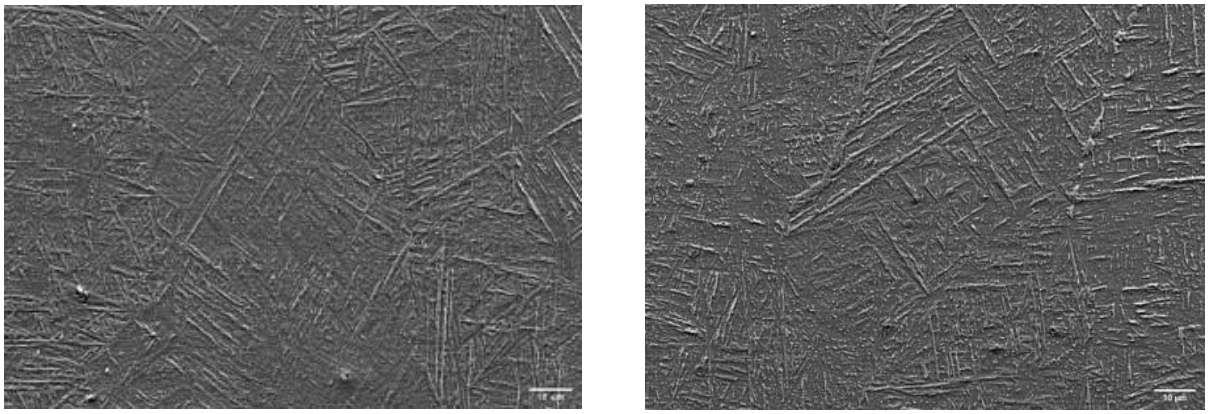

(a) (b)

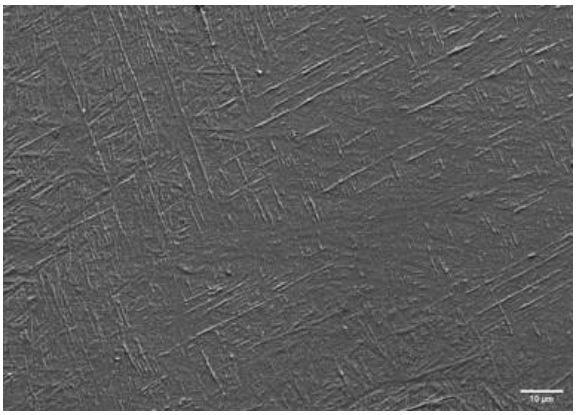

(c)

Figure 4.26: Micrograph of horizontal plane in lattice of (a)V13 implant (b) 1x 13 implant (c) 5x implant.

The EDS analysis of different phases in the lattice microstructure of V13, 1x13 and 5x13 implant shows that the α phase is aluminium enriched and the β phase is vanadium enriched (Table 4.11, 4.12 and 4.13). There were no significant variations in the elemental composition of phases in the lattice microstructure with powder recycling. However, the different α and β phases had phenomenal difference in composition as discussed in the previous sections.

Table 4.11 Compositional difference between phases in the lattice V13 microstructure (wt-%).

Phase	Ti	Al	V	O	Si	Fe
Large α phase	87.36 ± 2.48	5.81 ± 0.32	4.22 ± 2.35	2.19 ± 0.18	0.04 ± 0.02	0.39 ± 0.49
α bulge phase	87.13 ± 1.69	5.77 ± 0.29	4.36 ± 2.11	2.32 ± 0.43	0.02 ± 0.02	0.41 ± 0.30
β phase	85.94 ± 3.03	5.43 ± 0.58	5.36 ± 2.84	2.55 ± 0.50	0.03 ± 0.02	0.69 ± 0.93

Table 4.12Compositional difference between phases in the lattice 1x13 microstructure (wt-%)

Phase	Ti	Al	V	O	Si	Fe
Large α phase	87.34 ± 3.04	5.77 ± 0.43	4.47 ± 2.84	1.96 ± 0.44	0.04 ± 0.01	0.42 ± 0.90
α bulge phase	88.56 ± 0.37	5.93 ± 0.18	3.11 ± 0.59	2.23 ± 0.12	0.03 ± 0.03	0.14 ± 0.10
β phase	77.08 ± 7.03	4.53 ± 1.01	12.40 ± 5.63	3.41 ± 0.84	0.06 ± 0.05	2.53 ± 1.74

Table 4.13Compositional difference between phases in the lattice 5x13 microstructure (wt-%)

Phase	Ti	Al	V	O	Si	Fe
Large α phase	88.19 ± 0.42	6.31 ± 0.10	2.80 ± 0.22	2.48 ± 0.37	0.07 ± 0.04	0.14 ± 0.11
α bulge phase	88.35 ± 0.59	6.16 ± 0.07	2.86 ± 0.18	2.34 ± 0.36	0.09 ± 0.10	0.20 ± 0.27
β phase	87.83 ± 1.89	5.81 ± 0.63	4.49 ± 2.39	1.65 ± 0.18	0.05 ± 0.03	0.17 ± 0.18

4.2.1.5 Nano Particles.

Nanosized particulate structures were observed in the α matrix at higher magnifications (Figure 4.27). The precipitates were randomly distributed in the α phase and were measured to be in the range of 30– 100 nm. The particulates have varying morphology and size compared to each other. In previous investigations, researchers have made several assumptions regarding the particulate phase. In the earlier stages, the nano particles were assumed to be Ti3Al precipitates. This was in accordance with typical dimension range of Ti_3Al precipitates (50 – 200 nm) [73]. The particulates were expected to be developed during the exposure to higher chamber temperatures where the α phase was formed. The particles were also observed to be formed during controlled heat treatment process [77]. However, the particulates cannot be confirmed to be Ti_3Al precipitates, in this study. The dimension of the particles made it difficult to be analyzed using the standard composition analysis techniques like EDS. However, an SE-BSE image comparison was carried out inorder to validate the presence of α Ti_3Al precipitates.

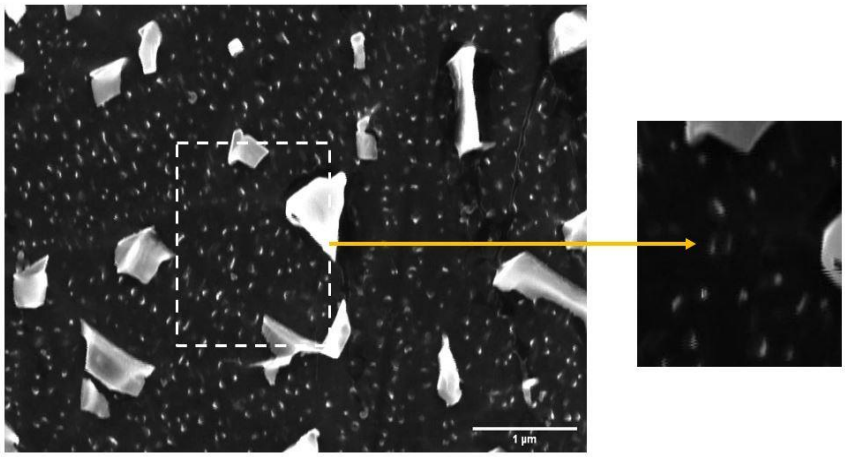

Figure 4.27: Micrograph of V13 BS solid sample portraying the nano sized particles in α matrix.

The particles were imaged using both SE and BSE detectors in a FEG-SEM (Figure 4.28). The BSE images will provide a chemical contrast which aids in pointing out various phases. The particles which were identified in the SE images of the implant samples appeared to be bright white particulates in the BSE images. This suggests that the particulates are vanadium enriched *nanosized β particles* which were observed in all three implant samples made from virgin, 1 time and 5 times recycled powder (Figure 4.28).

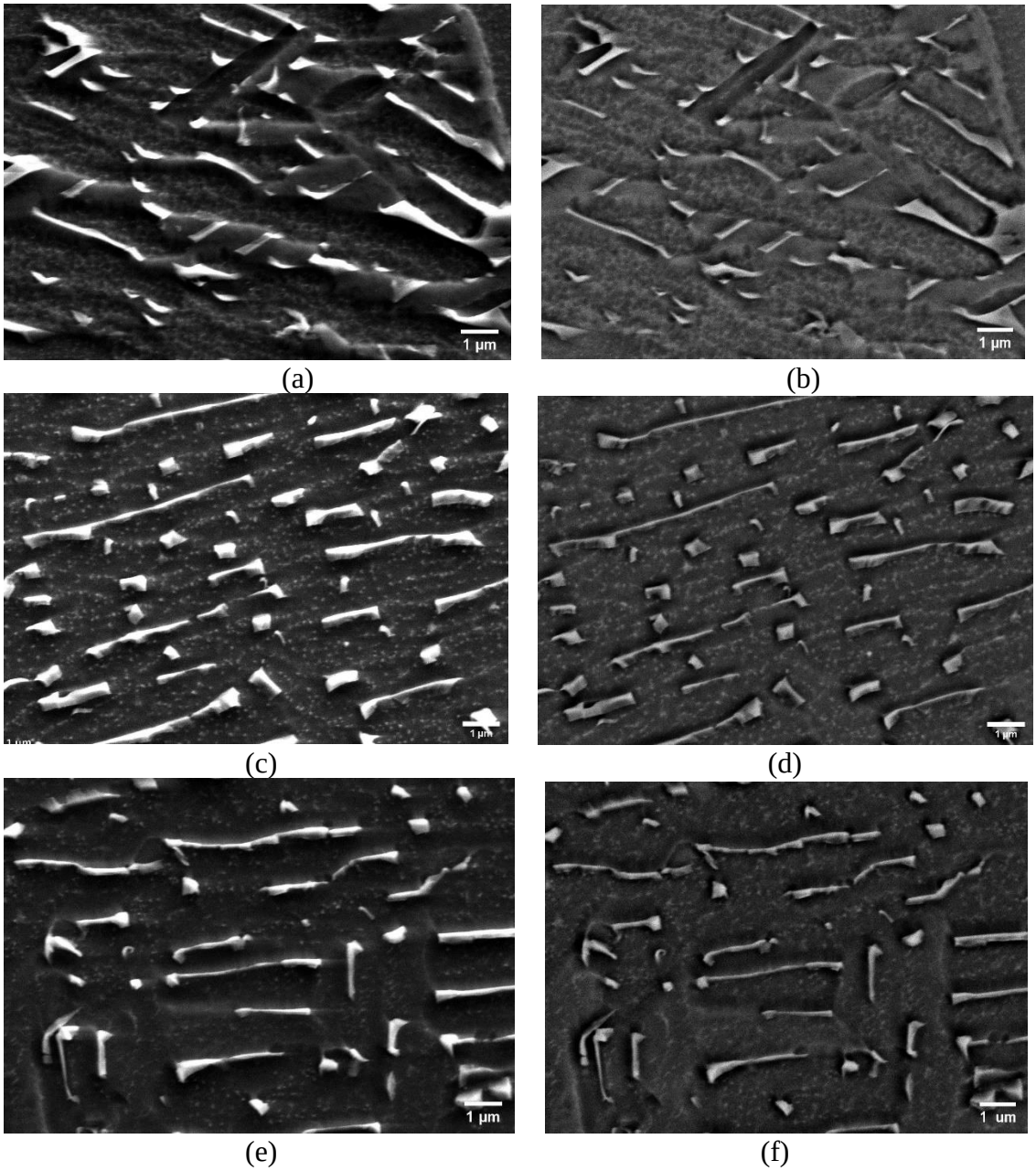

Figure 4.28: Micrographs portraying (a) V13 SE image (b) V13 BSE image(c)1x SE image (d) 1x BSE image (e) 5x SE image and (f) 5x BSE image.

4.2.1.6 Average α- lath thickness

The α- lath thickness is an important factor which aids in improving the mechanical properties of the developed Ti-6Al-4V alloy [76]. Figure 4.29 shows the variation in average α- lath thickness of the solid regions in V13, 1x13 and 5x13 implant microstructures. The average alpha lath thickness of all the implants is found to be in the range of 0.6 – 0.7 µm. The largest α- lath thickness was observed for the implant samples fabricated from virgin powder. Nevertheless, the variation was not significant enough to be justified. The implant samples made from 1 times and 5 times recycled powders did not exhibit any variation in α- lath thickness. In summary, no phenomenal variations can be observed in the average α- lath thickness of implant samples, with powder recycling.

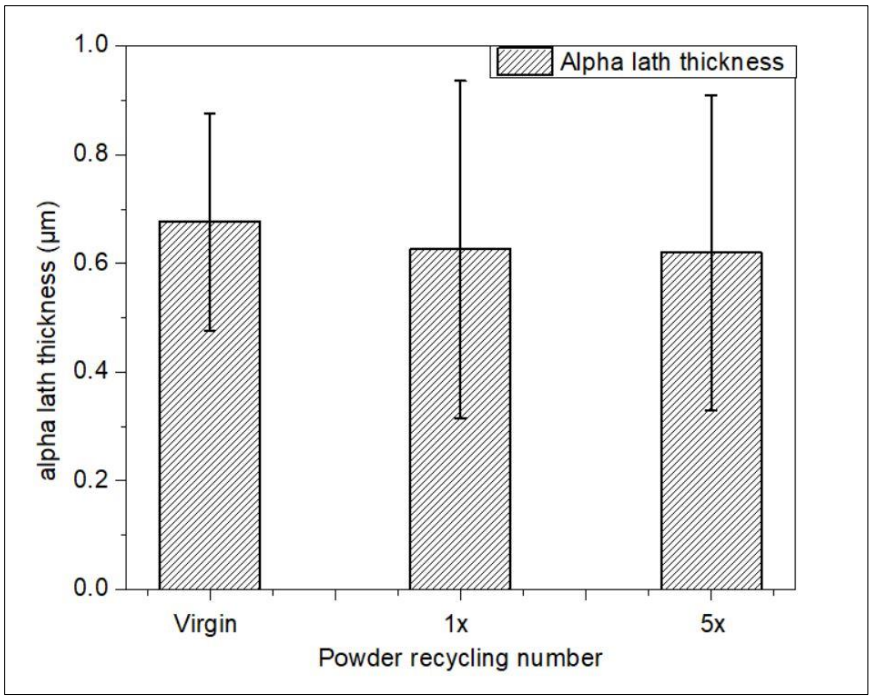

Figure 4.29: Plot depicting the variation in α- lath thickness in implant samples with respect to powder recycling.

4.2.2 Porosity analysis

Typical EBM porosities were observed in the V13, 1x13 and 5x13 samples. The porosities like lack of fusion and gas porosities with size upto 100 µm were observed on both solid and lattice regions of the implant samples. Figure 4.30 portrays the various types of porosities in the implant samples. Figure 4.30 (a) and (c) exhibits the gas porosities which are 10 – 80 µm in dimension. These porosities, which are larger in dimension is formed during the EBM manufacturing process [36]. The porosities which are smaller than 2 µm in dimension are formed as a result of feedstock anomalies. The lack of fusions observed in the samples were formed during the EBM process (Figure 4.30 (b) and (d)) [36], [37]. They were approximately measured to be 40 – 120 µm in dimension. The porosity values can affect the mechanical properties of the developed samples [37].

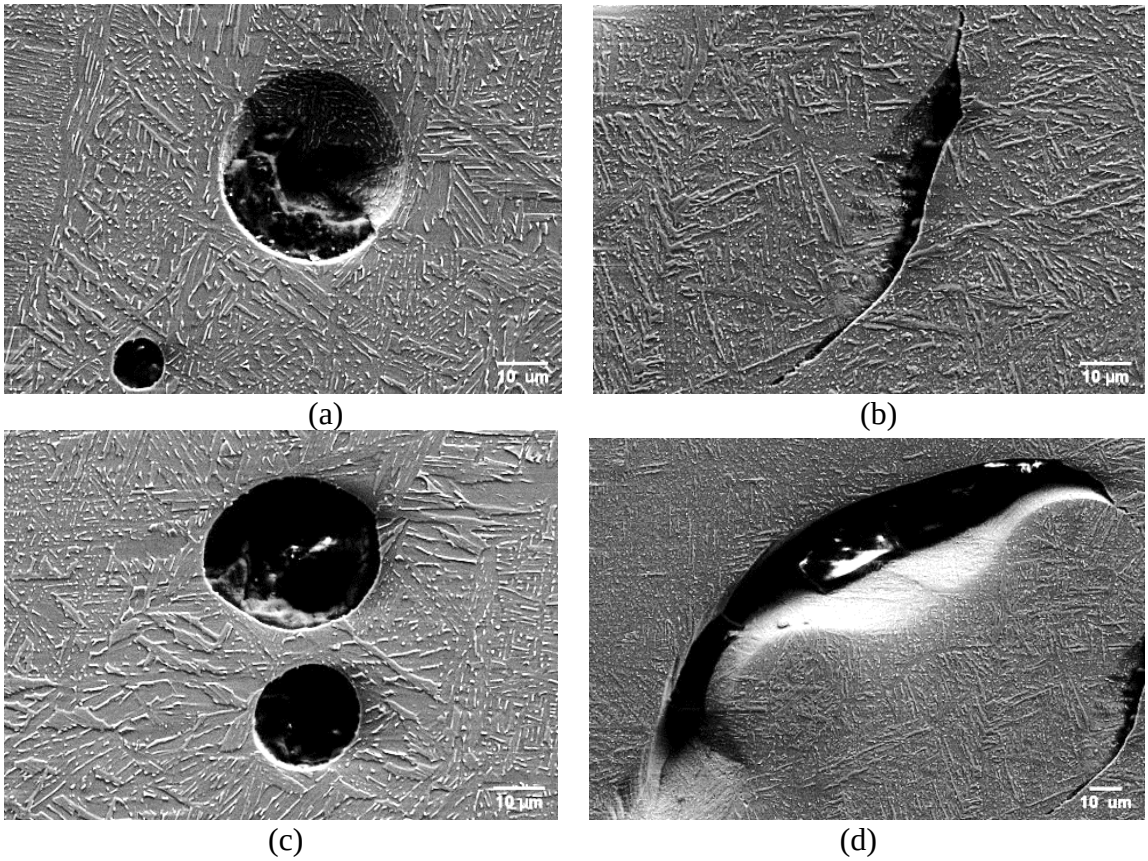

(a) (b)

(c) (d)

Figure 4.30: FEG-SEM Micrograph portraying (a) gas porosity in V13 solid sample (b) lack of fusion in 1x lattice sample (c) gas porosity in 5x solid sample (d) lack of fusion in 5x lattice sample

4.2.2.1 Porosity percentage

Figure 4.31 portrays the variation of porosity percentage values in V13, 1x13 and 5x13 samples with respect to build height. In general, the porosity percentage is found to be increasing with the distance from the build plate. From bottom to top, the increase in porosity percentage is ~ 0.05 %, 0.18 % and 0.17 % for V13, 1x13 and 5x13 implant respectively. This is in accordance with the literature [36]. This percentage increase in porosity with respect to build height can be attributed to the varying scanning strategy and thermal complexity at a larger distance from the build plate [36].

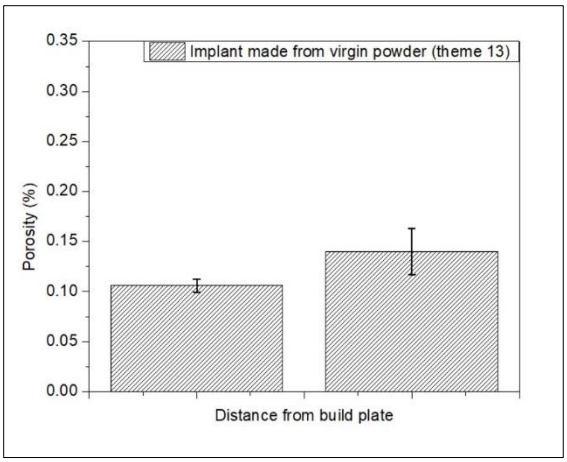

(a)

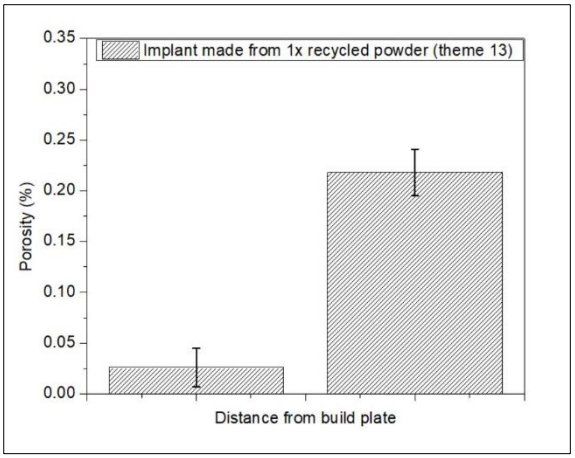

(b)

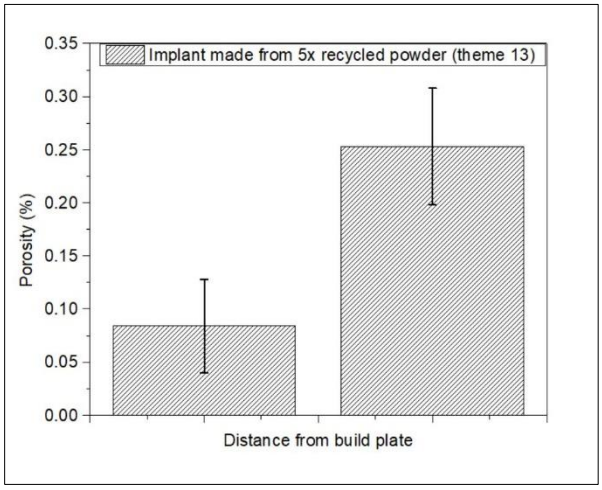

(c)

Figure 4.31: Plot depicting the variation in porosity percentage with respect to build height in (a) V13 implant (b) 1x implant (c) 5x implant.

The percentage variation in porosity with respect to powder recyling is portrayed in Figure 4.32. It can be observed that for samples far from the build plate, the porosity percentage increases with increasing recyling of powder samples. Near to the build plate, however, the implant samples exhibit a decrease in porosity percentage after1 time recyling of powder while similar porosity as V13 was found for samples fabricated with 5 times recycled powder. This can be due to the feedstock and process anomalies.

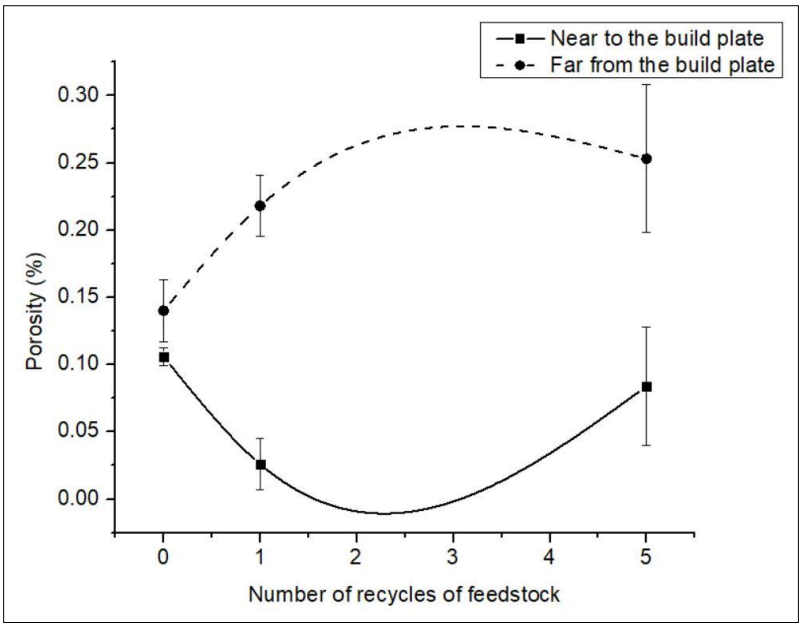

Figure 4.32: Plot depicting the variation in porosity percentage with respect to powder recycling.

4.2.3 Implant surface chemistry

The surface chemistry of implants is an important factor which decides the bio-chemical reactions and tissue regeneration properties of the developed implant. The presence of oxides and other elements is crucial for bone – implant interaction to a certain level [78]. The surface elemental composition, chemical state of elements and their depth profiles are detailed in this section

4.2.3.1 Survey spectrum

The survey spectrum details the elemental composition on the surface of the implant samples. The lattice and solid regions on the implant samples were analyzed in order to know the elements existed there. Figure 4.35 shows the survey spectra of lattice and solid samples of V13, 1x13 and 5x13 samples. It is evident from the survey spectrum plots that all the samples constitute of Ti, V, Al, O and N. The intensity of vanadium peaks is observed to be feble, compared to the peaks of titanium, oxygen and carbon. A low intensity peak of iron ($Fe2p_{3/2}$) was observed in the V13 lattice sample (Figure 4.33 (a)). But, the intensity of iron peak is difficult to be defined in the survey spectrum of other samples.

The carbon peak (C1s) is observed to have a relatively high intensity. The presence of carbon on the sample surface is due to the contamination which can occur during sample handling and processing [55]. The presence of calcium is evident in all the samples, owing to the development of calcium contamination on the sample surface. In the initial stages, calcium was misinterpreted to be an element present in the composition of the alloy. But, the immediate elimination of calcium after sputtering with Ar^+ ions, confirm that it is a contaminant on the implant surface. The intensity of aluminium peak is low compared to other elements present in

the implant samples. However, the presence can be confirmed as it is located between the range of 70 – 80 eV.

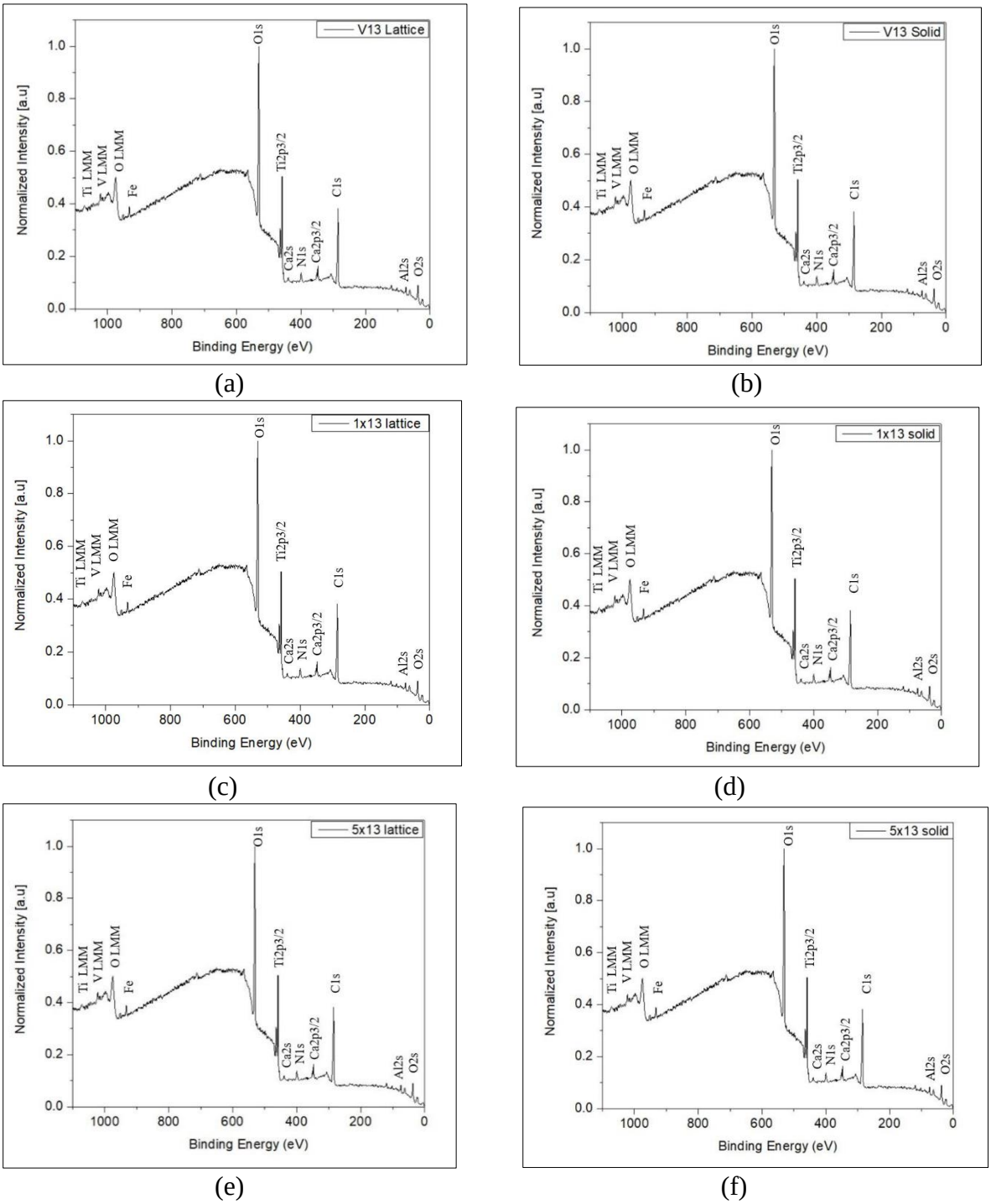

Figure 4.33: Survey spectrum of (a) V13 lattice (b) V13 solid (c) 1x13 lattice (d) 1x13 solid (e) 5x13 lattice (f) 5x13 solid

4.2.3.2 Chemical state

The oxidation states of the elements of interest were determined by analyzing the multiplex spectrum of the respective elements. Nitrogen, titanium, vanadium and aluminium were analyzed inorder to identify their chemical state in lattice and solid surfaces. The analysis was conducted on surfaces that were not sputtered. Sputtering is a destructive process and this might change the chemical state of the surface [55], [57]. From Figure 4.34 (a), no clear variation in chemical states of titanium in the lattice sample was observed. Titanium is found to be existing in the Ti^{4+} (TiO2) state, most commonly [59]. The Ti^{4+} (Ti $2p_{3/2}$) is located at the binding energy position of 458.7, approximately.

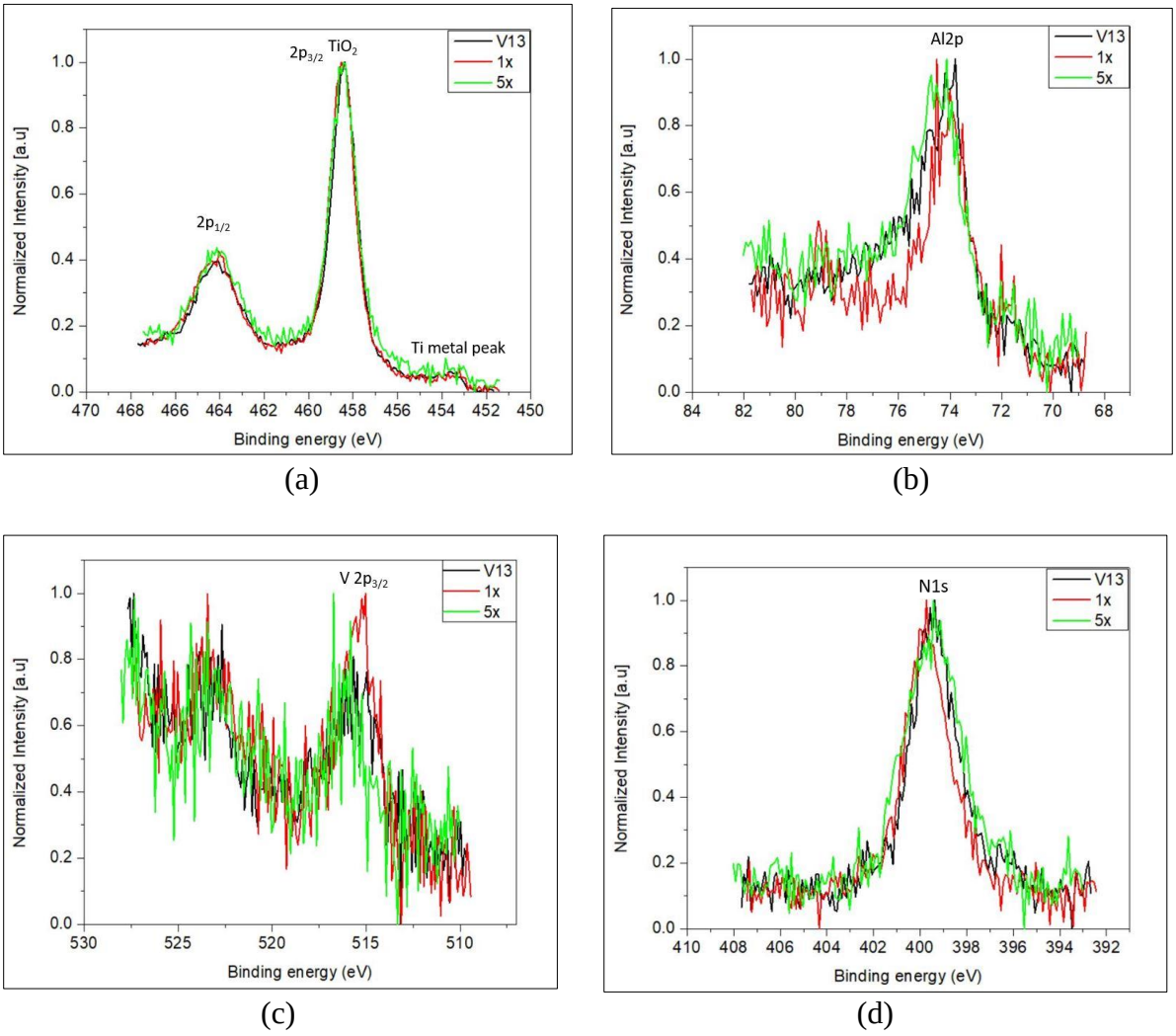

Figure 4.34: High resolution spectrum of (a) Lattice Ti 2p3/2 (b) Lattice Al 2p (c) Lattice V 2p3/2 (d) Lattice N1s

The aluminium peak (Al2p) is located at a binding energy of 74.2 eV approximately (Figure 4.34). Aluminum is noted to be existing at an oxidation state of $Al3^{+}$, which is Al_2O_3 [79]. Hydroxide may develop in some cases, as indicated by the positive peak shift of Al 2p for lattice 5x13 sample (Figure 4.34 b). Vanadium exists as V_2O_5 (V^{5+}) with $V2p_{3/2}$, at a binding energy position of approximately 516 eV [80]. However, no significant peak shift is observed

between V13, 1x13 and 5x13 samples. The highest intensity peak of nitrogen is N1s, which is located approximately at 399 eV. According to the literature, nitrogen is expected to exist as TiN [81].

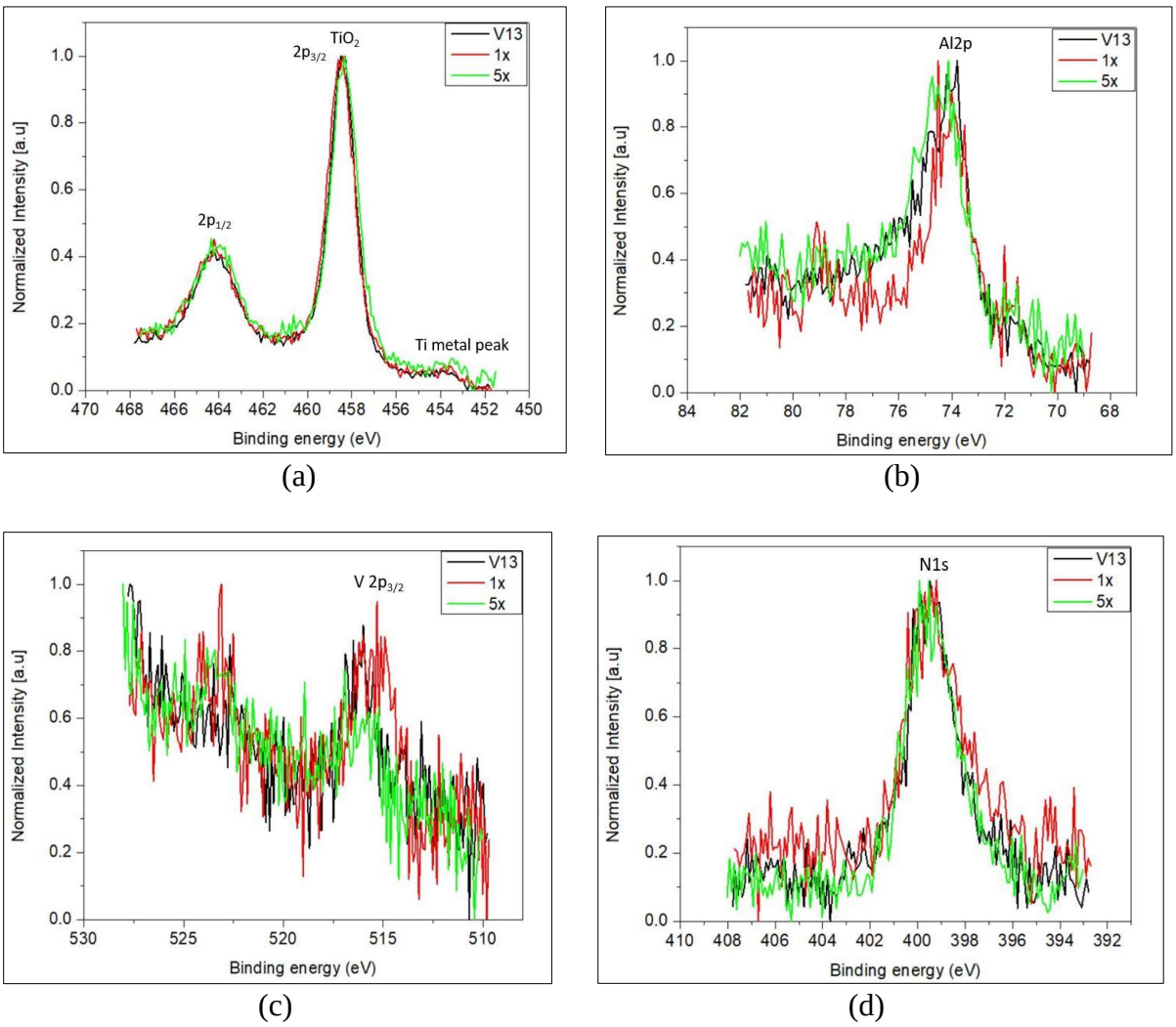

Figure 4.35: High resolution spectrum of (a) Solid Ti 2p3/2 (b) Solid Al 2p (c) Solid V 2p3/2 (d) Solid N1s

Figure 4.35 portrays the high resolution spectra of solid V13, 1x13 and 5x13 samples. It is evident from the plots that the oxidations states of elements are similar to the oxidation states in lattice samples. The lattice and solid samples do not exhibit any other phenomenal variations. A trivial variation is observed in the peak locations of Ti, Al, V and N, compared to the provided binding energy values from the XPS handbook [82]. This trivial variations are the effect of XPS instrument calibration [80]

4.2.3.3 Depth Profile

Figure 4.36 portrays the depth profiles of lattice and solid sections of the implant samples. The atomic concentration of O, N, C, Ti, Al and V as a function of sputter time or depth can be identifed from the profiles. The concentration of titanium is found to be drastically increasing with sputtering. For example, the titanium concentration is found to be increasing upto 75 at % approximately, for V13 lattice and solid samples (Figure 4.36 (a) and (b)). The concentration of carbon is significantly decreasing with depth in all the samples. This observation concludes that carbon is a surface contaminant which is removed with Ar^+ ion sputtering [55]. The aluminium concentration is found to be increasing with sputtering. However, vanadium is trivial at the surface layer and is found to be increasing significantly with etch time.

In the V13 lattice and solid samples, the oxygen concentration is found to be notably decreasing by a sputering time of 10 minutes. However, the concentration of oxygen is found to show a notable decrease only after 20 minutes of sputering time in 1x13 and 5x13 samples, indicating the increase of oxide thickness. This explains the decrease in titanium concentration, towards the interior region of samples. The higher concentration of oxygen indicates the presence of oxide compounds like titanium oxide, aluminium oxide and vanadium oxide towards the interior region of the implant samples [59]. The higher oxygen content in 1x13 and 5x13 samples might be arising as a result of recycled powder being used for the implant fabrication. The higher oxygen content in the recycled feedstock will result in a notable increase in oxygen concentration of fabricated implant samples [67], [69].

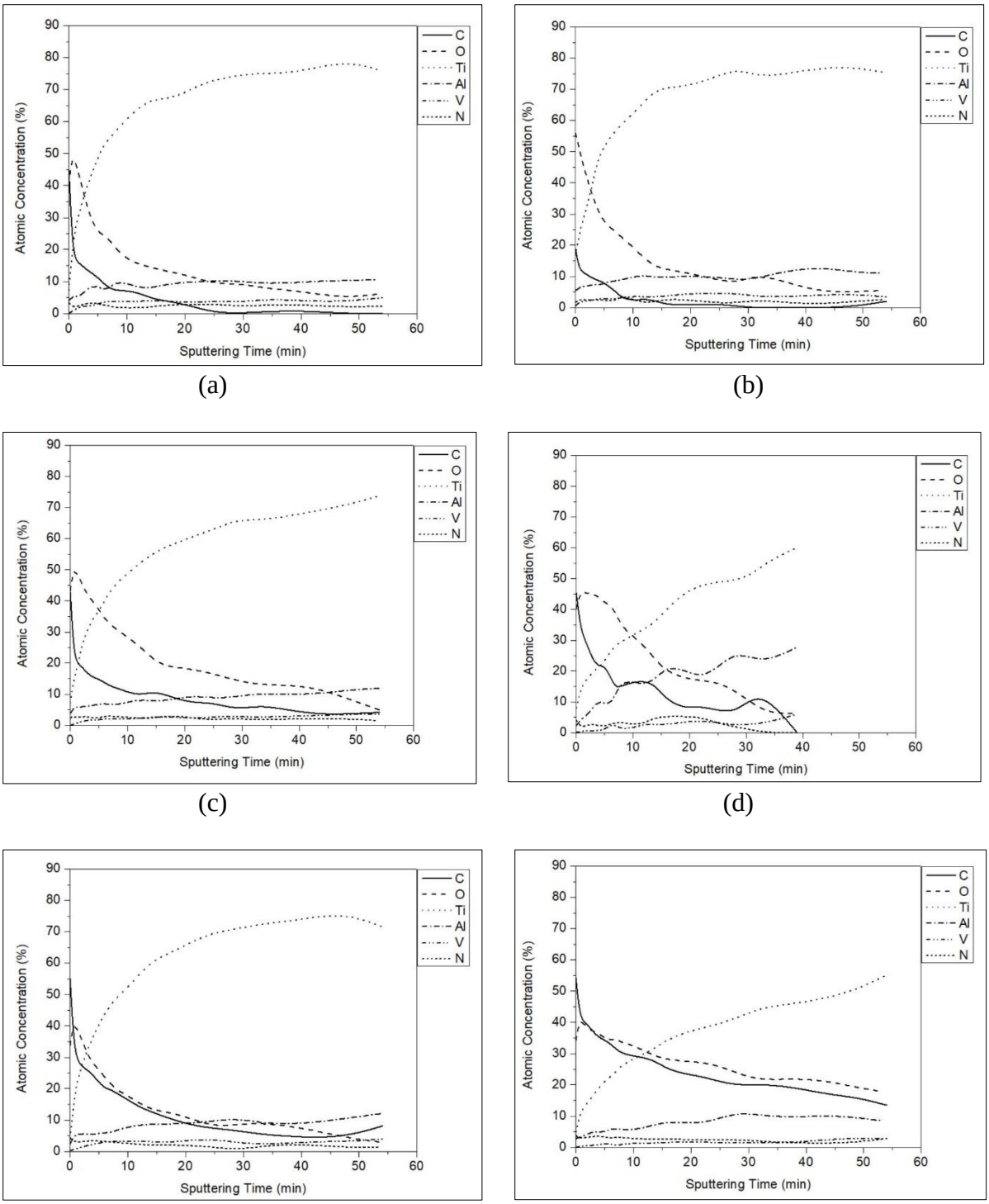

Figure 4.36: Depth profiles of (a) V13 lattice (b) V13 solid (c) 1x13 lattice (d) 1x13 solid (e) 5x13 lattice and (f) 5x13 solid.

The cation depth profiles were plotted in order to identify the cation enrichment. Figure 4.37 exhibits these profiles measured from lattice and solid samples fabricated by using different powder batches. It is evident from the figures that, titanium concentration is found to get enriched towards the interior region of the sample, compared to the surface. A slight increase in concentration of vanadium can also be observed in all the lattice and solid samples, towards

the interior region. The aluminium concentration is observed to be decreasing with sputtering. Higher concentration of aluminium is observed at the surface compared to the bulk of the sample. However, a contradiction is observed in the 1x13 solid sample. Notice the Al concentration measured in this sample is considerably higher than others. This can be possible due to the following reasons : (A) localized enrichment of aluminium on the analyzed region (B) presence of inclusions or contaminants which can alter the concentration percentage of cations. Nevertheless, the trend shown by vanadium in 1x13 solid sample is similar to other implant samples.

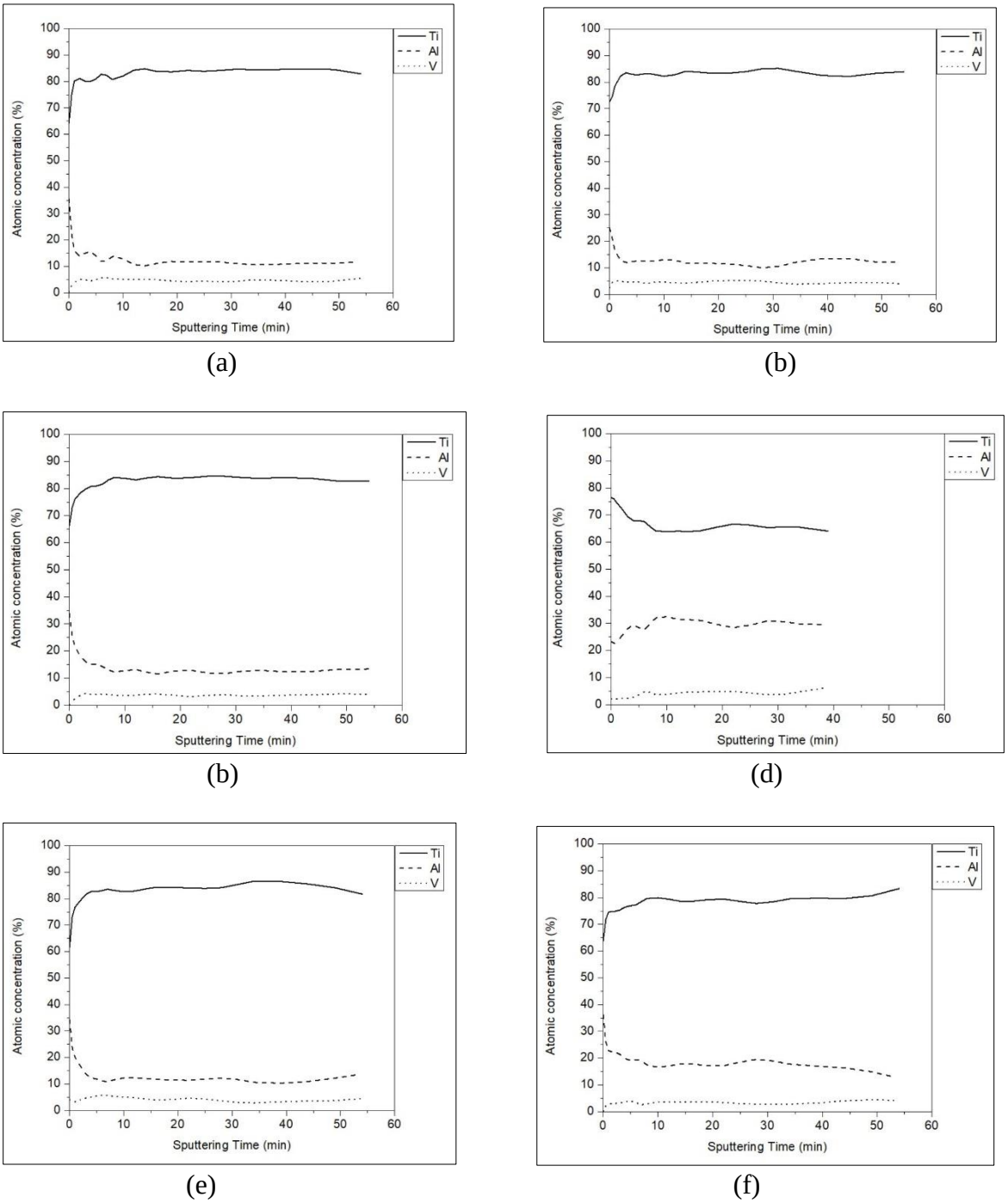

Figure 4.37: Cation depth profiles of (a) V13 lattice (b) V13 solid (c) 1x13 lattice (d) 1x13 solid (e) 5x13 lattice and (f) 5x13 solid.

4.2.3.4 Thickness of Oxide layer on the implant samples

The oxide thickness of the sample was calculated as the depth, when the intensity of the O1s was reduced to half of its maximum intensity in the depth profiles. The obtained values of oxide thickness can not be considered as the actual thickness of oxides. Nevertheless, the method was found to be effective in formulating a comparison between the oxide thickness of the samples [55]. Figure 4.38 portrays a plot which depicts the variation in thickness of oxide layer in the lattice and solid samples with respect to powder recycling. A clear increase in oxide thickness can be observed in the solid samples with powder recycling. This can be attributed to the increase in oxygen content of powder samples with recycling. However, the oxide thickness only differs slightly in the lattice samples.

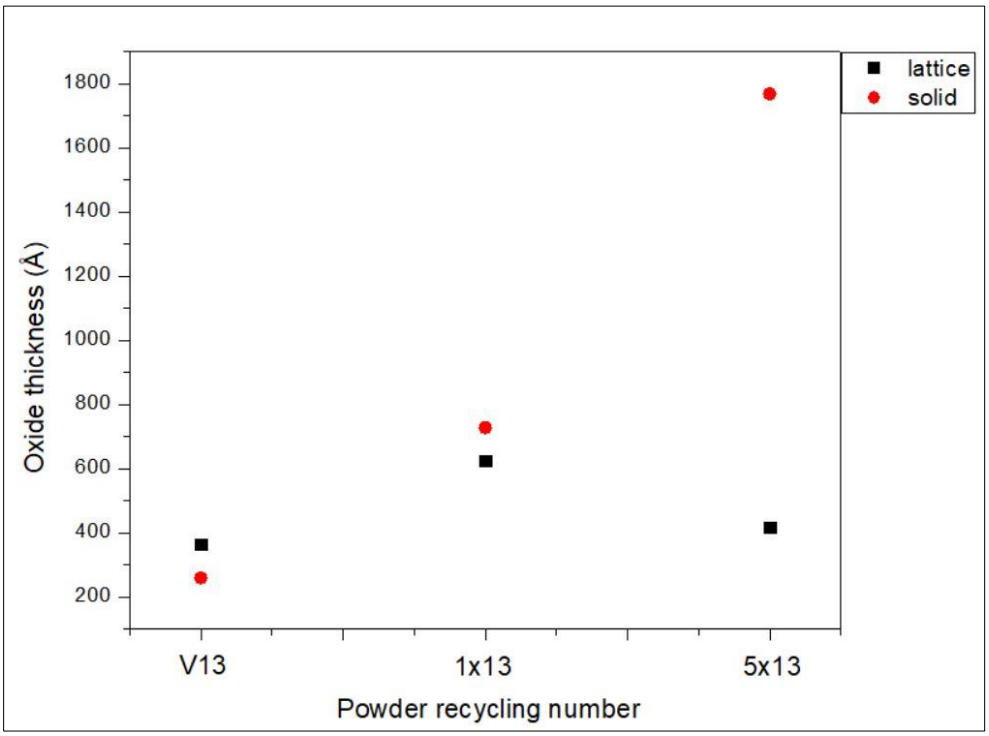

Figure 4.38: Scatter plot depicting the variation in oxide thickness of implants, with powder recycling

4.2.4 Implant lattice – geometrical analysis

4.2.4.1 Average lattice strut thickness

A strut is the thin solid section of a porous lattice network (Figure 4.39). Strut thickness is an important factor which decides the biological and mechanical properties of the developed bone implant [83]. The morphometric analysis using the micro-CT data was evaluated to get the average strut thickness which is portrayed in Figure 4.40 and 4.41.

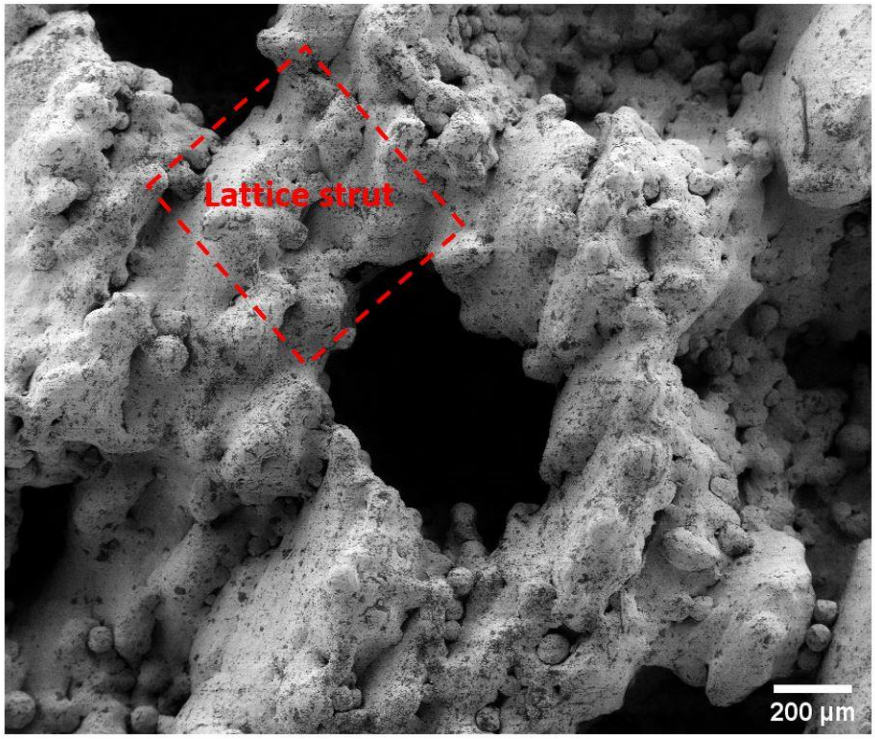

Figure 4.39: SEM micrograph of V13 implant showing a lattice strut

The plots in Figure 4.40 portrays the variation in average strut thickness at bottom, middle and top region of the implant with respect to powder recycling. In V13 implant (Figure 4.40 (a)), the average strut thickness is found to be decreasing and then increasing with increasing distance from the build plate. For 1x13 and 5x13 implants (Figure 4.40 (b) and (c)), an increasing trend is observed with respect to an increase in distance from the build plate.

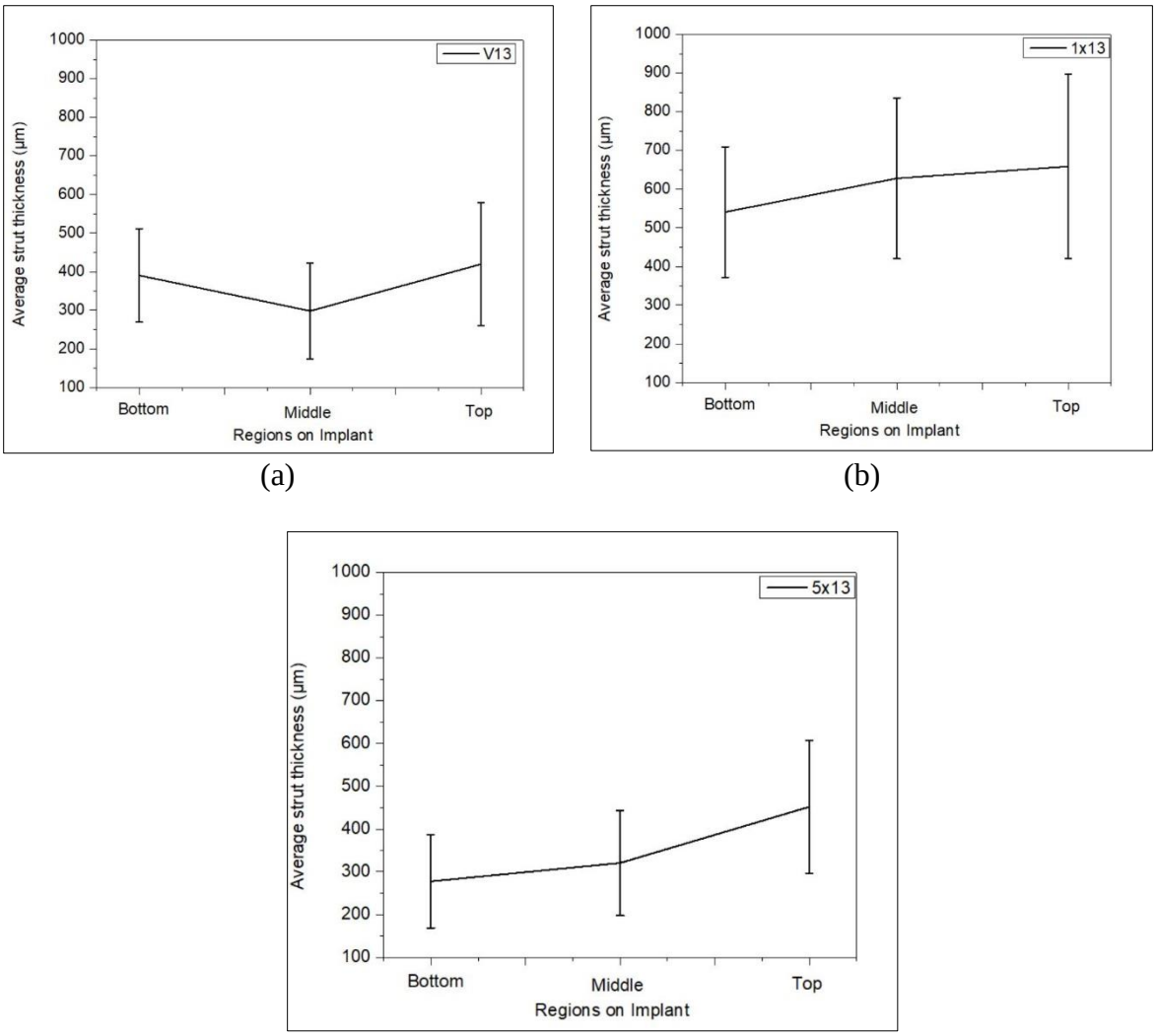

Figure 4.40: Plot depicting the average strut thickness at different regions in (a) V13 implant (b) 1x13 implant (c) 5x13 implant

The average strut thickness is found to be increasing from ~ 400 µm in V13 (bottom region) to ~ 550 µm in 1x13 implant (bottom region). However, the thickness is found to be decreasing to ~ 250 µm in 5x13 implant (bottom region). A similar trend is observed in case of middle and top regions of the implant. The trend observed with the build height can be attributed to the varying scan strategy with respect to increasing build height.

Figure 4.41 portrays the variation of average strut thickness with respect to powder recycling. Comparison plots are made to identify the variations at the bottom, middle and top regions of the implant. The lattice strut thickness is found to exhibit an increase with 1 time powder recycling and decrease with 5 times powder recycling. A similar trend is observed in top, middle and bottom region of the implant samples. The strut thickness of the V13 samples were measured approximately in between 250 – 450 µm. The 1x13 sample had an average strut thickness of 500 – 650 µm. However, the strut thickness of 5x13 samples were measured in between 350 – 450 µm. The constant trend observed in the top, bottom and middle sections is possibly due to the similar scan strategy and build orientation utilized at each region of the build, irrespective of the feedstock.

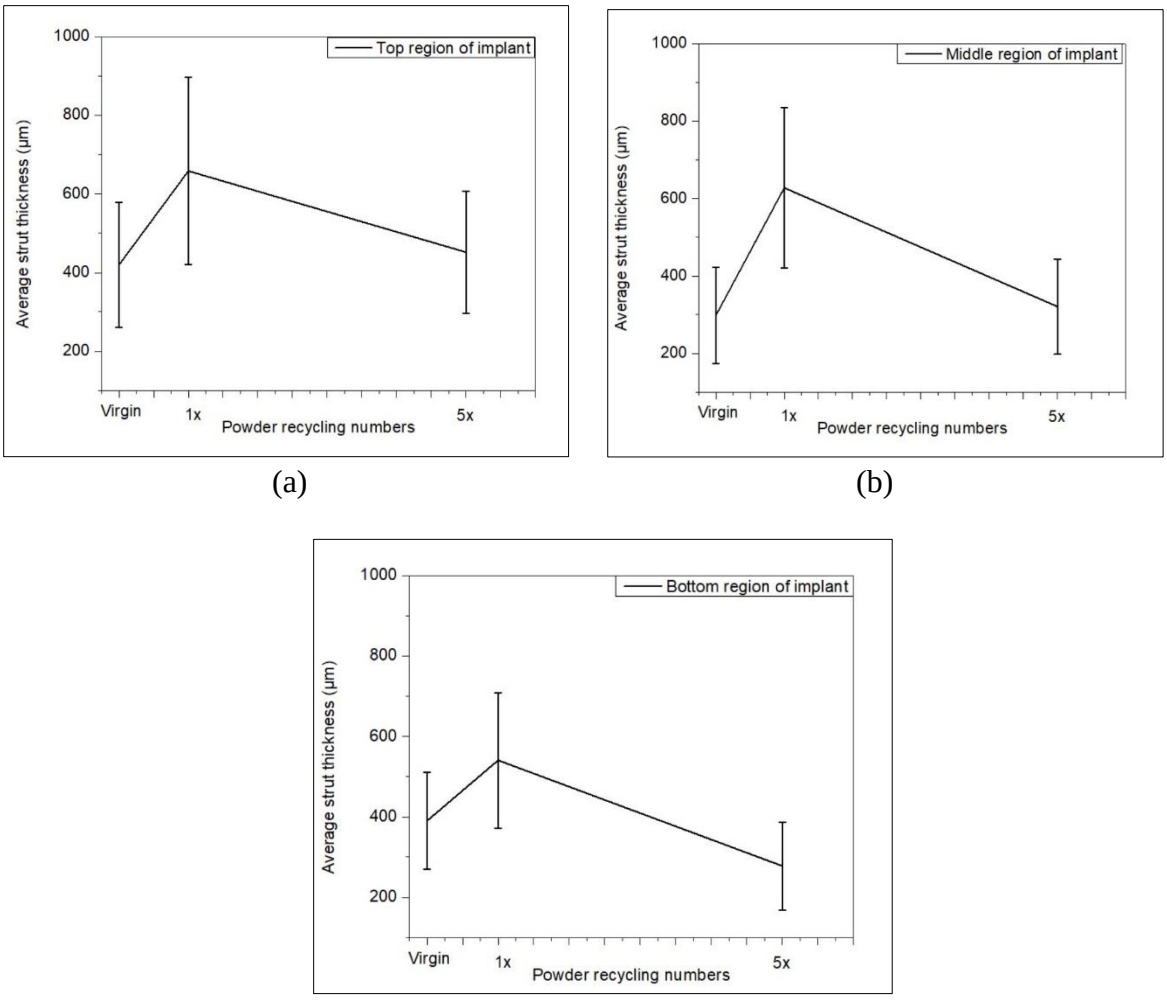

Figure 4.41: Plot depicting the average strut thickness for implant samples at different powder recycling numbers in the (a) top region of implant (b) middle region of implant (c) bottom region of implant

4.2.4.2 Lattice strut thickness distribution

The morphometric analysis tool in the CTAn software was used to generate a distribution of strut thickness. Figure 4.42 portrays the strut thickness distribution of V13, 1x13 and 5x13 implants at different regions in the build, namely top, middle and bottom region. Figure 4.42 (a), (b) and (c), exhibits the strut thickness distribution of V13 implant at top, middle and bottom region respectively. It can be observed that the distribution exhibits a shift towards the left in the middle region. This means that more struts have thickness in between 100 – 400 µm. Nevertheless, this shift is not observed in the bottom region of the sample. A similar trend is observed in the case of 5x13 sample. However, this phenomenon was not observed in 1x13 sample. The distribution range was larger in 1x13 sample, compared to V13 and 5x13 samples.

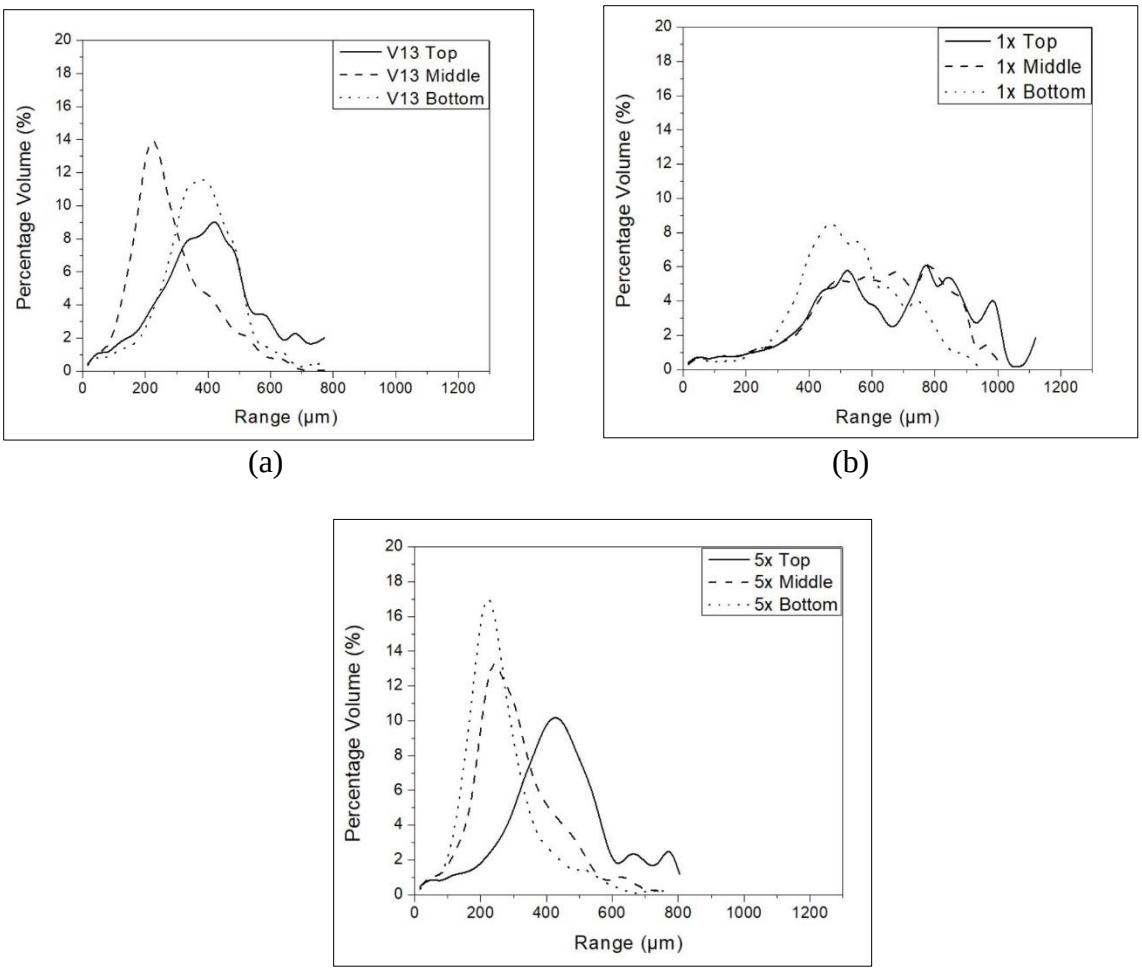

Figure 4.42: Plot depicting the strut thickness distribution at (a) V13 implant (b) 1x13 implant region (c) 5x13 implant

The strut thickness was found to be less than 500 µm in most of the samples, except 1x13. The ideal thickness of the strut for enhanced biological performance is still debated. Nevertheless, researchers have claimed that a strut thickness < 500 µm is most suitable for biomechanical rejuvenation and molecule transport [83]. 1x13 sample exhibited slightly differed distribution of strut thickness. This may be attributed to the fabrication oddity. However, further investigation should be carried out to validate this disagreement.

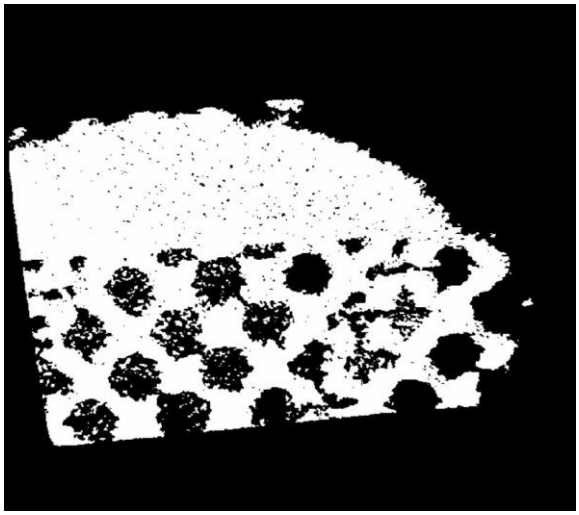

Figure 4.43: Thresholded image of the 5x13 bottom region sample (from CTAn software).

Figure 4.43 shows the thresholded X-ray image of 5x13 bottom region sample. This image was chosen from an optimal location in the slices of images generated, in order to provide an overview of the sample. Dark spots can be observed on the sample surface. Nevertheless, it can not be confirmed to be innate porosities in lattice and solid region of the sample. The resolution used for scanning was approximately 16 µm. A better resolution was not used due to lack of available resources and time during the Covid-19 pandemic. So the dark spots can be artifacts from the measurement, instead of pores. Also, the poor resolution (16-µm) used for imaging resulted in a poor quality of the generated 3D model (Figure A3, A4 and A5).

4.2.5 Implant lattice – topography and roughness

Confocal microscopy technique was utilized to analyze the surface topographical features of all lattice samples. The topographical analysis revealed the presence of various surface anomalies. Figure 4.44 portrays 3D maps of V13, 1x13 and 5x13 lattice implant samples, at the middle and bottom region of the build, fabricated with various batches of powder feedstock. The portrayed images of all the samples are acquired from a similar location in the build design, in order to perform a comparison study. The analyses was not performed at the top region of the implants due to limited availability of time and resources.

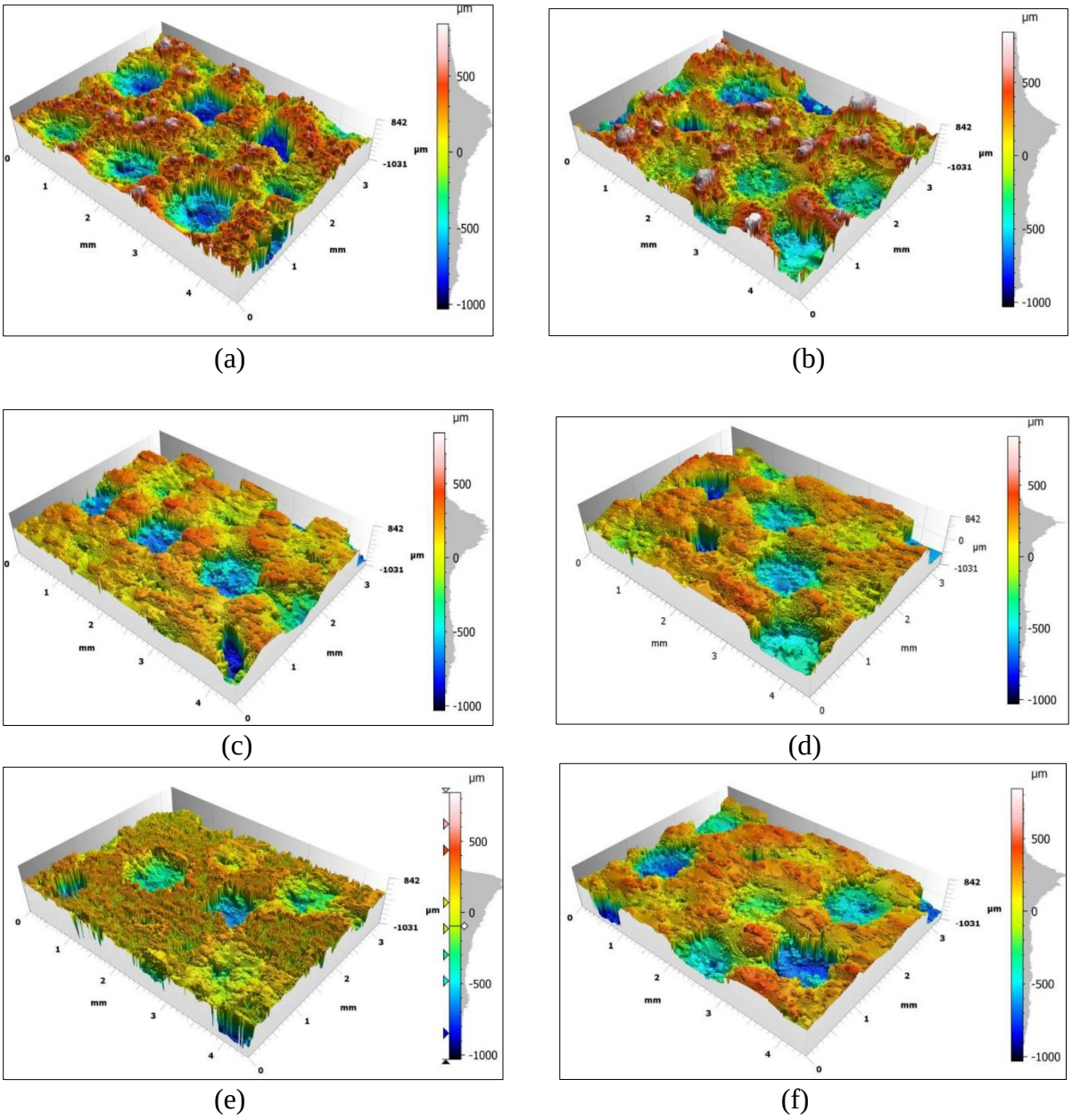

Figure 4.44: 3D maps portraying the peaks and valleys in lattice sample of (a) V13 bottom region (b) V13 middle region (c) 1x13 bottom region (d) 1x13 middle region (e) 5x13 bottom region (f) 5x13 middle region

The porous lattice networks of the implants were printed on a thick solid region. Several topographical features, namely, peaks and valleys can be evidently seen on the 3D maps of lattice samples. The variations in height and depth of the peaks and valleys are indexed by different colours. The maximum height of the peaks and depth of valleys were evaluated in both bottom and middle regions of the implant samples. Figure 4.45 portrays the maximum peak height (S_p) and valley depth (S_v) of the implant samples. The maximum peak height can be defined as height of the highest topographical feature on the lattice sample, while the maximum valley depth can be defined as the depth of the lowest topographical feature identifed on the lattice. It can be noted from the figures that the highest peaks and lowest valleys are observed in V13 implant samples. A marginally decreasing trend is observed in the peak height

for 1x13 and 5x13 implant samples. The trend can be observed in both middle and bottom regions.

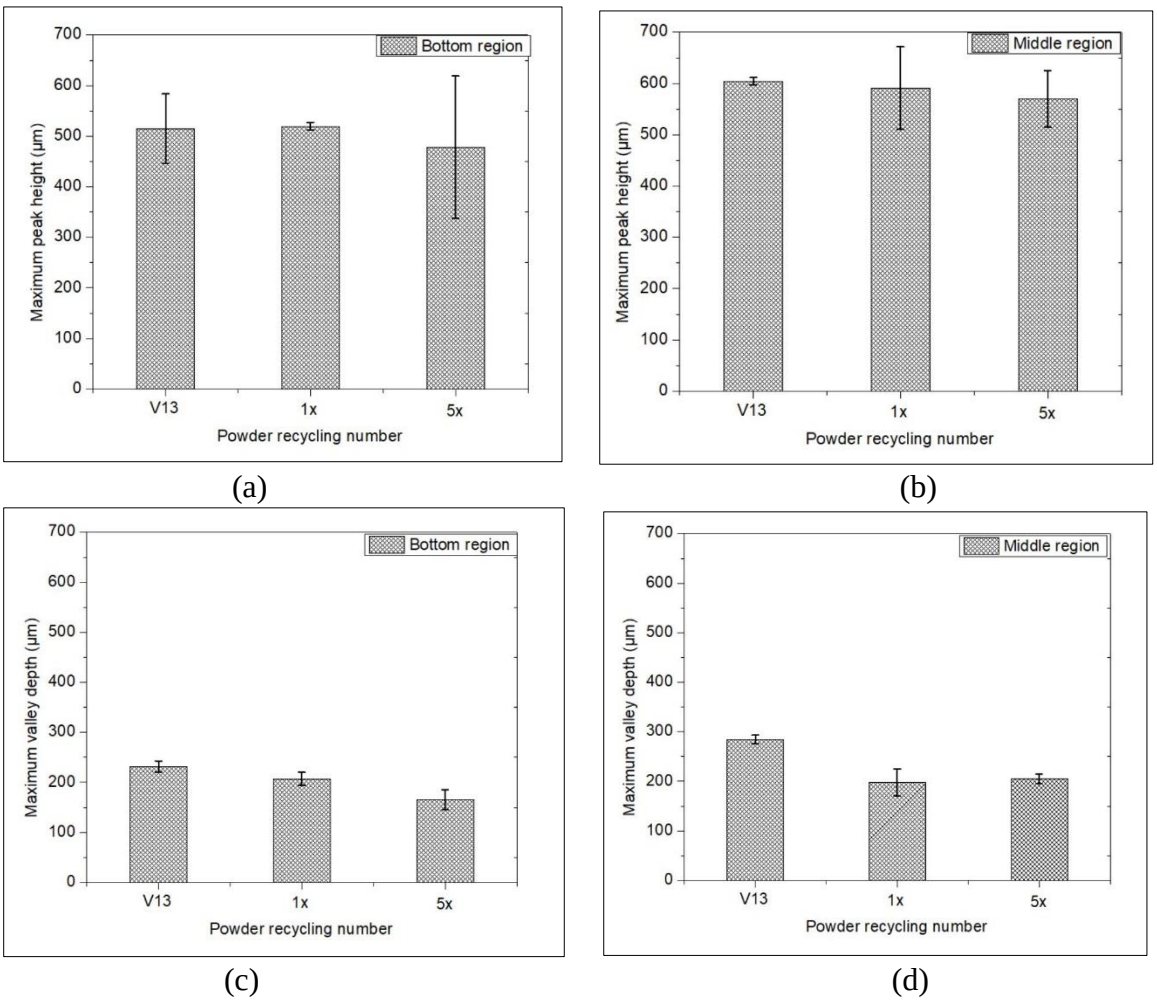

Figure 4.45: Plots exhibiting (a) maximum peak height at bottom region of implant samples (b) maximum peak height at middle region of implant samples (c) maximum valley depth at bottom region of implant samples (d) maximum valley depth at middle region of implant samples

Heat maps of the lattice implant samples were generated using the Mountains Map 8 software (Figure 4.46). The portrayed heatmaps of the lattice implants were generated from similar locations in the build design. The roughness distribution of the surface subjected to analysis can be identified from the exhibited heat maps. Figure 4.46 (a), (b) and (c) shows the heat maps of the bottom regions in V13, 1x13 and 5x13 lattice implant samples. It can be observed that the V13 lattice has rougher particulates on the sample surface compared to 1x13 and 5x13 samples. This trend can be also be observed in the middle region of the implant samples (Figure 4.46 (d), (e) and (f)).

A comparison was made between the mean surface roughness values (S_a) of V13, 1x13 and 5x13 implant samples (Figure 4.47). The Sa value evaluated in this investigation is the mean surface roughness measured over an area. It is evident from the plot that the S_a value is decreasing with respect to increasing powder recycling number in the bottom region of the

sample (Figure 4.47 (a)). A similar trend is observed in the middle region of the implant samples (Figure 4.47 (b)).

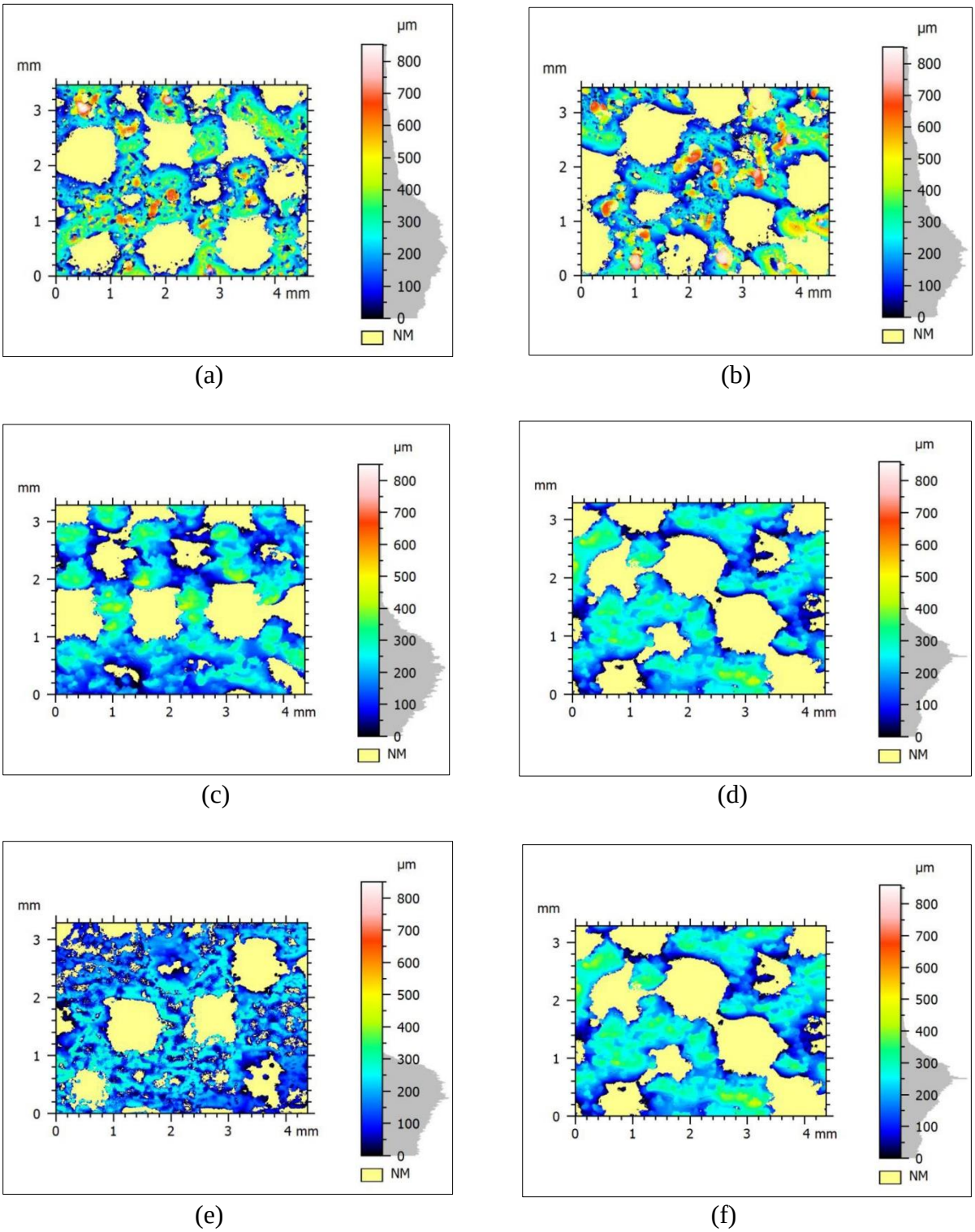

Figure 4.46:Heat maps portraying the surface roughness in the lattice sample at (a) V13 bottom region (b) V13 center region (c) 1x13 bottom region (d) 1x13 middle region (e) 5x13 bottom region (f) 5x13 middle region

The decreasing trend in the mean surface roughness values (S_a) with powder recycling is a contradiction to the observations on solid samples. Studies have concluded that the solid samples exhibits an increase in surface roughness with powder recycling [84]. However, the contradiction observed in this case can be attributed to the complicated lattice geometry and the smaller dimensions which are developed by EBM process. Also, the S_a values have a trivial increase with an increase in building height.

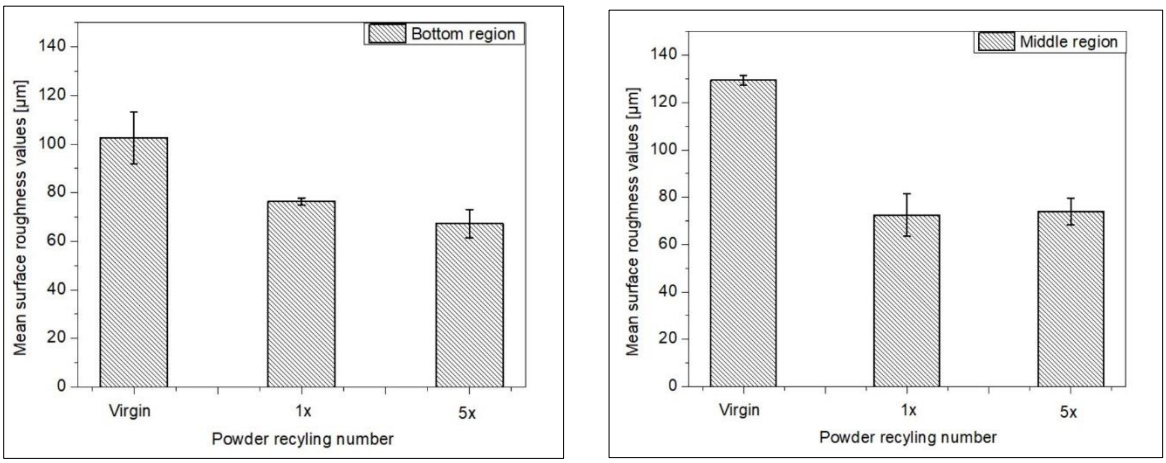

(a) (b)

Figure 4.47: Comparison plots portraying the variation in surface roughnes values of lattice samples with powder recycling, at the (a) bottom region of the implant samples and (b) top region of the implant sample.

5. Conclusion and Remarks

The present investigation was carried out to identify the effect of powder recycling on the microstructural, geometrical and chemical properties of the fabricated acetabular cups. Analyses were performed on three different implant samples manufactured using virgin, 1 time recycled and 5 times recycled powder feedstock. The lattice and solid sections on the implant samples were subjected to investigation including the variations on microstructure, surface roughness and geometry on the implant with respect to build height. Apart from the fabricated implants, the feedstock samples were also subjected to experimental studies for comparing the variations of morphologies and microstructure observed in virgin and recycled powder batches.

The microstructural analysis were performed at lower magnifications using optical microscope and higher magnifications using SEM. The elongated structure of the grains due to epitaxial growth in EBM process is evident from the OM micrographs. Typical EBM microstructural features like grain boundary α, basket weave α, colony α and β phase were observed in both top and bottom region of all the solid implant samples. The microstructure at the bottom and the top section of the solid implant samples are found to be heterogeneous. Variations with respect to build height was clearly observed in the SEM micrographs. The top section of V13, 1x13 and 5x13 implant samples possesses larger fraction of martensitic phase, compared to the bottom section microstructure, in solid samples. Apart from the usual Ti-6Al-4V EBM microstructural features, peculiar phases like α bulges and large α patches were also identified. High magnificantion analysis using FEG-SEM, revealed the presence of randomly distributed β nano particles. The lattice samples were found to possess a higher fraction of α'-martensitic phases. Apart from the α'-martensite, several phases like grain boundary α, basket weave α, colony α and β phase were also observed in the lattice microstructure. However, no significant variation was observed on the microstructure in the solid and lattice sample, with powder recycling.

An EDS compositional analyses of the implant samples were conducted by keeping the beam voltage constant. A significant difference was observed between the phases present in the microstructure. The α phases were found to be enriched with aluminium, while the β phases were enriched with vanadium. In addition, β phases in both TS and BS samples show an increase in Fe content, compared to the α phases. The α bulge phase in the BS samples of V13 and 5x13 implants are found to have higher vanadium content compared to the TS samples. A contradiction is observed in 1x13 BS sample. Although, higher oxygen content is found in β phases in all TS samples compared to α phases, however, this difference is not found in BS samples. The implant samples did not exhibit any phenomenal variations in the elemental composition of phases in V13, 1x13 and 5x13 implant samples, with powder recyling. The porosity analyses revealed the presence of typical EBM defects like lack of fusion and gas porosities. With an increase in build height, an increase in porosity percentage is exhibited in all the implant samples. For TS samples, powder recycling increases the porosity. However, for samples near to the build plate, the percentage porosity is decreasing after 1 time recycling, while the 5x13 sample exhibited a similar porosity value compared to virgin sample.

The XPS survey spectra revealed the presence of Ti, Al, V, N, O, Si, C, Fe and Ca at the surface. Carbon and Ca was confirmed to be surface contaminants on the lattice and solid surfaces of the implant. Titanium was found to be exisiting as TiO_2, with an oxidation state of Ti^{4+}. Aluminum peak was located at a binding energy of 74.2 eV validating the existance of aluminium as Al_2O_3. Vanadium and nitrogen are found to be existing as V_2O_5 and TiN, respectively. There was no significant variation in oxidation states of solid and lattice samples.

Moreover, powder recyling have no significant affect on the oxidation states of elements. An increase in oxide thickness was observed in samples fabricated with recycled powder. The larger oxide thickness in 1x13 and 5x13 samples is due to the higher oxygen content in recycled feedstock. The solid region of all the implant samples is found to have a larger oxide thickness, compared to the lattice samples. An implant will have an enhanced ion transport and bone rejuvenation with the presence of an oxide layer [84]. Nevertheless, previous investigations have pointed out that the bio-compatability is independent of oxide thickness [78]. The present oxide in the implant samples, might also combine with water molecules to form hydroxide.

The geometrical analyses of the implant samples were useful in calculating the strut thickness of the implant samples. The average strut thickness of V13 and 5x13 samples were found to be less than 500 µm, which is most suitable for tissue growth [83]. A larger strut thickness value found in 1x13 sample can be attributed to the EBM process anomalies. However, a broader distribution of strut thickness was observed in 1x13 samples, compared to V13 and 5x13 samples. The enhanced distribution of strut thickness may generate an anisotropic behaviour in terms of the mechanical properties in the implant [85]. The average strut thickness values are found to have an increasing trend with an increase in build height, for both the recycled samples. A difference is observed in case of V13 samples, where the average strut thickness values are found to be decreasing and then increasing with respect to build height.

The topography and surface roughness of the lattice samples were analyzed using confocal microscopy. The presence of peaks and valleys was revealed in the lattice topography. The maximum peak height and valley depth was found to be decreasing with powder recycling. The values of maximum valley depth and peak height is found to exhibit an increasing trend with respect to increase in build height. The surface roughness distribution can be distinguished by utilizing a generated heat map of the lattice strut. The average roughness values of all the implant samples were calculated from these heat maps. A clear declining trend of roughness with powder recycling was found in the lattice struts of V13, 1x13 and 5x13 samples. But, the S_a values are found to be increasing with an increase in build height. Nevertheless, further research should be carried out in order to confirm these findings.

The analyses on the powder samples portayed a significant variation in powder morphology, microstructure and elemental composition. The powder particles were deformed and the surface finish was found to be degrading, with powder recycling. A notable change in microstructure was observed in the powder particles after 5 times recycling. The fraction of martensitic needles was higher in virgin and 1 time recycled power. But, the 5 times recycled powder has presence of phases like α bulges and β phases. EDS analysis indicated that Al concentration was higher in the surface region compared to the interior region. It was likely that, the O concentration increase with powder recyling.

6. Future scope

The project scope could not be expanded further due to the lack of resources and time available during the Covid-19 pandemic. Further research should be carried out in order to support the formulated conclusions.

A detailed analysis should be carried out in order to explain the EBM microstructure. Apart from the phase identification, further quantitative analysis should be carried out for assessing the fraction of each phases present in the implant samples. This could be helpful in correlating the mechanical properties with the microstructural features.

The mechanical properties of the developed implant samples should be investigated in order to formulate the fatigue and impact resistance properties of the implant samples. A detailed study should be conducted on the β nano particles. The distribution and exact composition of these particles should be identified. Electron Backscattered Diffraction analysis could be carried out to identify the grain orientation and discriminate the various phases present in the implant microstructure.

The investigation should be conducted using more implant samples fabricated with recycled powder batches. This is essential to validate the present investigation.

7. References

[1] I. Gardner Business Media, “Additive Manufacturing,” *Additive Manufacturing*, 2021. [Online]. Available: https://www.additivemanufacturing.media/.

[2] S. and D. P. Arabnejad Khanoki, “Fatigue design of a mechanically biocompatible lattice for a proofof-concept femoral stem.,” *J Mech Behav Biomed Mater,* vol. 22, pp. 65–83, 2013.

[3] Darryl L. Millis, “Responses of Musculoskeletal Tissues to Disuse and Remobilization,” in *Canine Rehabilitation and Physical Therapy*, 2nd ed., 2014, pp. 92–153.

[4] Liu, P.C. et al., “A study on the mechanical characteristics of the EBM-printed Ti-6Al-4V LCP plates in vitro.,” *J Orthop Surg Res,* vol. 9, p. 106, 2014.

[5] Wu, S.H. et al., “Porous titanium-6 aluminum-4 vanadium cage has better osseointegration and less micromotion than a poly-ether-ether-ketone cage in sheep vertebral fusion. ,” *Artif Organs,* vol. 37(12), pp. E191-201., 2013.

[6] Ponader, S. et al., “In vivo performance of selective electron beam-melted Ti-6Al-4V structures.,” *J Biomed Mater Res A,* vol. 92, pp. 56–62, 2010.

[7] vol. I. M. J. Donachie, *“Titanium: A technical guide,”* II. The Materials Information Society, 2000.

[8] A.S.M International, “Titanium Alloys,” in *Materials Properties Handbook*, ASM International, 1994.

[9] J. O. Milewski, “Additive Manufacturing,” in *Santa FE*, Springer International Publishing, 2017.

[10] “AZoM.com, ‘Titanium Alloys in Medical Applications,’” *AZO Materials*, 2000. [Online]. Available: http://www.azom.com/article.aspx?ArticleID=1794.

[11] B. Bikramjit, “Biomaterials for Musculoskeletal Regeneration,” *Singapore: Springer*, 2016.

[12] A. Cunha, “Multiscale Femtosecond Laser Surface Texturing of Titanium and Titanium Alloys for Dental and Orthopaedic Implants,” no. JANUARY, pp. 1–294, 2015.

[13] A. M. Abraham, “Encyclopedia of sustainable technologies,” *Cambridge: Elsevevier*, 2017.

[14] F. H. Froes and H. B. Bomberger, “‘The Beta Titanium Alloys,’” *JOM*, vol. 37, no. 28, 1985.

[15] A. Abbas, A. Seif, I. El-Mahallawi, and W. Khalifa, “Microstructure and Hardness of Subzero Quenched and Heat Treated Ti-6Al-4V Alloy,” in *Proceedings of the 3rd Pan American Materials Congress*, 2017, pp. 379–391.

[16] Chattoraj, “‘Stress corrosion cracking (SCC) and hydrogen-assisted cracking in titanium alloys,’” *Stress Corros. Cracking, Elsevier*, pp. 381-408., 2011.

[17] H. G. H. Campbell, . T. B. Lagrange, W. E. King, J. D. Colvin, A. Ziegler, N. D. Browning and K. and H. Bostanjoglo, “The HCP To BCC Phase Transformation in Ti Characterized by Nanosecond Electron Microscopy Solid-Solid Phase Transformations in Inorganic Materials 2005,” *Miner. Met. Mater. Soc.*, 2005.

[18] A. A. Antonysamy, “Microstructure, Texture and Mechanical Property Evolution during Additive Manufacturing of Ti6Al4V Alloy for Aerospace Applications,” Manchester, UK, 2012.

[19] K. K. and M. M. J. Sieniawski, W. Ziaja, “Microstructure and Mechanical Properties of High Strength Two-Phase Titanium Alloys 2013.,” *InTech*, 2013.

[20] R. Pederson, “Microstructure and phase transformation of Ti-6Al-4V,” Luleå, Sweden,

2002.
[21] Manufactur3D, “7 Types of Additive Manufacturing Process,” 2018. [Online]. Available: https://manufactur3dmag.com/7-types-additive-manufacturing-technologies/. [Accessed: 16-Aug-2021].
[22] Crantia Technologies, “3D Printing,” *iLearnCANA*, 2020. .
[23] Wohlers Associates, “What is Additive Manufacturing?,” *Wohlers Associates*. [Online]. Available: https://wohlersassociates.com/additive-manufacturing.html.
[24] I. G. R. S. Khorasani, “Powder Bed Fusion,” in *Additive Manufacturring Technologies*, Springer, 2020, pp. 125–170.
[25] M. G. R. Mahmud Ashra, Ian Gibson, “CHALLENGES AND PROSPECTS OF 3D PRINTING IN STRUCTURAL ENGINEERING,” in *13th International Conference on Steel, Space and Composite StructuresAt: Perth, Australia*, 2018.
[26] Arcam.com, “ArcamAB,” Sweden, 2017.
[27] Sebastian Duda, “Microstructure Evolution of EBM Fabricated Ti-6Al-4V,” Gothenburg, 2020.
[28] T. O. M. Koike, K. Martinez, L. Guo, G. Chahine and R. Kovacevic, “Evaluation of titanium alloy fabricated using electron beam melting system for dental applications,” *J. Mater. Process. Technol*, vol. 211, pp. 1400–1408, 2011.
[29] X. T. et Al., “Graded microstructure and mechanical properties of additive manufactured Ti-6Al-4V via electron beam melting,”,” *Acta Mater*, vol. 97, pp. 1–16, 2015.
[30] W. Z. and I. T. S. S. Al-bermani, M. L. Blackmore, “The Origin of Microstructural Diversity, Texture, and Mechanical Properties in Electron Beam Melted Ti-6Al-4V,” *Metall. Mater. Trans. A*, vol. 41 A, pp. 3422-3434, 2010.
[31] EMMANUEL MUZANGAZA, “The Effects of Titanium Ti-6Al-4V Powders Manufactured Using Electron Beam Melting (EBM) - Additive Manufacturing on Metallurgical Evaluation.,” 2018.
[32] GE Additive, “Arcam EBM Q10 plus,” *General Electric*, 2021. [Online]. Available: https://www.ge.com/additive/additive-manufacturing/machines/ebm-machines/arcam-ebm-q10plus.
[33] H. P. T. et Al., “Microstructure, Mechanical Properties, and Flatness of SEBM Ti-6Al-4V Sheet in As-Built and Hot Isostatically Pressed Conditions,” *Jom*, vol. 69, pp. 466–471, 2017.
[34] R. D. and Z. X. Guo, “Microstructural evolution of a Ti–6Al–4V alloy during β-phase processing: experimental and simulative investigations,” *Mater. Sci. Eng. A*, vol. 365, pp. 172–179, 2004.
[35] W. Q. T. et al., “Microstructure and wear properties of electron beam melted Ti-6Al-4V parts : a comparison study against as-cast form,” *Metals (Basel).*, vol. 6, p. 284, 2016.
[36] P. N. H. Galarraga, D. A. Lados, R. R. Dehoff and M. M. Kirka, “Effects of the microstructure and porosity on properties of Ti-6Al-4V ELI alloy fabricated by electron beam melting (EBM),” *Addit. Manuf.*, vol. 10, pp. 47–57, 2016.
[37] S. V. J. Sneha Goel, Magnus Ahlfors, Fouzi Bahbou, “Effect of Different Post-treatments on the Microstructure of EBM-Built Alloy 718,” *J. Mater. Eng. Perform. 28(2)*, 2018.
[38] F. Medina, “Reducing metal alloy powder costs for use in powder bed fusion additive manufacturing: Improving the economics for production,” Texas, 2013.
[39] “LPW Technology LTd, ‘lpwtechnology,’” 2020. [Online]. Available: http://www.lpwtechnology.com/technical-library/technical-information/methods-of-powderproduction/.

[40] I. T. Watkins & H. M. Davies1& O. G. Stanners & S. Marchisio, “Powder interlayer bonding of geometrically complex Ti-6Al-4V parts,” *Int. J. Adv. Manuf. Technol.*, vol. 106, 2020.
[41] Rajesh P.Verma, “Titanium based biomaterial for bone implants: A mini review,” in *Materials Today: Proceedings*, 2020, pp. 3148–3151.
[42] T. Albrektsson et al., “The interface zone of inorganic implantsIn vivo: Titanium implants in bone,” *Mater. Sci. Ann. Biomed. Eng.*, 2006.
[43] L. E. M. et al., “Next-generation biomedical implants using additive manufacturing of complex, cellular and functional mesh arrays,” *Philos Trans A Math Phys Eng Sci .*, 2010.
[44] T. Stich et al., “Implant-bone-interface: Reviewing the impact of titanium surface modifications on osteogenic processes in vitro and in vivo,” *Bioeng. Transl. Med.*, 2021.
[45] “Optical Microscope - Some Basics,” *Leica Microsystems*, 2012. [Online]. Available: https://www.leica-microsystems.com/science-lab/optical-microscopes-some-basics/.
[46] Microscope world, “Microscope World,” 2015. [Online]. Available: http://blog.microscopeworld.com/2015/05/how-does-light-microscope-work.html.
[47] O. P. C. and P. Ka, “Scanning Electron Microscope: Advantages and Disadvantages in Imaging Components,” *Int. J. Curr. Microbiol. Appl. Sci.*, vol. 6, pp. 1877–1882, 2017.
[48] D. J. W. Zhou, R. Apkarian and Z. L. Wang, “Fundamentals of scanning electron microscopy (SEM),” *Scanning Microsc. Nanotechnol. Tech. Appl., pp. 1–40, 2007,* pp. 1–40, 2007.
[49] Thermo Fisher Scientific, “Principles of Scanning Elelctron Microscopy,” 2021. [Online]. Available: https://www.thermofisher.com/se/en/home/materials-science/learning-center/applications/scanning-electron-microscope-sem-electron-column.html.
[50] R. W. and C. Wang, “Springer Tracts in Modern Physics,” *Prog. Nanoscale Charact.*, vol. 272, 2018.
[51] and D. C. J. I. Goldstein, D. E. Newbury, J. R. Michael, N. W. M. Ritchie, J. H. J. Scott and Joy, “Microscopy and X-Ray Microanalysis.”
[52] K. Yase, “Transmission Electron Microscopy,” vol. 43, no. 2, 1994.
[53] C. X-rays, “Analytical Electron Microscopy for Materials Science,” *Mater. Today*, vol. 6, p. 38, 2003.
[54] Meyers, “Mechanical Behaviour of Materials, .,” in *Mechanical Behaviour of Materials*, 2nd ed., Cambridge: Cambridge University Press.
[55] S. Axelsson, “Surface characterization of Titanium Powders with X-Ray Photoelectron Spectroscopy,” Gothenburg, 2012.
[56] LOS ALAMOS NATIONAL LABORATORY, “XPS Works,” *University of California for the US Department of Energy*, 1998. [Online]. Available: https://www.lanl.gov/orgs/nmt/nmtdo/AQarchive/04summer/XPS.html.
[57] J. Watts, J.F. and Wolstenholme, “An introduction to surface analysis by XPS and AES.,” in *An introduction to surface analysis by XPS and AES.*, West Sussex, England: Wiley, 2003.
[58] J. B. Lumsden, “Chapter X-Ray Photoelectron Spectroscopy.,” in *Materials Characterizations*, Ohio: ASM International, 1986, pp. 568–580.
[59] J. F. Wagner, C.D., Riggs, W.M., Davis, L.E. and Moulder, *Handbook of X-Ray Photoelectron Spectroscopy.* Eden Prairie, Minnesota: Corporation, Perkin-Elmer, 1979.
[60] Bruker, “SkyScan 1272.” [Online]. Available: https://www.bruker.com/en/products-

and-solutions/microscopes/3d-x-ray-microscopes/skyscan-1272.html.
[61] A. Palmquist, F. A. Shah, L. Emanuelsson, O. Omar, and F. Suska, “A technique for evaluating bone ingrowth into 3D printed, porous Ti6Al4V implants accurately using X-ray micro-computed tomography and histomorphometry,” *Micron*, vol. 94, pp. 1–8, 2017.
[62] M.D. Bentley et al., “The use of microcomputed tomography to study microvasculature in small rodents,” *AJP Regul. Integr. Comp. Physiol.*, vol. 28295), 2002.
[63] Olympus, “Introduction to Confocal Microscopy,” *Olympus Corp.*, 2021. [Online]. Available: https://www.olympus-lifescience.com/en/microscope-resource/primer/techniques/confocal/confocalintro/.
[64] N. Gathimba and Y. Kitane, “Static ductility evaluation of corroded steel plates considering surface roughness characteristics,” *2018 Struct. Congr.*, no. August, p. 13, 2018.
[65] Yu Sun et al., “The effect of recycling on the oxygen distribution in Ti-6Al-4V powder for additive manufacturing,” *Mater. Hight Temp.*, vol. 35, no. 1–3, pp. 217–224, 2017.
[66] S.Ghods et al., “Electron beam additive manufacturing of Ti6Al4V: Evolution of powder morphology and part microstructure with powder reuse,” *Materialia*, vol. 9, 2020.
[67] G. S. M. Vlasea and, “The effect of reuse cycles on Ti-6Al-4V powder properties processed by electron beam powder bed fusion,” *Manuf. Lett.*, vol. 25, pp. 60–63, 2020.
[68] C. de F. et Al., “Micromechanical behavior and thermal stability of a dualphase α+α’ titanium alloy produced by additive manufacturing,” *Acta Mater., vol.*, vol. 162, pp. 149–162, 2019.
[69] N. Emminghaus, C. Hoff, J. Hermsdorf, and S. Kaierle, “Residual oxygen content and powder recycling: Effects on surface roughness and porosity of additively manufactured Ti-6Al-4V,” *Addit. Manuf.*, vol. 46, 2021.
[70] Y. Cao, M. Delin, F. Kullenberg, and L. Nyborg, “Surface modification of Ti-6Al-4V powder during recycling in EBM process,” *Surf. Interface Anal.*, vol. 52, no. 12, pp. 1066–1070, 2020.
[71] Nick Connor, “Titanium - Melting Point,” 2020. [Online]. Available: https://www.periodic-table.org/titanium-melting-point/.
[72] N. Connor, “Aluminium - Melting point,” 2020. [Online]. Available: https://www.periodic-table.org/aluminium-melting-point/.
[73] and C. S. L. D. G. Lee, S. Lee, “Quasi-static and dynamic deformation behavior of Ti-6Al-4V alloy containing fine α2-Ti3Al precipitates,” *Mater. Sci. Eng. A*, vol. 366, pp. 25–37, 2004.
[74] Daido Steel group, “Titanium and Titanium Alloy,” 2020. [Online]. Available: https://www.daido.co.jp/en/products/titanium/chemical/index.html.
[75] and J. W. S. Raghavan, M. L. S. Nai, P. Wang, W. J. Sin, T. Li, “Heat treatment of electron beam melted (EBM) Ti-6Al-4V: microstructure to mechanical property correlations,” *Rapid Prototyp. J.*, vol. 24, no. 4, pp. 774–783, 2018.
[76] P. Wang, M. L. S. Nai, W. J. Sin, and J. Wei, “Effect of building height on microstructure and mechanical properties of big-sized Ti-6Al-4V plate fabricated by electron beam melting,” *MATEC Web Conf.*, vol. 30, pp. 4–7, 2015.
[77] and A. D. H. Carreon, M. Carreon, “Assessment of precipitates of aged Ti-6Al-4V alloy by ultrasonic attenuation,” *Philos. Mag.*, vol. 97, pp. 58–68, 2017.
[78] C. Larsson, P. Thomsen, J. Lausmaa, M. Rodahl, B. Kasemo, and L. E. Ericson, “Bone response to surface modified titanium implants: studies on electropolished implants

with different oxide thicknesses and morphology," *Biomaterials*, vol. 15, no. 13, pp. 1062–1074, 1994.
[79] W. E. S. C. and A. Lippitz, A., Kemnitz E., Bose, O. and Unger and 4f7=2 Referenced, "XPS binding energy data obtained with di erent aluminium oxides, -hydroxides and - fluorides. ," *Fresenius' J. Ana- lytical Chem.*, vol. 358, pp. 175–179, 1997.
[80] S. Borgmann, D., Hums, E., Hopfengartner, G., Wedler, G. and G. W. and Rademacher, "XPS studies of oxidic model catalysts: internal standards and oxidation numbers," *J. Electron Spectrosc. Relat. Phenomena*, vol. 63, pp. 91–116, 1993.
[81] V. . Huravlev, J.F., Kuznetsov, M.V. and Gubanov, "XPS analysis of adsorption of oxygen molecules on the surface of Ti and TiNx lms in vacuum," *J. Electron Spectros. Relat. Phenomena*, vol. 38, pp. 169–176, 1992.
[82] F. D. P.Simon, N.Bui, N.Pebere, "In situ redox conductivity, XPS and impedance spectroscopy studies of passive layers formed on lead-tin alloys," *J. Power Sources*, vol. 53, no. 1, pp. 163–173, 1995.
[83] I. Yadroitsava et al., "Bone regeneration on implants of titanium alloys produced by laser powder bed fusion: A review," in *Titanium for consumer applications: Real world use of titanium*, 2019, pp. 197–233.
[84] A. Ataee, Y. Li, D. Fraser, G. Song, and C. Wen, "Anisotropic Ti-6Al-4V gyroid scaffolds manufactured by electron beam melting (EBM) for bone implant applications," *Mater. Des.*, vol. 137, pp. 345–354, 2018.
[85] L. Damiati *et al.*, "Impact of surface topography and coating on osteogenesis and bacterial attachment on titanium implants," *J. Tissue Eng.*, vol. 9, 2018.

8. Appendix

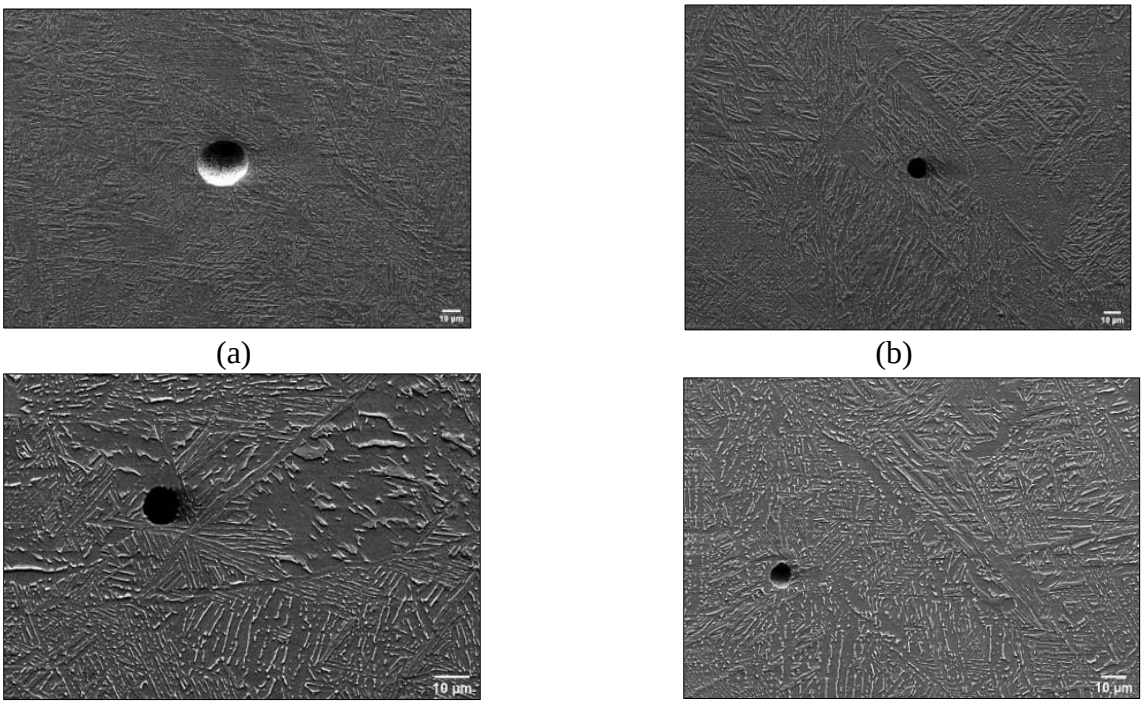

(a) (b)

(c) (d)

Figure A1: SEM micrographs depicting gas porosities in solid region of implant (a) 1x13 top section (b) 1x13 bottom section (c) 5x13 bottom section (d) V13 bottom section

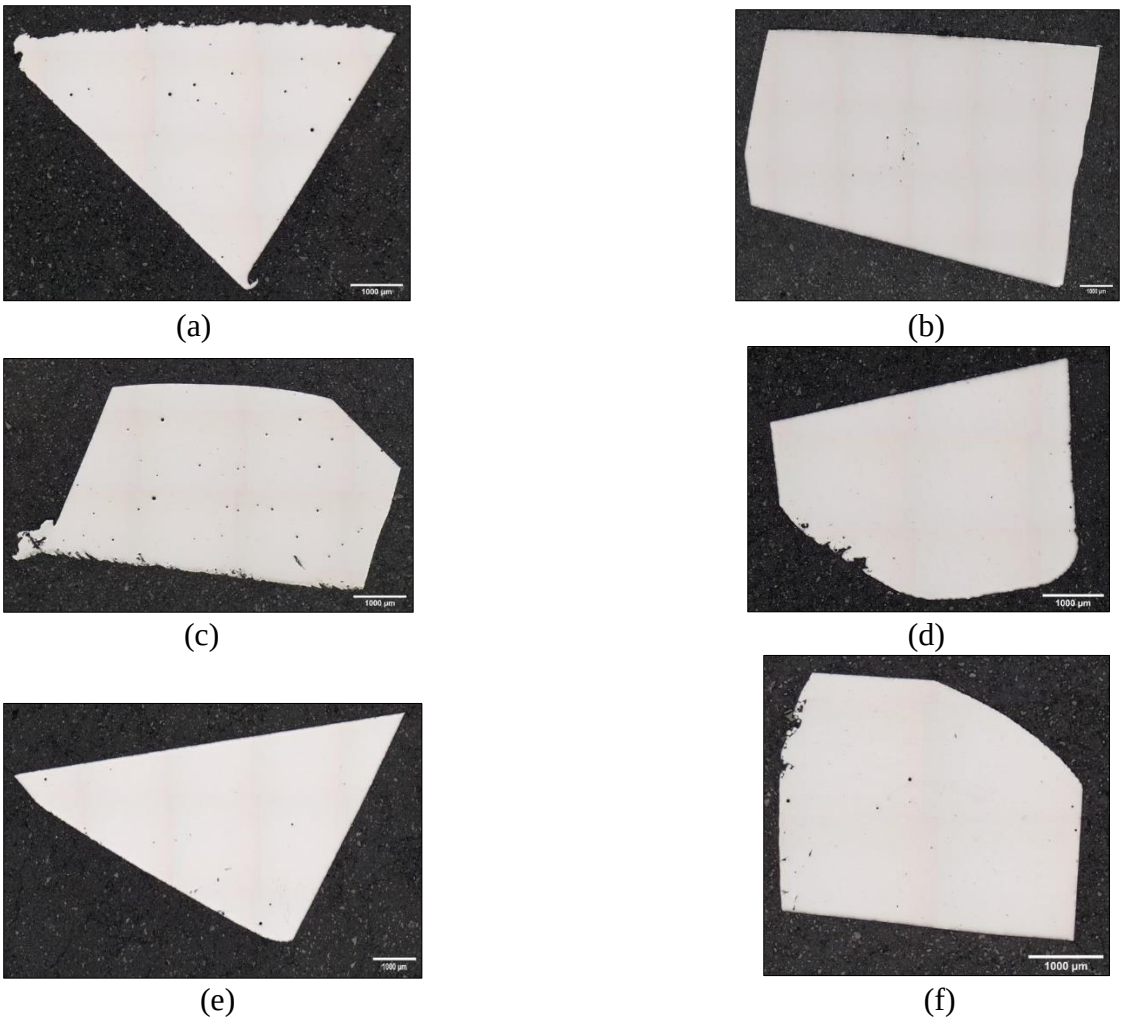

Figure A2: Stitched OM micrographs of (a) V13 top section (b) V13 bottom section (c) 1x top section (d) 1x13 bottom section (e) 5x13 top section (f) 5x13 bottom section

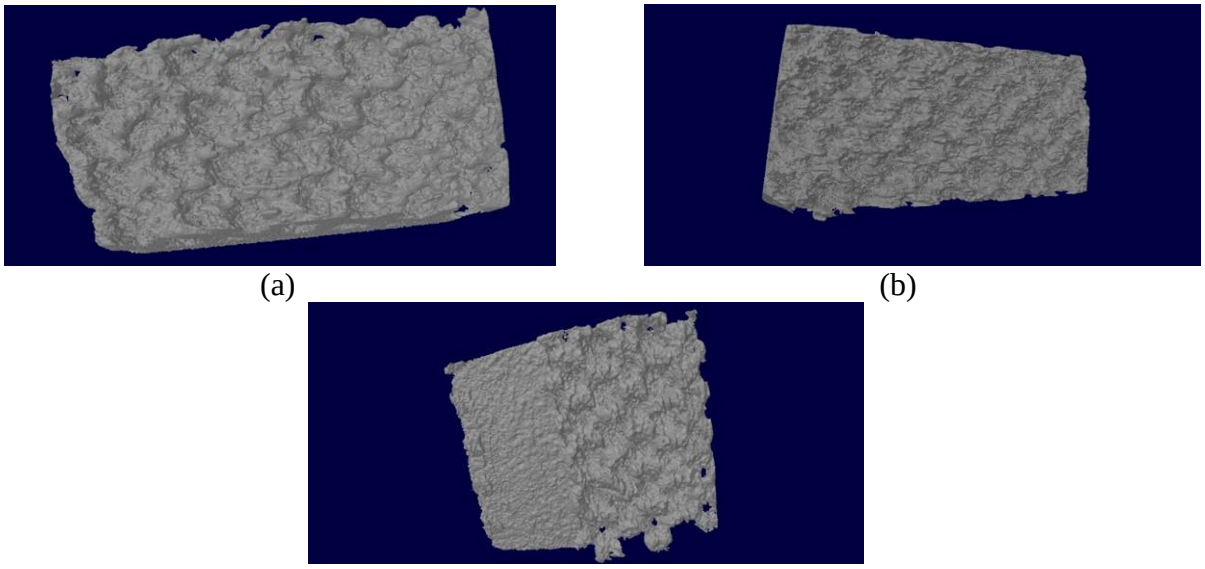

Figure A3: CTAn generated 3D model of (a) V13 top section (b) V13 middle section (c) V13 bottom section

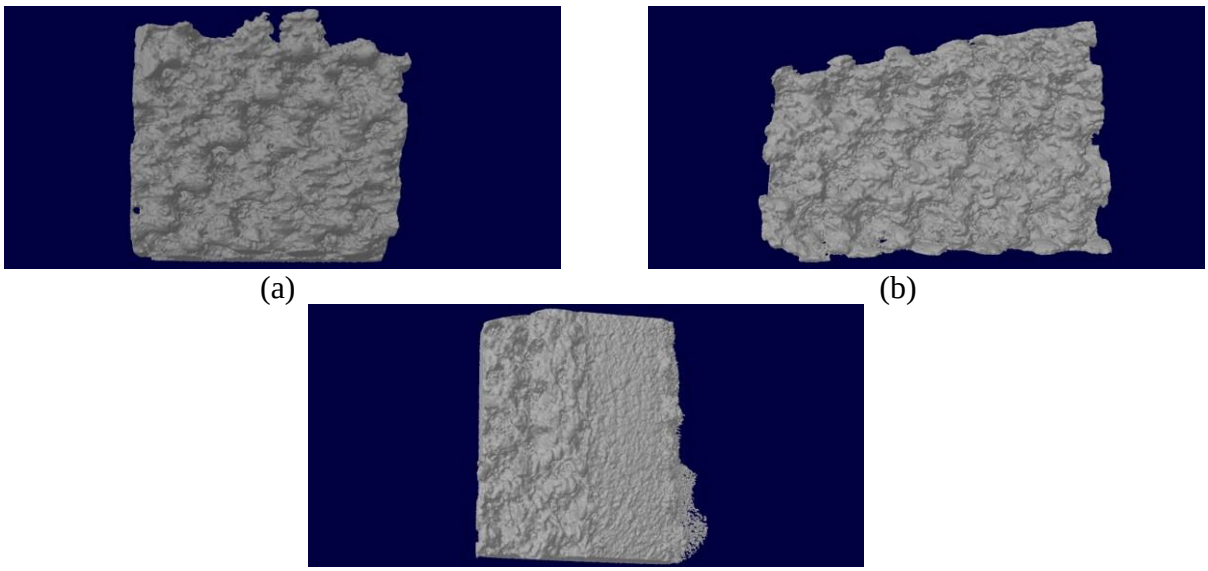

Figure A4: CTAn generated 3D model of (a) V13 top section (b) V13 middle section (c) V13 bottom section

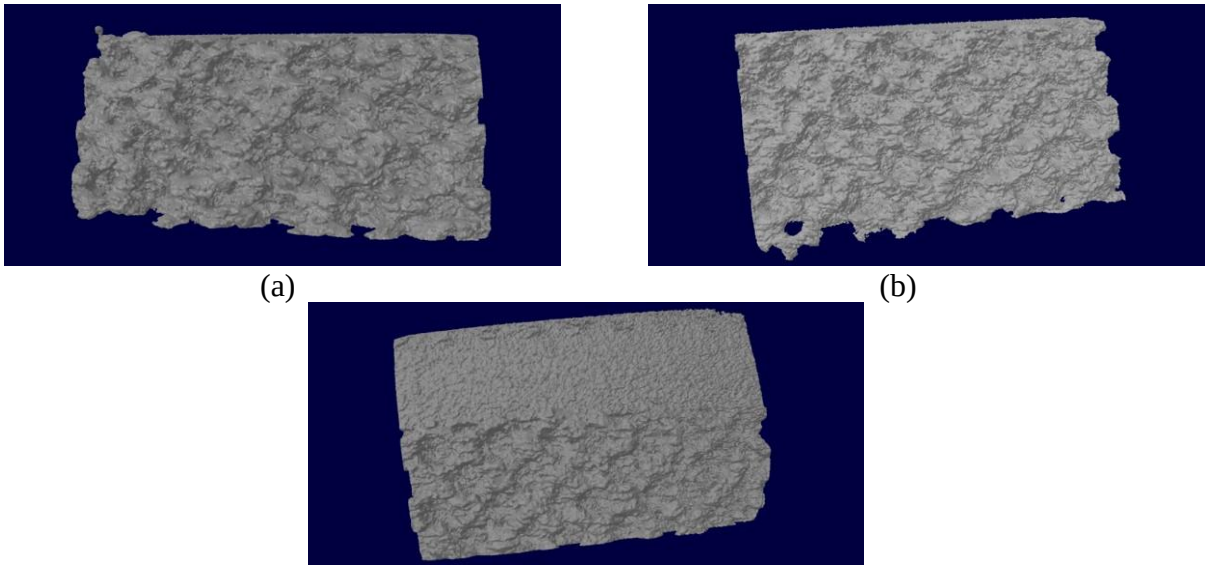

(a) (b)

(c)

Figure A5: CTAn generated 3D model of (a) V13 top section (b) V13 middle section (c) V13 bottom section

DEPARTMENT OF INDUSTRIAL AND MATERIALS SCIENCE
CHALMERS UNIVERSITY OF TECHNOLOGY
Gothenburg, Sweden
www.chalmers.se

CHALMERS
UNIVERSITY OF TECHNOLOGY